

UK Nitrides Consortium Winter Meeting

7-8 January 2021

Online
Event



IOP Institute of Physics

<http://UKNC2021.iopconfs.org/home>



UKNC Winter Meeting

7–8 January 2021

Programme

Please note all times are in GMT.

Thursday 7 January

12.00	Opening remarks By Rachel Oliver, Philip Shields, Rob Martin and David Binks
	Session 1: Keynote Presentation <u>Chair:</u> Rob Martin, University of Strathclyde, UK
12.15	(Invited) AlGa_N Nanostructures for Electron Beam Pumped UV Emitters Eva Monroy, French Commission for Atomic Energy and Alternative Energies, France
13.00	Lunch
	Session 2: Structural and optical materials characterisation <u>Chair:</u> Philip Shields, University of Bath, UK
13.45	Multimicroscopy of cubic InGa_N/Ga_N MQWs Bonning Ding, University of Cambridge, UK
14.00	Defect structures in (001) zincblende Ga_N/3C-SiC nucleation layers Martin Frentrup, University of Cambridge, UK
14.15	Direct evidence of an Al alloyed Si_Nx interlayer within an ammonia predosed AlN/Si interface via STEM-EELS Simon Fairclough, University of Cambridge, UK
14.30	Non-Radiative Recombination Centers in InGa_N/Ga_N Core-Shell Nanorods Probed by Hyperspectral Cathodoluminescence Imaging Kagiso Loeto, University of Cambridge, UK
14.45	Non-destructive imaging of residual strains in Ga_N and their effect on optical and electrical properties through correlative light–electron microscopy Naresh Kumar Gunasekar, University of Strathclyde, UK
15.00	Carrier dynamics in and around trench defects in InGa_N QWs probed by time resolved cathodoluminescence Gunnar Kusch, University of Cambridge, UK
15.15	Break
	Session 3: Modelling <u>Chair:</u> Rachel Oliver, University of Cambridge, UK
15.45	Temperature dependence of radiative and non-radiative recombination rates in c-plane InGa_N/Ga_N quantum wells Joshua McMahon, Tyndall National Institute, Ireland

16.00	Impact of random alloy fluctuations on inter-well transport in InGaN/GaN multi-quantum well systems Michael O'Donovan, Tyndall National Institute, Ireland
Session 4: The Humphreys Lecture	
<u>Chair:</u> Matthew Halsall, University of Manchester, UK	
16.15	(Invited) Exploring (and exploiting) the physics of ultra-wide-bandgap nitrides Chris Van de Walle - University of California Santa Barbara, USA

Friday 8 January

Session 5: The Foxon Lecture	
<u>Chair:</u> Peter Parbrook, Tyndall National Institute, Ireland	
09.00	GaN for display applications enabled by transfer printing Brian Corbett - Tyndall National Institute, Ireland
Posters and flash presentations session	
09.45	P1 Light emission from Zn-doped InN colloidal quantum dots Ruben Ahumada-Lazo, The University of Manchester, UK
09.47	P2 Employing a CMOS-Integrated GaN μLED Array to Generate Superimposed Pulse Amplitude Modulation for Optical Camera Communications Navid Bani Hassan, University of Strathclyde, UK
09.49	P3 Effects of Ammonia Substrate Pretreatment on the Strain Management in GaN-on-Si Structures Alexander Hinz, Fraunhofer FEP, Germany
09.51	P4 HAX-PES measurements of InGaN/GaN heterostructures using a lab-based x-ray source Stephen Church, University of Manchester, UK
09.53	P5 The effects of thermal annealing on the optical properties of Mg-doped zinc-blende GaN Daniel Dyer, University of Manchester, UK
09.55	P6 Study of Ti contacts to corundum α-Ga₂O₃ Fabien Massabuau, University of Strathclyde, UK
09.57	P7 Defects in 10-13 GaN: An electron microscopy study Gunnar Kusch, University of Cambridge, UK
09.59	P8 Multi-microscopy of a single dislocation cluster within a GaN-on-GaN p-i-n diode Simon Fairclough, University of Cambridge, UK
10.01	P9 Combined Time of Flight and Photometric Stereo Imaging for Surface Reconstruction Emma Le Francois, University of Strathclyde, UK
10.03	P10 Structural impact of step-graded AlGaIn buffer variants on MOCVD grown GaN-on-Si Saptarsi Ghosh, University of Cambridge, UK
10.05	P11 The role of the nucleation step in self-assembled GaN nanowire growth Nian Jiang, University of Cambridge, UK
10.07	P12 Tomography of Porous Gallium Nitride Nanostructures Maruf Sarkar, University of Cambridge, UK
10.09	P13 Thick GaN capped AlGaIn/GaN HEMTs for reduced surface effects Maira Elksne, University of Glasgow, UK
10.11	P14 Investigation of Electrically Active Defects in In_{0.15}Ga_{0.35}N/GaN Multi Quantum Wells Grown on Different Substrates by Using Deep Level Transient Spectroscopy Abdulaziz Almalki, University of Nottingham, UK

10.13	P15 A study of the effect of a Si-doped underlayer on photoluminescence in InGaN/GaN QWs Stephen Church, University of Manchester, UK
10:15	Breakout rooms discussion - posters
11.15	Break
Session 6: Quantum wells and LEDs	
<u>Chair:</u> Fabien Massabuau, University of Strathclyde, UK	
11.30	Application of GaN-based series-biased micro-LED arrays to long-distance visible light communications Enyuan Xie, University of Strathclyde, UK
11.45	Size and wavelength-dependent characterisation of ultraviolet microlight-emitting diodes Jonathan McKendry, University of Strathclyde, UK
12.00	Effect of localised state filling and defect density on the efficiency of InGaN/GaN QWs Rachel Barrett, The University of Manchester, UK
12.15	A comparison of efficiency droop in wurtzite and zincblende InGaN/GaN quantum wells Stephen Church, University of Manchester, UK
12.30	Lunch
Session 7: Electronic Devices	
<u>Chair:</u> David Binks, University of Manchester, UK	
13.15	Evaluation of doping profiles by UV-induced increase in channel conductivity in AlGaIn/GaN High Electron Mobility Transistors Markus Wohlfahrt, University of Bristol, UK
13.30	Crystalline AlGaIn & SiC Interlayers for Integration of Diamond with GaN Daniel Field, University of Bristol, UK
13.45	Dual metal gate AlGaIn/GaN HEMTs with improved transconductance and reduced short channel effects Joseph Pinchbeck, The University of Sheffield, UK
14.00	Optimum design choices for AlGaIn/GaN HEMTs on diamond substrates Thomas Gerrer, University of Bristol, UK
14.15	Closing remarks and prize presentation By Rachel Oliver, Philip Shields, Rob Martin and David Binks
14.30	Social activity: UKNC fun quiz

Programme

Thursday 7 January

12.00	Opening remarks
Session 1: Keynote Presentation	
12.15	(Invited) AlGaIn Nanostructures for Electron Beam Pumped UV Emitters Eva Monroy, French Commission for Atomic Energy and Alternative Energies, France
13.00	Lunch
Session 2: Structural and optical materials characterisation	
13.45	Multimicroscopy of cubic InGaIn/GaN MQWs Boning Ding, University of Cambridge, UK
14.00	Defect structures in (001) zincblende GaN/3C-SiC nucleation layers Martin Frentrup, University of Cambridge, UK
14.15	Direct evidence of an Al alloyed SiNx interlayer within an ammonia predosed AlN/Si interface via STEM-EELS Simon Fairclough, University of Cambridge, UK
14.30	Non-Radiative Recombination Centers in InGaIn/GaN Core-Shell Nanorods Probed by Hyperspectral Cathodoluminescence Imaging Kagiso Loeto, University of Cambridge, UK
14.45	Non-destructive imaging of residual strains in GaN and their effect on optical and electrical properties through correlative light-electron microscopy Naresh Kumar Gunasekar, University of Strathclyde, UK
15.00	Carrier dynamics in and around trench defects in InGaIn QWs probed by time resolved cathodoluminescence Gunnar Kusch, University of Cambridge, UK
15.15	Break
Session 3: Modelling	
15.45	Temperature dependence of radiative and non-radiative recombination rates in c-plane InGaIn/GaN quantum wells Joshua McMahon, Tyndall National Institute, Ireland
16.00	Impact of random alloy fluctuations on inter-well transport in InGaIn/GaN multi-quantum well systems Michael O'Donovan, Tyndall National Institute, Ireland
Session 4: The Humphreys Lecture	
16.15	(Invited) Exploring (and exploiting) the physics of ultra-wide-bandgap nitrides Chris Van de Walle - University of California Santa Barbara, USA

Friday 8 January

	Session 5: The Foxon Lecture
09.00	GaN for display applications enabled by transfer printing Brian Corbett - Tyndall National Institute, Ireland
	Posters and flash presentations session
09.45	P1 Light emission from Zn-doped InN colloidal quantum dots Ruben Ahumada-Lazo, The University of Manchester, UK
09.47	P2 Employing a CMOS-Integrated GaN μLED Array to Generate Superimposed Pulse Amplitude Modulation for Optical Camera Communications Navid Bani Hassan, University of Strathclyde, UK
09.49	P3 Effects of Ammonia Substrate Pretreatment on the Strain Management in GaN-on-Si Structures Alexander Hinz, Fraunhofer FEP, Germany
09.51	P4 HAX-PES measurements of InGaN/GaN heterostructures using a lab-based x-ray source Stephen Church, University of Manchester, UK
09.53	P5 The effects of thermal annealing on the optical properties of Mg-doped zinc-blende GaN Daniel Dyer, University of Manchester, UK
09.55	P6 Study of Ti contacts to corundum α-Ga₂O₃ Fabien Massabuau, University of Strathclyde, UK
09.57	P7 Defects in 10-13 GaN: An electron microscopy study Gunnar Kusch, University of Cambridge, UK
09.59	P8 Multi-microscopy of a single dislocation cluster within a GaN-on-GaN p-i-n diode Simon Fairclough, University of Cambridge, UK
10.01	P9 Combined Time of Flight and Photometric Stereo Imaging for Surface Reconstruction Emma Le Francois, University of Strathclyde, UK
10.03	P10 Structural impact of step-graded AlGaIn buffer variants on MOCVD grown GaN-on-Si Saptarsi Ghosh, University of Cambridge, UK
10.05	P11 The role of the nucleation step in self-assembled GaN nanowire growth Nian Jiang, University of Cambridge, UK
10.07	P12 Tomography of Porous Gallium Nitride Nanostructures Maruf Sarkar, University of Cambridge, UK
10.09	P13 Thick GaN capped AlGaIn/GaN HEMTs for reduced surface effects Maira Elksne, University of Glasgow, UK
10.11	P14 Investigation of Electrically Active Defects in In_{0.15}Ga_{0.35}N/GaN Multi Quantum Wells Grown on Different Substrates by Using Deep Level Transient Spectroscopy Abdulaziz Almalki, University of Nottingham, UK
10.13	P15 A study of the effect of a Si-doped underlayer on photoluminescence in InGaIn/GaN QWs Stephen Church, University of Manchester, UK
10:15	Breakout rooms discussion - posters
11.15	Break

Session 6: Quantum wells and LEDs	
11.30	Application of GaN-based series-biased micro-LED arrays to long-distance visible light communications Enyuan Xie, University of Strathclyde, UK
11.45	Size and wavelength-dependent characterisation of ultraviolet microlight-emitting diodes Jonathan McKendry, University of Strathclyde, UK
12.00	Effect of localised state filling and defect density on the efficiency of InGaN/GaN QWs Rachel Barrett, The University of Manchester, UK
12.15	A comparison of efficiency droop in wurtzite and zincblende InGaN/GaN quantum wells Stephen Church, University of Manchester, UK
12.30	Lunch
Session 7: Electronic Devices	
13.15	Evaluation of doping profiles by UV-induced increase in channel conductivity in AlGaIn/GaN High Electron Mobility Transistors Markus Wohlfahrt, University of Bristol, UK
13.30	Crystalline AlGaIn & SiC Interlayers for Integration of Diamond with GaN Daniel Field, University of Bristol, UK
13.45	Dual metal gate AlGaIn/GaN HEMTs with improved transconductance and reduced short channel effects Joseph Pinchbeck, The University of Sheffield, UK
14.00	Optimum design choices for AlGaIn/GaN HEMTs on diamond substrates Thomas Gerrer, University of Bristol, UK
14.15	Closing remarks and prize presentation
14.30	Social activity: UKNC fun quiz

Thursday 7 January

Session 1: Keynote Presentation

AlGa_N Nanostructures for Electron Beam Pumped UV Emitters

A Harikumar,¹ S Cuesta,¹ I Dimkou,² Q-M Thai,³ F Donantini,⁴ Y Curé,¹ S T Purcell,³ Le Si Dang,⁴ and Eva Monroy¹

¹Univ. Grenoble-Alpes, CEA-IRIG, PHELIQS, France, ²Univ. Grenoble-Alpes, CEA-LETI, France, ³Univ. Lyon, Uni. Claude Bernard Lyon 1, CNRS, Institut Lumière Matière, France, ⁴Univ. Grenoble-Alpes, CNRS, Institut Néel, France

UV disinfection is receiving renewed attention due to the global pandemic, as an immediately deployable and cost-effective option. The common sources used for this application are low-pressure arc lamps, emitting at 254 nm and containing toxic mercury, which Europe is trying to phase out. Furthermore, this radiation is highly carcinogenic and cataractogenic, which represents a health hazard. Recently different replacements for mercury lamps have been proposed, e.g. excimer lamps that emit at 222 nm, supposedly harmless. However, most of the focus is now on AlGa_N-based UV LEDs, with numerous advantages (fast on/off switching, longer lifetime, reduced ozone generation, wider wavelength selection). Yet the wall plug efficiency of commercial LEDs at ≈ 260 nm is WPE < 1%, far below that of mercury lamps, and drops dramatically at shorter wavelengths. Therefore, there is still a need and opportunity for alternative UV sources.

This work proposes electron-beam pumped UV lamps as an alternative to LEDs to overcome issues related to doping, transport and contacting. This approach obviates the need for p-type doping and efficient and homogeneous carrier injection is achieved without an electron blocking layer. Furthermore, the WPE should not vary much over 210–350 nm. Here, we study the performance of AlGa_N/AlN dots-in-a-wire [1] and Stranski-Krastanov quantum dot superlattices [2], whose UV emission can be tailored in the 230–330 nm range. The three-dimensional (3D) carrier confinement in such nanostructures results in high internal quantum efficiency (IQE = 50% on average) and promising external quantum efficiency (EQE up to 5% for as-grown structures). Studies conducted under operation conditions (high injection) show no degradation of the IQE for excitation power densities up to 1 MW/cm², obtained by pumping with a pulsed Nd-YAG laser. With e-beam excitation, the emission efficiency remains stable up to 10 kV of acceleration voltage and 0.5 mA of injected current (current limit of our setup).

E-beam pumping offers also an interesting alternative for the fabrication of UV lasers, highly demanded in the fields of medicine and biotechnology, as well as in 3D printing and non-line-of-sight communication. Today, this spectral range is covered by gas lasers (ArF, KrF, XeF) or lasers based on frequency conversion (Nd:YAG). III-nitride semiconductor laser diodes are promising candidates to provide an efficient semiconductor-based alternative, but current injection is a major problem for wavelengths shorter than 360 nm.

For this application, advantages of the e-beam pumping include higher flexibility in the choice of materials for the active medium due to the absence of doping or electrical contacts, as well as higher radiative recombination efficiency since the electrons and holes generated by impact ionization share the same distribution in the active medium. This technology has enabled the fabrication of ZnSe-based pulsed lasers that emit up to 600 W at 535 nm. There are some studies of e-beam pumped UV lasers using AlGa_N/Ga_N separate confinement heterostructures (SCH), but they are limited to pulsed electron beam excitation at cryogenic temperatures [3,4]. New device architectures are required with the prospect of achieving room temperature lasers. Here, we present a study of undoped AlGa_N/Ga_N SCHs designed to operate under e-beam injection with an acceleration voltage ≤ 10 kV. We discuss the effect of spontaneous and piezoelectric polarization on the carrier diffusion and demonstrate that the performance is improved using an asymmetric graded-index separate-confinement heterostructure (GRINSCH).

[1] H. Arkumar et al., *Nanotechnology* **31** 505205 (2020).

[2] I. Dimkou et al., *Nanotechnology* **31** 204001 (2020).

[3] T. Wunderer et al., *IEEE Photonics Technology Letters* **29** 1344 (2017).

[4] T. Hayashi et al., *Scientific Reports* **7** 2944 (2017).

Session 2: Structural and optical materials characterisation

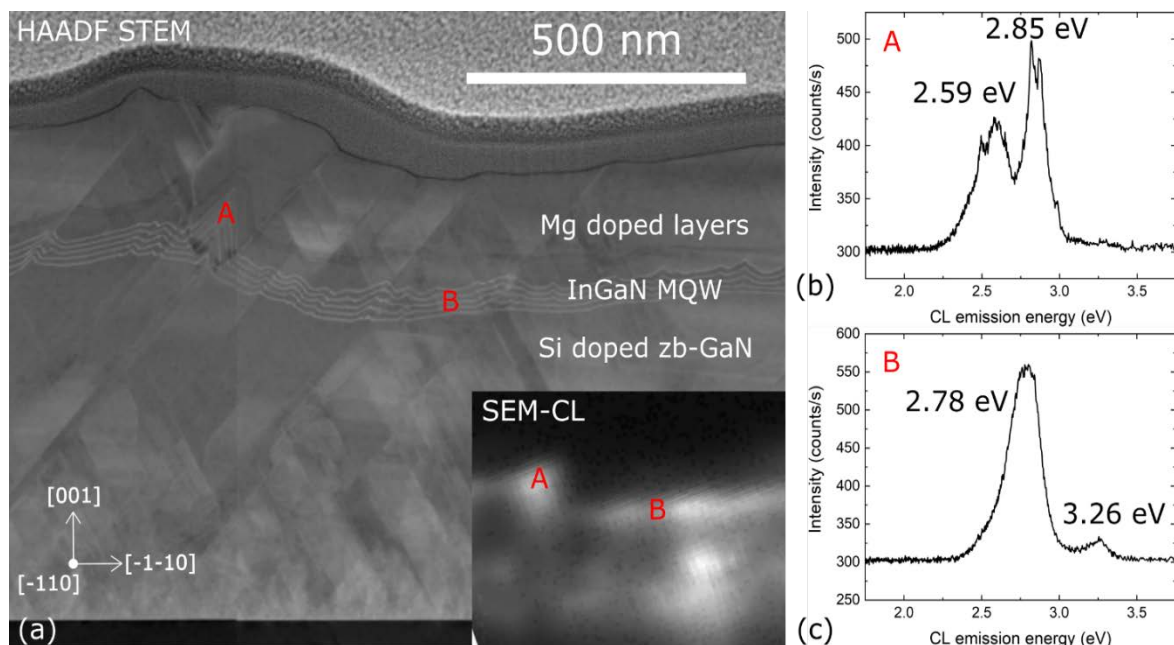
Multimicroscopy of cubic InGaN/GaN MQWs

Boning Ding¹, Martin Frentrup¹, Simon M. Fairclough¹, Gunnar Kusch¹, Menno J. Kappers^{1,2}, Manish Jain³, David J. Wallis^{1,2,3}, and Rachel Oliver¹

¹Department of Materials Science and Metallurgy, University of Cambridge, UK, ²Centre for High Frequency Engineering, University of Cardiff, UK, ³Kubos semiconductors Ltd, Future Business Centre, UK

To achieve white and colour-tunable lighting, the mixing of light from red-, blue- and green-wavelength LEDs is desired. At present, the efficiency of green-wavelength LEDs is approximately half that of red- and blue-wavelength LEDs, which is known as the ‘green gap’ problem [1]. The low efficiency of such devices is related to strong internal electric polarization fields across the quantum wells (QWs) of the commonly used wurtzite c-orientation.

Cubic zincblende GaN has the potential to bridge the ‘green gap’ due to the absence of internal electric fields. Furthermore, the smaller bandgap of cubic nitrides require less indium in InGaN quantum wells to reach the green wavelength region.



(a) HAADF STEM image illustrating the sample structure containing both feature A, a quartzite inclusion region with the QW, and a reference position B, a cubic region with the QW. The inset of (a) shows the panchromatic SEM-CL image corresponding to the same area. The spectra of A and B are present in (b) and (c), respectively. The CL data was recorded at 10K.

We have previously demonstrated the growth of phase pure cubic GaN on 3C-SiC/Si templates [2] but several challenges must be addressed before the optical quality of the zinc blende GaN grown is high enough for efficient green LEDs.

One of the current challenges for zincblende LED structures is the poor spectral purity of the emitted light. Here we demonstrate the use of a multi-microscopy approach to investigate possible causes for the low optical performance of a zincblende research LED heterostructure study one of the causes of the poor spectral purity in detail (figure 1). We have performed scanning transmission electron microscopy (STEM) (figure 1a), energy dispersive X-ray spectroscopy, scanning electron diffraction (SED) and cathodoluminescence hyperspectral imaging (CL) at 10K to characterize and correlate structural and optical properties on the same FIB slice of a cubic MQW structure. The cross-sectional high angular dark field STEM

image in the $[-110]$ zone in Fig 1 (a) shows $\{111\}$ SFs as weak contrast lines running across the heterostructure, which lead to local roughening of the active region. The CL spectra in Fig. 1c of a cubic GaN region (B) with a low density of SFs and relatively flat InGaN MQWs reveals an emission peak of the QWs at about 2.78eV and a weak near band edge (NBE) peak of zb-GaN at about 3.26 eV. In contrast to this reference region, we also observe multiple regions (like region A) of similar intensity in panchromatic SEM-CL images (see inset of Fig. 1a). These regions commonly exhibit a spectral splitting of the QW emission peak into several sub-peaks, and show no significant contributions from the cubic GaN NBE. The SED analysis revealed that region A contains a wurtzite inclusion of about 150 nm width, which is formed on twin boundaries of the surrounding (001) zincblende GaN material, and the STEM analysis shows that the QWs in these regions are formed on inclined facets in the wurtzite inclusion.

In summary, by combining the strength of CL and TEM microscopy techniques we have identified one of the causes for the observed spectral splitting in cubic GaN MQWs and linked it to the presence of a wurtzite inclusion, formed at a twin boundary.

[1] L. Y. Lee, "*Mater. Sci. Technol*", **33**, 14, 1570–1583 (2017)

[2] L. Y. Lee, "*J Appl. Phys.*", **124**, 105302 (2018)

Defect structures in (001) zincblende GaN/3C-SiC nucleation layers

Petr Vacek^{1,2}, Martin Frentrup¹, Lok Yi Lee¹, Fabien C-P Massabuau^{1,3}, Menno J Kappers¹, David J Wallis^{1,4}, Roman Gröger², and Rachel A Oliver¹

¹Department of Materials Science and Metallurgy, University of Cambridge, UK, ²Institute of Physics of Materials & CEITEC IPM, Brno, Czech Republic, ³Department of Physics, SUPA, University of Strathclyde, UK, ⁴Centre for High Frequency Engineering, University of Cardiff, UK

Solving the green gap problem is a key challenge for the development of future LED-based lighting systems. A possible approach to achieve higher LED efficiencies in the green spectral region is the growth of III-nitrides in the cubic zincblende phase (zb). Cubic zb-GaN with (001) orientation is polarisation field free and has a narrower bandgap than its wurtzite structure counterpart, due to which less indium is required in InGaN quantum wells for green light emission. However, given that zb-GaN is metastable under normal growth conditions and has strong similarities with the energetically preferred wurtzite phase, zb-GaN epilayers often exhibit phase mixture and a rich defect structure, which both may negatively influence the optical properties of the material.

In our presentation, we will report on the defect structure in zb-GaN nucleation layers (NLs) grown on (001) 3C-SiC/Si pseudo-substrates, and will discuss mechanisms for the formation of the observed defects more broadly.

High-resolution transmission electron microscopy (TEM) images of individual nucleation islands show a characteristic ABCABC stacking of the $\{111\}$ bi-layers in zb-GaN, revealing that the GaN islands grow epitaxially in the zb phase and (001) orientation on the 3C-SiC surface, with no observable amorphous layer at the interface. Facet angles present in the islands prior to the coalescence were measured by the atomic force microscopy (AFM) and TEM and some corresponded to short $\{111\}$ facets, which might induce SF nucleation. Most of the defects present in the NLs were formed close to the GaN/SiC heterointerface and include perfect dislocations, partial dislocations and predominantly intrinsic $\{111\}$ -type stacking faults. Perfect dislocations and partial dislocations are identified as 60° mixed-type respectively 30° Shockley partial dislocations, which both act as misfit dislocations to relieve the compressive lattice mismatch strain in GaN. No regular arrangement of these misfit dislocations is found at the zb-GaN/3C-SiC interface of our samples, which is in contrast to reports about zb-GaN layers grown on GaAs [1] and can be explained by the much lower lattice mismatch for 3C-SiC/Si pseudo-substrates compared to GaAs substrates. Intrinsic SFs

are mainly bounded at the interface by 30° Shockley partial dislocations and rarely by sessile Lomer-Cottrell partial dislocations, the latter of which are found next to SiC step edges in the GaN/3C-SiC interface and hence are possibly initiated by these.

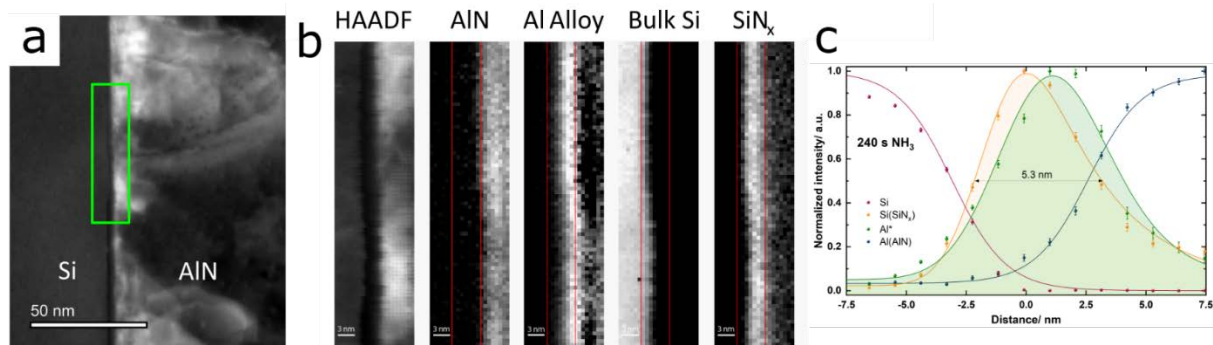
Based on our findings, we conclude that partial dislocations and intrinsic SFs either originate from the dissociation of perfect dislocations at the interface or that they directly form at the free surface as a partial dislocation half-loop. This highlights the importance of controlling the NL conditions for zb-GaN growth on 3C-SiC, to reduce the defect formation in the NLs, and consequently in the following zb-GaN thin films.

[1] A. Trampert, O. Brandt, H. Yang, and K.H. Ploog, Appl. Phys. Lett. **70**, 583 (1997).

Direct evidence of an Al alloyed SiN_x interlayer within an ammonia predosed AlN/Si interface via STEM-EELS

Simon M. Fairclough¹, Alexander M Hinz¹, Saptarsi Ghosh¹, Bogdan F Spiridon¹, David J Wallis^{1,2} and Rachel A. Oliver¹

¹Department of Material Science and Metallurgy, University of Cambridge, UK, ²Centre for High Frequency Engineering, University of Cardiff, UK



Gallium nitride (GaN) and its alloys (Aluminium[Al] and Indium) have shown great application within the electronic and optoelectronic fields due to their wide and tunable band gap, high defect tolerance within devices, high breakdown voltage and high saturation velocity.¹ A cost effective route towards these devices has been to grow GaN on Silicon (Si) substrates via metalorganic vapour phase epitaxy (MOVPE).² These structures show good performance compared to GaN devices on other¹ substrates such as sapphire or silicon carbide, but do require an aluminium nitride nucleation layer and a significant amount of subsequent strain management within the buffer layers to enable a low wafer bow and to prevent wafer cracking.²

Previous studies have shown that predosing the Si wafer surface with either trimethylaluminium (TMA) or ammonia before AlN growth can have an appreciable impact on wafer bow.³ Many questions still remain as to the importance and role of the predose in the growth of the AlN and subsequent strain management. Previous electron microscopy studies have inferred the formation of both amorphous and crystalline silicon nitride (SiN_x) interlayers, but with little compositional analysis due to the relatively large spatial resolution of electron dispersive x-ray spectroscopy (EDS).³ Other studies have used electron energy loss spectroscopy (EELS) which offers sub nm spatial resolution of the interface, and has been used to great effect for compositional analysis within TMA predose studies.^{4,5}

In this study we investigate a series of samples with different durations of ammonia predose via EELS, to not only probe the composition of the interface, but also to obtain chemical bonding information within this layer (Figure 1). Here we are able to show direct evidence of a SiN_x interlayer up to 5.3 nm thick with an ammonia predose time dependency, and for the first time highlight an Al alloying of the SiN_x.⁶

Fig. 1. a) A *High-angle annular dark-field* (HAADF) STEM image showing the AlN/Si interface of 240 second ammonia predosed sample. b) A live HAADF image of the green region in (a) with the corresponding deconvoluted AlN, Al Alloy, Bulk Si and SiN_x EELS signals within this region, c) Normalised intensity plot of the signals in (b) across the interface highlighting a 5.3nm SiN_x region that has been Al alloyed.

- [1] Amano, H. et al. The 2018 GaN power electronics roadmap. *Journal of Physics D: Applied Physics* vol. 51 163001 (2018).
- [2] Zhu, D., Wallis, D. J. & Humphreys, C. J. Prospects of III-nitride optoelectronics grown on Si. *Reports Prog. Phys.* **76**, 106501 (2013).
- [3] Li, Y. et al. Nucleation layer design for growth of a high-quality AlN epitaxial film on a Si(111) substrate. *CrystEngComm* **20**, 1483–1490 (2018).
- [4] Radtke, G., Couillard, M., Botton, G. A., Zhu, D. & Humphreys, C. J. Structure and chemistry of the Si(111)/AlN interface. *Appl. Phys. Lett.* **100**, 011910 (2012).
- [5] Radtke, G., Couillard, M., Botton, G. A., Zhu, D. & Humphreys, C. J. Scanning transmission electron microscopy investigation of the Si(111)/AlN interface grown by metalorganic vapor phase epitaxy. *Appl. Phys. Lett.* **97**, 251901 (2010).
- [6] Ghosh, S. et al. The origin(s) of anomalous substrate conduction in MOVPE grown GaN HEMTs on highly-resistive silicon. *Under Rev.*

Non-Radiative Recombination Centers in InGaN/GaN Core-Shell Nanorods Probed by Hyperspectral Cathodoluminescence Imaging

K Loeto¹, G Kusch¹, P-M Coulon², S Fairclough¹, P A Shields², R A Oliver¹

¹Department of Materials Science and Metallurgy, University of Cambridge, UK, ²Department of Electronic and Electrical Engineering, University of Bath, UK

Indium gallium nitride (InGaN) light-emitting diodes (LEDs) offer considerable luminous efficacy improvements when compared to traditional lighting sources such as fluorescent and incandescent lamps. However, conventional planar wurtzite InGaN LEDs suffer from polarisation fields inherent to the (0001) growth facet. These fields reduce the overlap integral of charge carriers in the quantum wells (QWs) – the quantum confined stark effect (QCSE) [1]. The QCSE lowers the internal quantum efficiency of such LEDs and hence the device efficiency. Core-shell nanorod (NR) structures expose non-polar {10-10} facets free from polarisation fields allowing QWs unaffected by the QCSE to be fabricated and potentially enhancing device efficiency [2]. However, as with their planar counterparts, NRs suffer from structural defects which can act as non-radiative recombination centers reducing device quality and efficiency. It is thus important to understand the origin and properties of these defects to control their incorporation and optimise the materials for their devices.

Cathodoluminescence (CL) hyperspectral imaging was used to study the optical properties of InGaN/GaN core-shell NRs. This involves exciting charge carriers within the NRs using a convergent and continuous beam of electrons with energy from 1 to 10 keV. Excited charge carriers recombine emitting photons whose integrated intensity, origin and energy are used to build up a hyperspectral CL map. The nanorods investigated were fabricated by a top-down etching and bottom-up facet regrowth hybrid process. Growth and regrowth were performed in a metal-organic vapour phase epitaxy (MOVPE) chamber.

By applying a digital band-pass filter to only observe the integrated intensity from GaN near-band-edge luminescence, at 3.39 eV, we observe a circular region of lower emission intensity at room temperature. This region correlates to the interface between initial etched GaN nanopillars and regrown GaN. The existence of this region indicates the presence of non-radiative recombination centres which can be from extended defects or point defects. From scanning transmission electron images of radial cross-sections of the NRs, no

extended defects were observed. Thus, we conclude that point defects are the origin of the lower intensity circular region. These point defects can act as a negative influence on the luminous efficacy of the LED structure as well as potential current sinks during the electric operation.

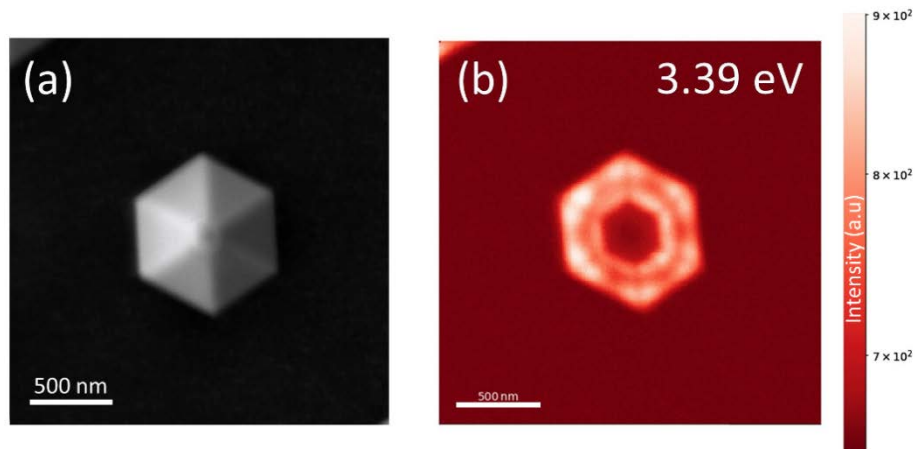


Fig. 2. (a) SEM image of a NR as imaged from above. (b) monochromatic CL map (centred at 3.39 eV) of NR in (a) taken at room temperature.

- [1] D. A. B. OMiller, et al, Phys. Rev. Lett. 53, 2173 (1984)
 [2] Emmanuel D. Le Boulbar, et al, Crystal Growth & Design 2016 16 (4), 1907-1916 y

Non-destructive imaging of residual strains in GaN and their effect on optical and electrical properties through correlative light-electron microscopy

Naresh-Kumar Gunasekar¹, Paul Edwards¹, Nouf-Allehiyani Mohammad¹, Bodhan Starosta¹, Benjamin Hourahine¹, Robert Martin¹, Carol Trager-Cowan¹, Tim Batten², Arantxa Vilalta-Clemente³, Angus Wilkinson³, Emmanuel Le Boulbar⁴ and Philip Shields⁴

¹Department of Physics, University of Strathclyde, UK, ²Renishaw plc, UK, ³Department of Materials, University of Oxford, UK, ⁴Department of Electronic and Electrical Engineering, University of Bath, UK

Understanding the nature of dislocations and their role in plastic deformations helps to better develop novel methods for producing technologically relevant electronic materials. Extended defects in as-grown semiconductor heterostructures are quite common, especially in the heteroepitaxial growth of thin films, irrespective of the growth methods and conditions. Screw dislocations for example, can alter the activation barrier for growth in the immediate surrounding areas and can be detrimental to electronic and optoelectronic devices [1]. Hence, measuring strain relaxation in lattice-mismatched heteroepitaxial semiconductor materials, for example GaN, provides great insight into dislocation formation [2]. We show a non-destructive approach to understanding the growth modes of a GaN thin film and simultaneously quantifying its residual strains and their effect on optical and electrical properties using correlative scanning electron microscopy techniques [3, 4] and Raman microscopy [5].

Figure 1 shows a correlative microscopy image revealing the distribution of dislocations and their effect on light emission. Coincident strain maps (see Fig. 2) derived from electron backscatter diffraction (EBSD) [6], cathodoluminescence (CL) and confocal Raman techniques reveal strain variations with similar direction and order of magnitude, especially in the proximity of dislocations. Correlating confocal Raman imaging with electron channelling contrast imaging (ECCI) suggests the distinctive pattern observed in the dislocations is the combined result of the underlying growth mask, movement of the dislocations along $\langle 11-20 \rangle$ during growth, and their propagation along the $\langle 0001 \rangle$ growth direction. The methodology presented in this work

can be adopted for any heteroepitaxial growth, in particular, those using selective masks on the growth substrates where the morphology influences the subsequent growth.

- [1] Y. Taniyasu, M.Kasu and T. Makimoto, *Nature*, **18** (2006) p. 325
- [2] D. Coopera, et al., *Micron*, **80** (2016) p. 145
- [3] G. Naresh-Kumar, et al., *Microsc. Microanal.* **20** (2014) p. 55
- [4] G. Naresh-Kumar, et al., *Nano Letters*, **19** (2019) p. 3863
- [5] T. Batten and M. Olga, *Mat. Sci. Forum.* **821**. Trans Tech Publications (2015) p. 229
- [6] A. J. Wilkinson, G. Meaden, and D. J. Dingley, *Ultramicroscopy* **106** (2006) p. 307
- [7] The authors acknowledge the support from the EPSRC grants “Quantitative non-destructive nanoscale characterisation of advanced materials” **EP/P015719/1**, “manufacturing of nano-engineered III-N semiconductors” **EP/M022862/1**, and “Nanoscale characterisation of nitride semiconductor thin films using EBSD, ECCI, CL and EBIC” **EP/J015792/1** and **EP/J016098/1**

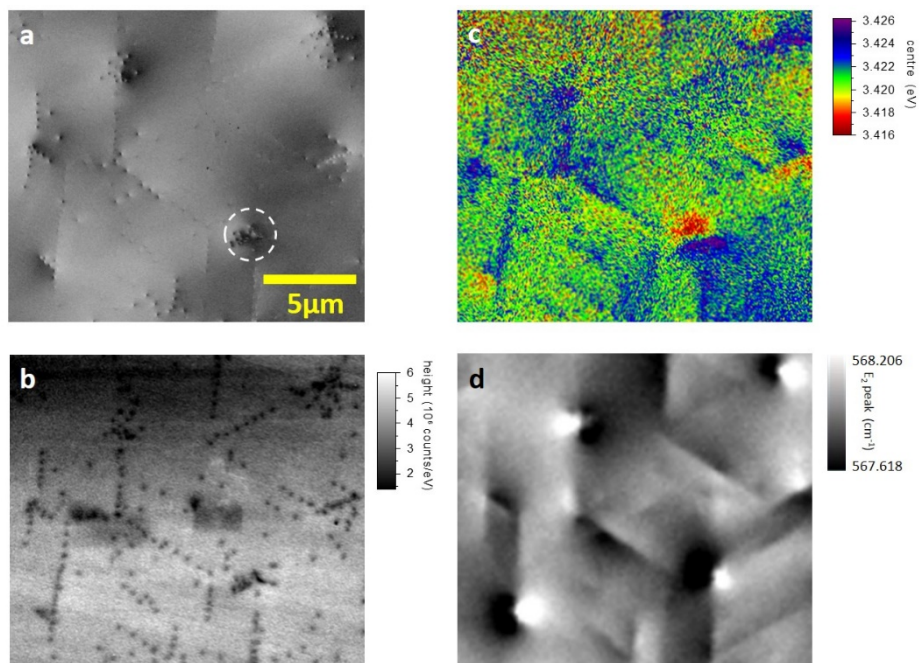


Fig. 1. Co-incident electron channelling contrast imaging (ECCI), cathodoluminescence (CL) and confocal Raman imaging from a GaN thin film. (a) ECCI micrographs showing threading dislocations (TDs) as black and white spots. (b) CL near band edge intensity map showing TDs as black spots, (c) CL peak fitted energy map showing compressive (blue region) and tensile strain (red region) on clusters of TDs and (d) Raman image collected $\approx 2 \mu\text{m}$ beneath the sample surface of the E_2 peak position showing the strain effect due to TDs similar to CL peak fitted energy map.

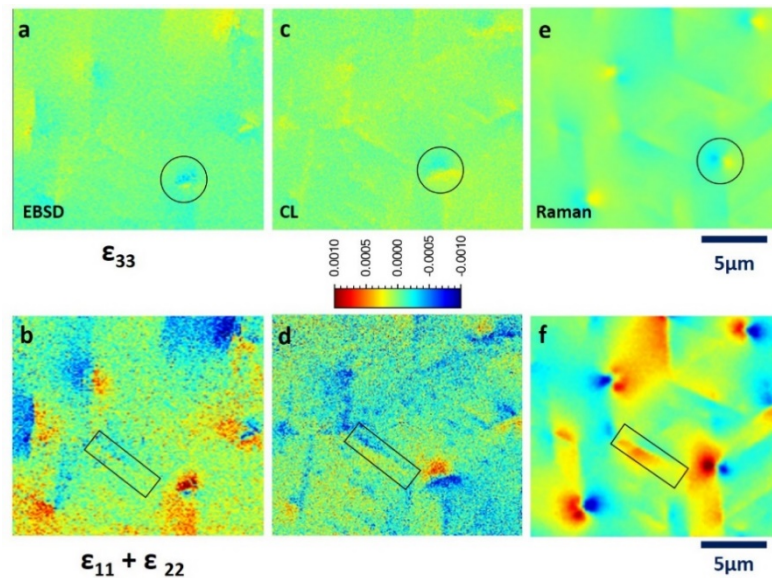


Fig. 2. Normal strains derived from electron backscatter diffraction (EBSD), CL and confocal Raman imaging. Top row images corresponds to residual strains along $\langle 0001 \rangle$ and bottom row images corresponds to residual strain $\langle 11-20 \rangle$ and $\langle 1-100 \rangle$. Strains derived from EBSD, out of plane strain (a) and in plane strains (b). Strains derived from CL, out of plane strain (c) and in-planes strains (d). Strains derived from Raman E_2 peak position map, out of plane strain (e) and in-planes strains (f).

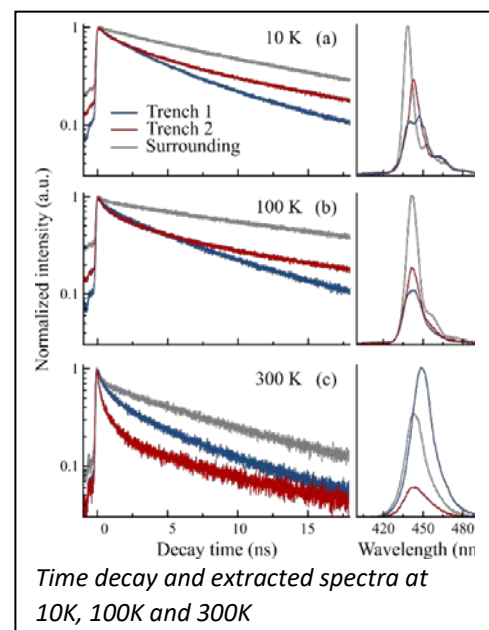
Carrier dynamics in and around trench defects in InGaN QWs probed by time resolved cathodoluminescence

G Kusch¹, Kagiso Loeto¹, E J Comish¹, S Hammersley³, M J Kappers¹, P Dawson¹, R A Oliver¹, and F C-P Massabuau^{1,2}

¹Department of Materials Science and Metallurgy, University of Cambridge, UK, ²Department of Physics, SUPA, University of Strathclyde, UK, ³Photon Science Institute, University of Manchester, UK

Heteroepitaxial growth of III-nitrides on substrates like Al₂O₃, Si and SiC typically results in the incorporation of defects. These defects can act as nonradiative recombination centres, reducing the performance of devices. Trench defects are one such defect found in InGaN/GaN quantum wells (QW), InAlGaN QWs and InGaN epilayers [1-3]. They have been shown to consist of an I1-type basal plane stacking fault located in the active region of the device which is bounded by a vertical stacking mismatch boundary that threads towards the surface and opens as a series of coalescing pits [1]. Trench defects display different and diverse emission properties compared to the material surrounding it [2,3].

Here, we present the use of temperature (10K-300K) and power (25 pA to 60 nA) dependent as well as time-resolved cathodoluminescence (CL) to study the emission and carrier dynamics of trench defects in InGaN/GaN 10 multiple QW structures grown by MOVPE. Spectra were extracted from hyperspectral maps recorded in CW mode such that the emission properties could be analyzed, while time-



Time decay and extracted spectra at 10K, 100K and 300K

traces were recorded with a time correlated single photon counting setup with a time resolution of ~ 100 ps.

Three different regions of interest were identified on the sample: unperturbed material and defects with a wide (Trench 1 ~ 50 nm) and narrow (Trench 2 ~ 30 nm) trench. Power dependent measurements at 300K showed the wide trench defects to be brighter than the surrounding material at low probe currents but to become darker at higher probe current. For these defects, a red-shift was observed under low probe currents compared to the surrounding material. No such shift was observed at high probe currents. Narrow trench defects remain darker than the surrounding material at all probe currents investigated. For the temperature-dependent time-resolved measurements (see Figure), the surrounding material shows the slowest decay at all temperatures investigated. At temperatures below 100K, the wide trench defects (Trench 1) show the fastest decay with the narrow trenches being intermediate. For temperatures above 100K, the narrow trench defects (Trench 2) now show the fastest decay with the wide trenches being intermediate.

Our CL results demonstrate that the carrier dynamics in the material enclosed within trench defects (in particular those of narrow trenches) is noticeably different from the carrier dynamics of the unperturbed material.

- [1] F. C.-P. Massabuau et al. Appl. Phys. Lett., **101**, 212107 (2012)
- [2] F. C.-P. Massabuau et al. J. Appl. Phys. **113**, 073505 (2013)
- [3] J. Bruckbauer et al. Appl. Phys. Lett. **98**, 141908 (2011)

Session 3: Modelling

Temperature dependence of radiative and non-radiative recombination rates in c -plane InGaN/GaN quantum wells

J M McMahon^{1,2}, D S P Tanner¹, E Kioupakis³, and S Schulz¹

¹Tyndall National Institute, University College Cork, Ireland, ²Department of Physics, University College Cork, Ireland, ³Materials Science and Engineering Department, University of Michigan, USA

The efficiency of light emitting diodes based on InGaN quantum wells (QWs) is affected by the competition of radiative and non-radiative processes. Sources of non-radiative recombination are Shockley-Read-Hall and Auger effects [1]. Given the importance of these factors for optoelectronic devices, experimental and theoretical studies have been directed towards understanding their fundamental properties in InGaN QWs. For instance, the experimental study by Nippert *et al.* [2] reported an unusual temperature dependence of the radiative recombination rate, often described by the so-called B coefficient. The experimental data indicated an increase in B with increasing temperature. Furthermore, experimental studies also show that the Auger recombination coefficient, C , increases with increasing temperature. While the increase in B with increasing temperature has been attributed to carrier localization effects, far less attention has been directed towards the theoretical analysis of the temperature dependence of the Auger coefficient, C , in InGaN/GaN QWs.

In this work we calculate both the radiative recombination coefficient, B , and the Auger coefficients, C_{eeh} and C_{hhe} , as a function of the temperature in c -plane In_xGa_{1-x}N QWs. These investigations have been carried out in the framework of an atomistic tight-binding model that accounts for random alloy fluctuations. Using the tight-binding wavefunctions, dipole and (direct and exchange) Coulomb matrix elements have been evaluated. Equipped with this information and the tight-binding eigenenergies, the radiative recombination coefficient and the Auger coefficients are directly calculated within this atomistic framework. For fixed In content, x , in the well, these calculations have been repeated several times for different microscopic configurations so that the impact of the alloy microstructure on the results is accounted for. Our

calculations show that carrier localization effects significantly affect the B coefficient at low temperatures. With increasing temperature energetically higher lying states are being populated, resulting in an increase of the dipole matrix elements and, as a consequence, an increase in B with increasing temperature [3]. The obtained data are in good agreement with the trends observed by Nippert *et al.* [2]. Furthermore, we find that the Auger coefficients, C_{eh} and C_{he} , also increase with temperature, revealing good agreement with experimental data [2]. Finally, we find that the B/C ratio decreases with increasing temperature, indicating that the Auger rate increases faster with temperature than the radiative rate.

- [1] A. David, N. G. Young, C. Lund and M. D. Crave, ECS J. Solid State Sci. Technol. **9** 016021 (2020)
- [2] F. Nippert, S. Y. Karpov, G. Callsen, B. Galler, T. Kure, C. Nenstiel, M. R. Wagner, M. Straßburg, H.-J. Lugauer, and A. Hoffmann, Appl. Phys. Lett., **109**, 161103 (2016)
- [3] J. M. McMahon, D. S. P. Tanner, E. Kioupakis, and S. Schulz, Appl. Phys. Lett., **116**, 181104 (2020)

Impact of random alloy fluctuations on inter-well transport in InGaN/GaN multi-quantum well systems

M O'Donovan^{1,2}, M Luisier³, E P O'Reilly^{1,2}, and S Schulz¹

¹Tyndall National Institute, University College Cork, Ireland, ²Department of Physics, University College Cork, Ireland, ³Integrated Systems Laboratory, ETH Zürich, Switzerland

InGaN-based quantum wells (QWs) have found widespread applications in light emitting diodes operating in the visible spectral range [1]. However, to exploit the full potential of these devices, understanding and tailoring their fundamental properties is of key importance. Here, the impact of alloy fluctuations, in particular on hole transport properties, has attracted considerable attention. Recent experimental studies have shown that ballistic hole transport can play an important role in InGaN multi-QW (MQW) systems [2]. However, targeting this question from a theoretical perspective is challenging, since ideally a fully quantum mechanical model that operates on atomistic electronic structure theory is required.

In this work we target ballistic electron and hole transport by combining an atomistic tight-binding (TB) model with non-equilibrium Green's function (NEGF) theory. The TB model accounts for (random) alloy fluctuations and connected fluctuations in strain and built-in fields [3]. Transport properties are calculated by coupling the TB Hamiltonian (containing all the atomistic effects of alloy fluctuations) to the NEGF solver OMEN [4].

In order to investigate the impact of alloy fluctuations on electron and hole ballistic transport properties in InGaN MQW systems, we compare results of a virtual crystal approximation (VCA) with data where random alloy fluctuations are explicitly considered. Special attention is paid to the impact of (i) the nitride-specific built-in field, (ii) the presence of a p-i-n junction induced field and (iii) the barrier width in c -plane InGaN MQW systems. Overall, our calculations show that electron ballistic transport is not greatly affected by alloy fluctuations (see Fig. 1 left). The alloy microstructure mainly leads to an energetic broadening of transmission peaks. Thus, VCA provides a reasonably good description of electron transmission properties.

For hole ballistic transport a different behavior is observed. We find that in general the presence of (random) alloy fluctuations opens up extra transmission channels which are not found in a VCA (see Fig. 1 right). We attribute these extra channels to the fact that introducing random alloy fluctuations leads to strong hole localization effects and that in turn k -vector conservation between different states contributing to the transport is no longer required. However, these channels do not necessarily stem from QW related states; they rather involve states energetically near the barrier valence band edge. Also we find that the presence of the extra channels strongly depends on the interplay of built-in field and barrier width. Overall, with increasing barrier width the hole ballistic transport is strongly reduced through states near the valence band edge (see Fig. 2 right). A reduction of hole ballistic transport has also been seen in recent experimental studies [2].

- [1] C.J. Humphreys, MRS Bulletin, **33**, (4), p. 459470 (2008)
- [2] S. Marcinkevičius, R. Yapparov, L. Y. Kuritzky, Y.-R. Wu, S. Nakamura, and J. S. Speck, Phys. Rev. B, **101**, p. 075305 (2020)
- [3] S. Schulz, M. A. Caro, C. Coughlan, and E. P. O'Reilly, Phys. Rev. B, **91**, p. 035439 (2015)
- [4] M. Luisier, A. Schenk, W. Fichtner, and G. Klimeck, Phys. Rev. B, **74**, p. 205323 (2006)

Supplementary information

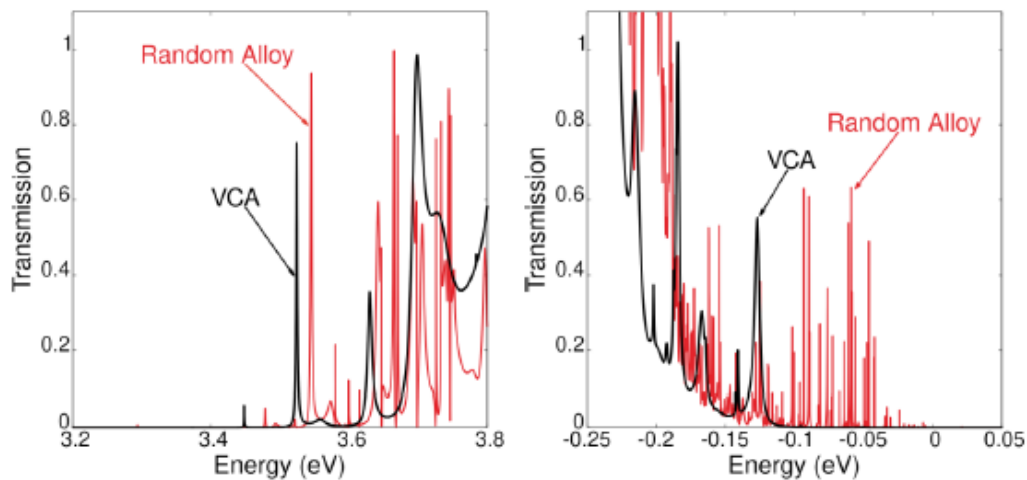


Fig. 1. VCA vs. random alloy calculation for (left) electrons and (right) holes through a 4 QW system with 3.1 nm barriers. The supercell dimensions are $4.4 \times 3.9 \times 28.8$ nm³, containing 43,904 atoms. The left figure shows a good agreement between VCA and random alloy calculations. Thus localization effects are of secondary importance for describing transmission properties of electrons, though different configurations will give rise to peaks at different energies, leading to a spectral broadening. The right figure reveals noticeable differences between VCA and random alloy calculations. The random alloy result shows many extra channels which contribute to transmission through the MQW structure. This is due to the breaking of \mathbf{k} as a quantum number, where \mathbf{k} -conservation is no longer limiting the transmission.

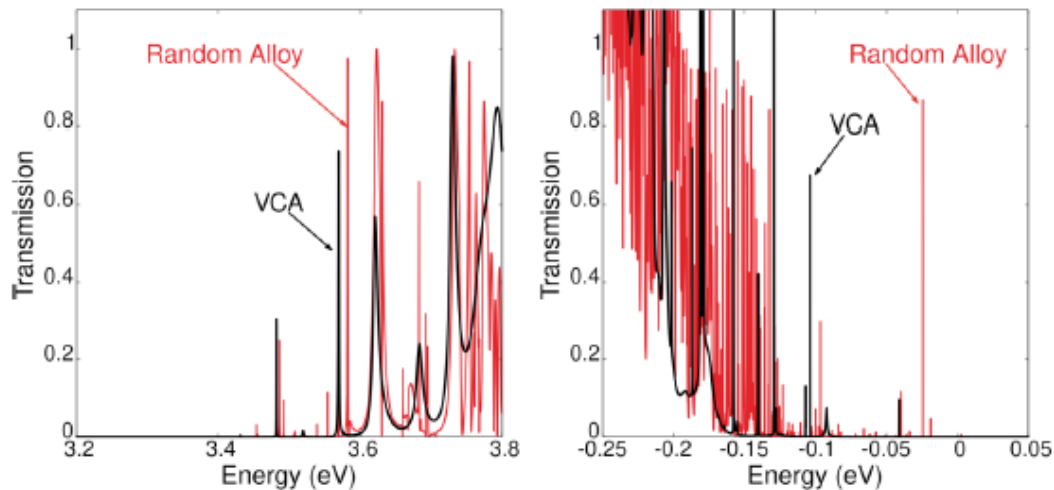


Fig. 2. VCA vs. random alloy calculation through a 4 QW system with 5.2 nm barriers. The supercell dimensions are $4.4 \times 3.9 \times 34.6$ nm³, containing 59,585 atoms for (left) electrons and (right) holes. The left figure shows a good agreement between VCA and random alloy calculation results. The right figure reveals a reduction in the extra channels found for the thinner barrier (see Fig. 1 right) in random alloy calculation when compared to a VCA. This is attributed to the widening of the barrier, which reduces the interaction between the hole states.

Session 4: The Humphreys Lecture

Exploring (and exploiting) the physics of ultra-wide-bandgap nitrides

Chris G Van de Walle

University of California, USA

We are entering the era of ultra-wide-bandgap semiconductors, with band gaps significantly wider than the 3.4 eV of GaN. These materials will enable deep-UV optoelectronics and have compelling advantages in high-power and RF electronics, quantum information science, and extreme-environment applications. I will talk about our studies of AlN, BN and alloys with other nitrides using first-principles calculations based on hybrid density functional theory.

The wurtzite-structure nitride semiconductors, AlN, GaN, and InN, are well established as key materials for solid-state lighting and power electronics. BN is being newly explored as a member of this family. BN prefers the hexagonal or zinc-blende forms; however, alloys between BN and AlN or GaN can be stabilized in the wurtzite structure. The large lattice mismatch between the constituent materials affects the stability and electronic structure of BAlN and BgAN alloys. We determine band alignments and polarization properties. I will discuss the impact of point defects as well as intentional and unintentional impurities, the impact on nonradiative recombination, and applications in quantum information science.

Work performed in collaboration with A. Alkauskas, C. Dreyer, L. Gordon, A. Janotti, J. Lyons, M. Maciaszek, M. Macko, J. Shen, M. Turiansky, J. Varley, L. Weston, D. Wickramaratne, and Q. Yan, and supported by NSF, AFOSR, and DOE.

Friday 8 January

Session 5: The Foxton Lecture

GaN for display applications enabled by transfer printing

Brian Corbett, Zeinab Shaban, Rory Cahill, Juan Morales, Tanmay Mondal, Muhammet Genc, Jack Browne and Zhi Li

Tyndall National Institute, Ireland

Gallium nitride light emitting diodes (LEDs) have changed how we light our homes forever. A next big commercial opportunity is in displays with many challenges to be faced on how to control and deliver the light to the variety of display configurations. This talk first describes how stimulated emission in superluminescent LEDs acts as an efficient source of watt-scale high brightness light. We then look at the development of microLEDs and how the technique of transfer printing enables effective assembly of multicolour displays.

Poster session

P1 Light emission from Zn-doped InN colloidal quantum dots

Simon M Fairclough¹, Peter N Taylor², Charles T Smith³, Pip C J Clark⁴, Stefan Skalsky⁴, Ruben Ahumada-Lazo⁴, Edward A Lewis⁵, Daniel J Tate⁶, Ben F Spencer⁵, Mary BurkittGray¹, Igor Piš⁷, Federica Bondino⁸, Patrick Bergstrom-Mann¹, Sadie Carter-Searjeant¹, Michael L Turner⁶, David J Binks⁴, Sarah J Haigh⁵, Wendy R Flavell⁴, Richard J Curry³, and Mark A Green¹

¹Department of Physics, King's College London, UK, ²Sharp Life Science (EU) Ltd., UK, ³Photon Science Institute and Department of Electrical and Electronic Engineering, The University of Manchester, UK ⁴Photon Science Institute and Department of Physics and Astronomy, University of Manchester, UK, ⁵Department of Materials, The University of Manchester, UK, ⁶Department of Chemistry, The University of Manchester, UK, ⁷Elettra-Sincrotrone Trieste S.C.p.A, Italy, ⁸IOM CNR, Laboratorio TASC, Italy

Group III-Nitride semiconductors typically grown by chemical vapor deposition or molecular beam epitaxy on wafer substrates have been extensively used as active materials in optoelectronic applications, like solid state lighting, because their intrinsic band gaps can be tuned from the infrared (IR) to the ultraviolet (UV) by altering their alloyed composition and by quantum confinement. The realisation of high quality colloidal III-Nitride nanocrystals will further extend their applicability by offering non-toxic alternatives for existing quantum dot (QD) materials used in photovoltaics, light emitting diodes (LEDs), medical imaging and biosensing. However, producing stable, high-quality, monodisperse III-Nitride samples, showing high efficiency photoluminescence (PL) by means of safe colloidal synthesis routes with suitable precursors remains a challenge 1,2.

In this work, we present InN colloidal QDs doped with zinc, which has been observed to improve the optical properties in InP and InAs nanoparticles 2 and increase the tuneability in GaN colloidal QDs 3. The emission from these Zn-doped InN colloidal QDs is widely tuneable in the visible and near IR by the synthesis reaction time and quantum yields of up to ~30% are obtained with an In:Zn ratio of 1:2 (InZn2N). The PL lifetimes are of the same order of magnitude of those previously reported for GaN 3 and Zn3N2 4 colloidal QDs (Figure 1). Air stability and the emission quantum yield are further improved by producing core/shell/shell structures with both GaN and ZnS as capping layers. In addition, proof-of-concept QD-LEDs based on these improved materials are demonstrated with a turn on voltage of 2 V and an estimated external quantum efficiency (EQE) of 10-3 % 2.

References

- [1] Chen, Z., Sun, C., Wei, G. & Chen, Z. Colloidal III-V Nitride Quantum Dots. in *Nonmagnetic and Magnetic Quantum Dots* 61–75 (IntechOpen, 2017). doi:10.5772/intechopen.70844.
- [2] Fairclough, S. M. *et al.* Photo- and Electroluminescence from Zn-Doped InN Semiconductor Nanocrystals. *Advanced Optical Materials* **2000604**, 1–9 (2020).
- [3] Choi, Y. C. *et al.* Blue Emission of α -GaN Colloidal Quantum Dots via Zn Doping. *Chemistry of Materials* **31**, 5370–5375 (2019).
- [4] Ahumada-lazo, R. *et al.* Confinement Effects and Charge Dynamics in Zn₃N₂ Colloidal Quantum Dots: Implications for QD-LED Displays. *Applied Nano Materials* **2**, 7214–7219 (2019).

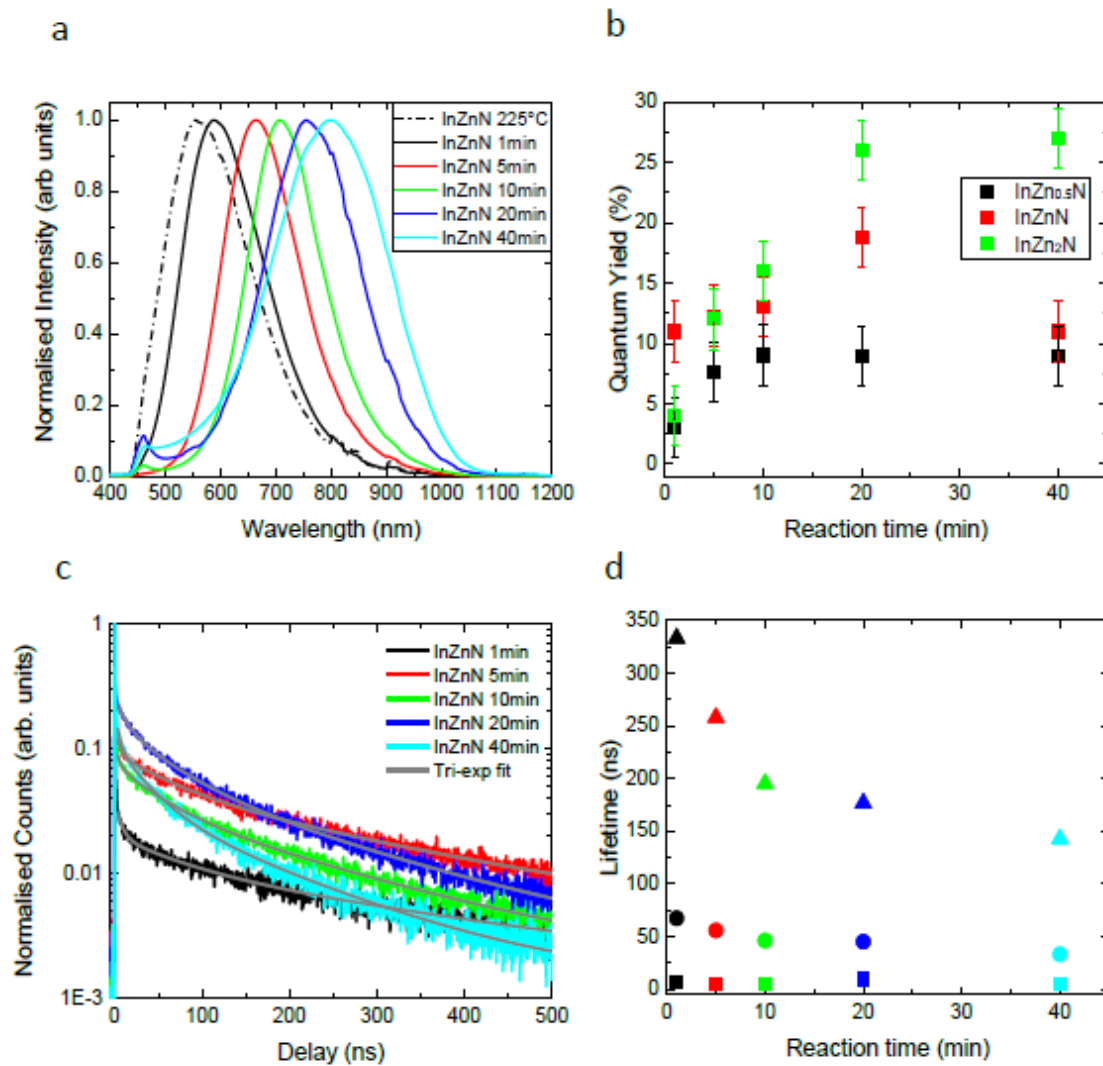


Fig. 1. a) Photoluminescence (PL) emission spectra, b) PL quantum yields (QY) for different In:Zn ratios, c) PL decays and d) PL lifetimes as a function of synthesis reaction time (size) for Zn-doped InN colloidal quantum dots.

P2 Employing a CMOS-Integrated GaN μ LED array to generate superimposed pulse amplitude modulation for optical camera communications

N Bani Hassan, M J Strain, M D Dawson, J Hermsdorf

Institute of Photonics, University of Strathclyde, UK

We present an application of Gallium-Nitride (GaN) micro-LED arrays, which enables superimposed m -ary pulse amplitude modulation for non-line-of-sight rolling-shutter-based optical camera communications. A bit error rate of 2.2×10^{-4} at a data rate of 16000 bps was achieved using a micro-pixel light emitting diode array and 4-ary pulse amplitude modulation.

Keywords—optical camera communications, discrete pulse amplitude modulation, LED array.

I. INTRODUCTION

Optical camera communications (OCC) is a technique, which combines the image capture function of a camera with its capabilities as a data receiver, and takes advantage of light-emitting diode (LED) lighting. Since GaN LEDs have fast switching speeds, the data rate in OCC is limited normally to the frame rate of the camera. The rolling shutter (RS) effect in complementary metal oxide semiconductor (CMOS) image sensors has been exploited to significantly increase the achievable data rate in OCC by mapping temporal variations in the LED intensity into spatial fringes. Moreover, complex modulations such as m -ary quadrature amplitude and phase (m QAM) [1] and m -ary pulse amplitude modulation (m PAM) [2] can boost the data rate to $\log_2 m$ times the frame rate of the camera. In the case of m PAM, the variations in the light intensity in the RS mode forms multiple bands with different brightness, see Fig. 1(a). However, complex modulation schemes require a digital to analog converter (DAC) to generate the electrical signal. Gallium-Nitride (GaN) micro-LED (μ LED) arrays provide an elegant method to remove the need for a DAC through generation of an analog signal by superimposing the intensity of individual digitally addressed LEDs, also referred to as digital-to-light conversion (DLC) [3, 4]. In this paper, we demonstrate a DLC technique for PAM similar to [3] for non-line-of-sight RS-based (NLOS) OCC.

II. SYSTEM MODEL

Figure 1(a) illustrates the schematic system model used for this work. A GaN μ LED array with a size of $M \times N$ transmits the optical information and a lens system projects the light onto a wall/screen in defocused mode. At the receiver side, an RS camera with a resolution of $U \times V$ captures the variations in the intensity of the reflected light, i.e., a $(M \times N) \times V$ non-imaging MIMO link at each time instant. Every symbol of the data generated in m PAM modulation is mapped to binary forming $\log_2(m)$ bits/symbol. Each bit is sent to a separate column of the LED array corresponding to its bit value. On the LED array, all LEDs within one column transmit the same data but independent of other columns (labelled c_1 , c_2 , and c_3 in Fig. 1(b)). Note, the sum intensities (SIs) of transmitting columns are different corresponding to the bit value and a power of 2 times the column with lowest SI. That is, the column with lowest SI transmits the least significant bit, while the most significant bit is transmitted by the columns with the SI of $m/2$ times the lowest SI. As a result, a m -level illumination pattern is formed on the wall by aggregating the illumination of different columns, representing the same symbol of the generated PAM signal. Note, it is essential that Tx optics create a highly defocused footprint on the wall/screen so that the footprint of all LEDs fully overlap. Accordingly, at each time-step, labelled t_1 , t_2 , and t_3 in Fig. 1(b), a striped pattern with discrete multi-level illumination is captured, see Fig. 1(c). The images taken are next processed to extract the data. In order to improve the signal to noise ratio (SNR), we element-wise average the values of all columns. However, this imposes distortion to the signal due to the shape of the footprint and illumination pattern. To compensate for the distortion, a picture of the footprint with no AC signal is taken to obtain a calibration curve. Next, we element-wise divide the received signal by the calibration curve; see Fig. 1(d). The SNR at the edges of the footprint is very low and dividing by a small number imposes a high noise level. Therefore, we truncate the

signal on both sides to ensure a reasonable SNR for the received signal. Note, this method can also be implemented in line-of-sight OCC, provided that a large defocused footprint of the light source can be created on the image sensor.

III. RESULTS

We evaluated the proposed concept experimentally. The system setup comprised a 16×16 flip-chip bonded array of GaN μ LEDs with 100- μ m pitch, 72- μ m pixel diameter, a bandwidth of 110 MHz, and a peak intensity at 410 nm; a camera lens with a FoV of ~ 4.5 degree; a white wall; and an iPhone-7-plus wide-angle rear camera. The camera, the LED array and the optics were positioned at a height of 25 cm from the base, all facing towards the wall, creating an NLOS link. The ISO and exposure time of the camera was set to 1760 and 125 μ s, respectively, and the resolution of the camera was 3024×4032 . To obtain the calibration curve, we took 20 pictures of the footprint with no AC signal on and took an average over the pictures and the columns. This ensures a reduced temporal noise standard deviation, hence a low noise calibration curve with a size of 3024×1 . We generated 4000 bits in 4-PAM format and passed it to the system in 10-symbol long packets and captured 1000 JPG images of the footprint. For each image, an average over all columns was taken, leaving an array with a size of 3024×1 . This array is then elementwise divided by the calibration curve. Figure 2 (a)-(c) show the eye diagram of the 4-level received signal for R_s of 2000, 4000, and 8000 symbol/s, respectively. We sample at the maximum eye opening to minimise the impact of inter-symbol interference (ISI). We measured the mean and standard deviation of each level and estimated the bit error rate as 9.5×10^{-8} , 9.2×10^{-8} , and 2.2×10^{-4} , respectively, which are all below the 7% forward error correction limit of 3.8×10^{-3} . Therefore, we achieved a data rate of 16 kbps. Note, the eye closes as the R_b increases. This is due to the ISI imposed by the exposure time, i.e., to open the eye a shorter exposure time must be used at a cost of reduced SNR.

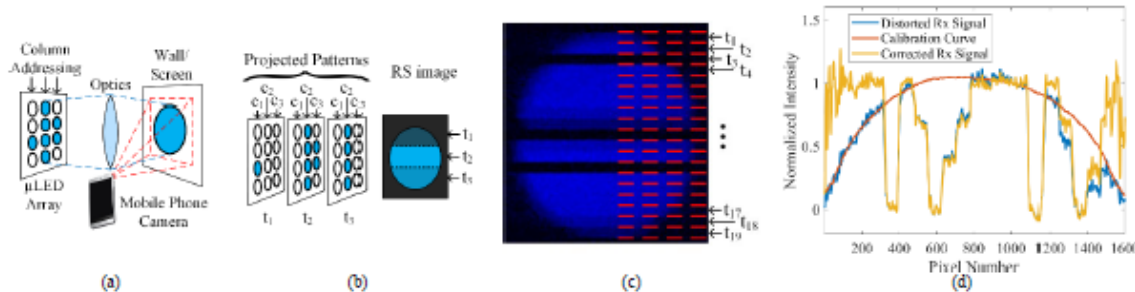


Fig. 1. (a) Schematic of the setup, (b) illustration of discrete PAM encoding and received image with RS effect, (c) experimental result, where the horizontal red lines indicate symbol boundaries, (d) Normalized intensity as a function of pixel number for the received signal.

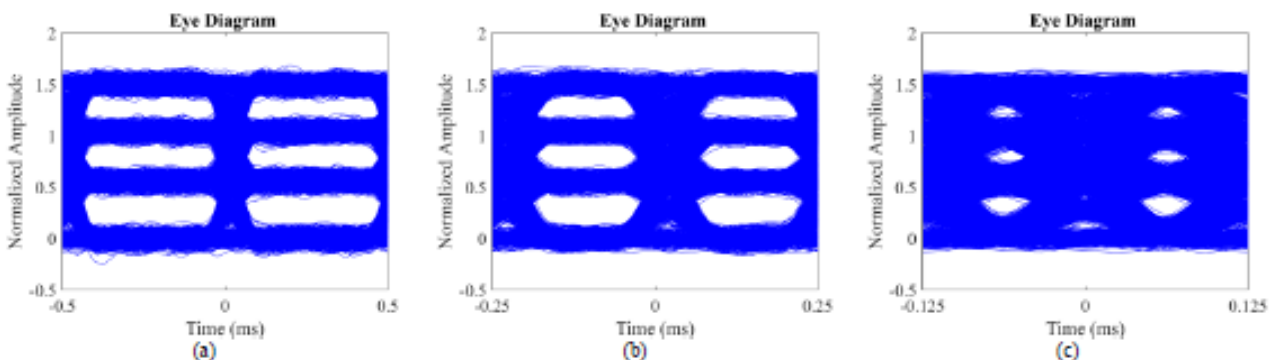


Fig. 2. Eye diagram of the received signal for R_b of (a) 2 ksymbol/s, (b) 4 ksymbol/s, and (c) 8 ksymbol/s.

IV. CONCLUSION

In this paper, we demonstrated experimentally that GaN μ LED arrays in any format that allows column-wise addressing at kHz rates are excellently suited to enable superimposed pulse amplitude modulation, which relaxes the requirement for a DAC. Using this technique, we improved the data rate by a factor of 2 compared with conventional RS-OCC using OOK modulation schemes.

ACKNOWLEDGMENT

This work was funded by EPSRC grant EP/S001751/1 and data are available at <https://doi.org/10.15129/de7b702f-aa64-4752-9756-d24f96c19d58>.

REFERENCES

- [1] T. Nguyen, M. D. Thieu, and Y. M. Jang, "2D-OFDM for optical camera communication: Principle and implementation," *IEEE access*, vol. 7, pp. 29405-29424, 2019.
- [2] V. P. Rachim and W.-Y. Chung, "Multilevel intensity-modulation for rolling shutter-based optical camera communication," *IEEE Photonics Technology Letters*, vol. 30, pp. 903-906, 2018.
- [3] A. D. Griffiths, M. S. Islim, J. Herrnsdorf, J. J. McKendry, R. Henderson, H. Haas, *et al.*, "CMOS-integrated GaN LED array for discrete power level stepping in visible light communications," *Optics express*, vol. 25, pp. A338-A345, 2017.
- [4] N. B. Hassan, M. Strain, M. Dawson, and J. Herrnsdorf, "Discrete Power-Stepping Pulse Amplitude Modulation for Optical Camera Communications Employing a CMOS-Integrated GaN μ LED Array," in *2020 IEEE Photonics Conference (IPC)*, pp. 1-2.

P3 Effects of Ammonia Substrate Pretreatment on the Strain Management in GaN-on-Si Structures

Alexander M Hinz, Simon M Fairclougha, David J Wallisa,b, and Rachel A Olivera

Department of Materials Science and Metallurgy, University of Cambridge, and Centre for High Frequency Engineering, University of Cardiff, UK

With the maturing of GaN-on-Si technology there is an increasing interest in the fabrication of advanced devices like micro-LEDs and membrane based sensors. However, these devices require a complete or partial removal of the Si substrate. The large thermal expansion and lattice mismatch in the GaN-on-Si system usually necessitate the growth of elaborate strain management layer stacks between the inexpensive Si substrate and the GaN epilayer. Thus, upon removal of the Si substrate the remaining layer stack will deform to compensate for the loss of the balancing force provided by the Si substrate. Therefore, the strain management layer stack has not only to be optimised such that the GaN epilayer remains crack free and the wafer bow, before the Si removal, falls within the processing specifications, but also should minimise the deformation of the layer stack after removal of the Si substrate to facilitate further processing. This requires an understanding of the strain management layer stacks and control of their growth that goes well beyond the level required for standard GaN-on-Si structures.

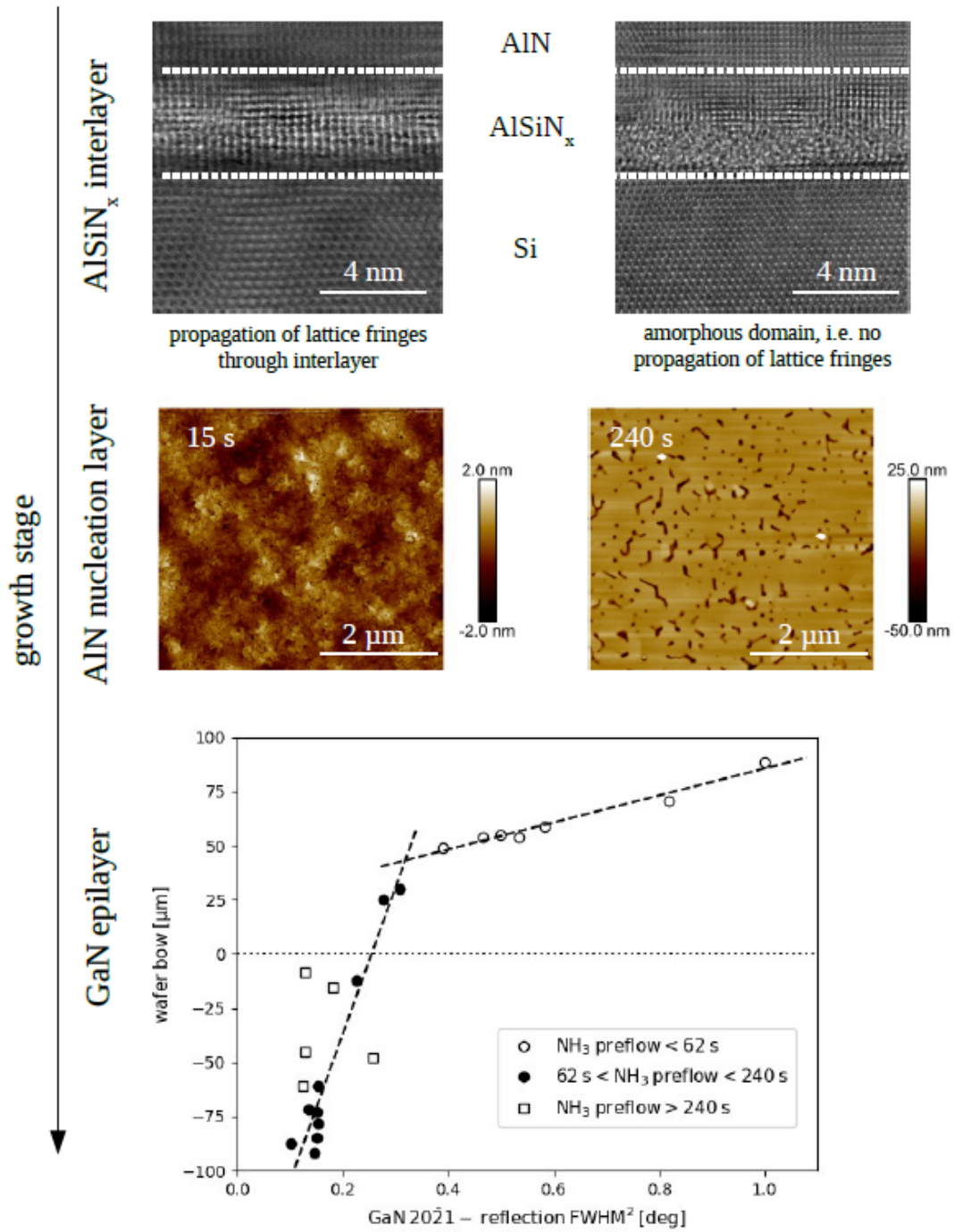
This contribution will give an update on an ongoing investigation of the effects of an ammonia substrate treatment on the strain management in GaN-on-Si structures. It will be shown that the final wafer bow of a 6" GaN-on-Si structure can be controlled within a range of 90 μ m concave to 90 μ m convex by simply varying the duration of the ammonia substrate treatment. High resolution X-ray diffractometry revealed a correlation of the final wafer bow with the ω -FWHM of the 2021 GaN epilayer reflection. The correlation can be subdivided into two distinct regions. Initially the wafer bow becomes less concave with decreasing ω -FWHM.

At an ω -FWHM of around 1800 arcsec the transition from concave to convex wafer bows accelerates substantially and continues until a maximum convex wafer bow is reached. However, this correlation between the ω -FWHM of the 2021 GaN epilayer reflection and the wafer bow is only valid for small treatment times. For large treatment times the correlation breaks down.

To gain a better understanding of the pretreatment's effect on the epitaxial growth the AlN nucleation layer and its interface with the Si substrate have been studied in more detail. For all treatment durations a SiNx interlayer is formed between the Si and the AlN nucleation layer that also appears to contain significant amounts of Al. Thus we will refer to this layer as an AlSiNx-layer. The thickness of the interlayer increases with the treatment duration up to a thickness of a few nm.

However, high resolution TEM revealed that even in thick interlayers a significant amount of regions can be found in which lattice fringes propagate from the Si substrate into the AlN nucleation layer. Most likely these regions contain highly defective AlN that maintains the epitaxial relationship between the Si substrate and the AlN nucleation layer that is grown on the otherwise amorphous AlSiNx interlayer. Furthermore, AFM scans of the AlN nucleation layer's top surface showed that with increasing treatment duration the nucleation layer is less coalesced. As the AlN growth parameters are not intentionally changed, this suggests that a longer pretreatment reduces the AlN nucleation density by inducing changes in the AlSiNx interlayer. This reduction in the nucleation density is also reflected in a reduction of the ω -FWHM of the AlN nucleation layer 2021 reflection. A delayed coalescence would enhance dislocation bending during the growth of the nucleation layer. It appears that ultimately this lower defect density is propagated into the strain management stack and the GaN epilayer resulting in a change of the wafer bow.

Graphical Abstract



P4 HAX-PES measurements of InGaN/GaN heterostructures using a lab-based x-ray source

S A Church¹, B Spencer¹, M J Kappers², M Frentrup², D J Wallis^{2,3}, R A Oliver² and D J Binks¹

¹Department of Physics and Astronomy & Photon Science Institute, University of Manchester, UK,

²Department of Materials Science & Metallurgy, University of Cambridge, UK, ³Centre for High Frequency Engineering, University of Cardiff, UK

X-ray photoelectron spectroscopy (XPS) provides detailed chemical information regarding a material by measuring the binding energy of emitted electrons when exposed to an X-ray source [1]. This can be used to identify and quantify the elemental species, as well as determine the chemical bonds which they form [1]. Conventionally, lab based XPS experiments use “soft” X-rays (typically 1500 eV), and are sensitive only to the material surface. To obtain information from 10’s nm within the sample, HARd X-ray PhotoElectron Spectroscopy (HAX-PES) is performed, with photon energies around 10 keV.

HAX-PES allows the measurement of depth profiles by changing the angle of emission of the photoelectrons [2]. These experiments are sensitive to the degree of band bending in the material, which manifests as a shift in the binding energy of the electrons [2]. HAX-PES is therefore a useful technique to study III-N semiconductors, which typically have strong polarisation fields and surface band bending [3]. In recent years, this has been applied to GaN epilayers to directly measure the surface band bending profile in the top 10 nm [2], and this has been applied to understand surface damage caused by etching techniques [4]. However, these previous studies of HAX-PES on GaN have utilised synchrotron beam lines as the “hard” x-ray source. Due to the high demand and high cost for time on these beamlines, this has limited the scope of investigations using the technique.

In this paper, we report preliminary HAX-PES measurements on InGaN/GaN heterostructures using a state-of-the-art lab based “hard” X-ray source (HAXPES-Lab, ScientaOmicron GmbH). An example “soft” XPS spectrum is shown in Figure 1, with a HAXPES spectrum of the sample shown in Figure 2 for comparison. The XPS spectrum exhibits peaks originating from the core levels of Ga, as well as from O and C, indicating surface contamination. In the HAXPES spectrum the contaminant signals are significantly reduced, and core levels from In are present. This indicates that the measurement is less sensitive to the surface and can detect electrons from buried layers which contain indium. These results demonstrate that lab-based HAX-PES measurements are able to probe into the bulk of the material, which can enable detailed systematic investigations to be carried out without the need for synchrotron beam lines.

[1] J E Bowen Katari J. Phys. Chem. 1994, 98, 4109-4117.

[2] S. Ueda *Appl. Phys. Express*, 2018, **11** 105701.

[3] F. Bernardini and V. Fiorentini, Phys. Rev. B 1997, **56**, R10024(R).

[4] D. Kikuta et al. R&D Review of Toyota CRDL, 2015, 46, 3, 43-50.

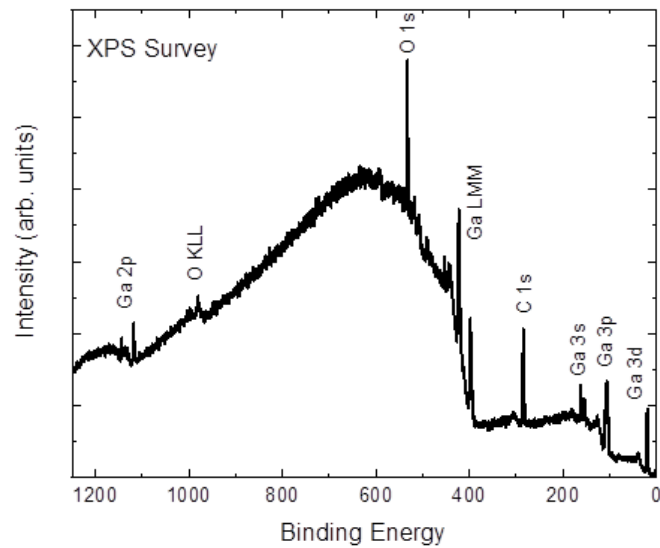


Fig 1. A “soft” XPS spectrum of an InGaN/GaN heterostructure using an x-ray energy of 1.5 keV (Al $K\alpha$). This sample contains a 2.7 nm InGaN QW 5nm from the sample surface and a 24 nm InGaN underlayer 10.7nm from the surface. Only core levels from Ga and surface contaminants are observed due to the surface sensitivity of the technique, and the N 1s core level is obscured by Ga Auger peaks.

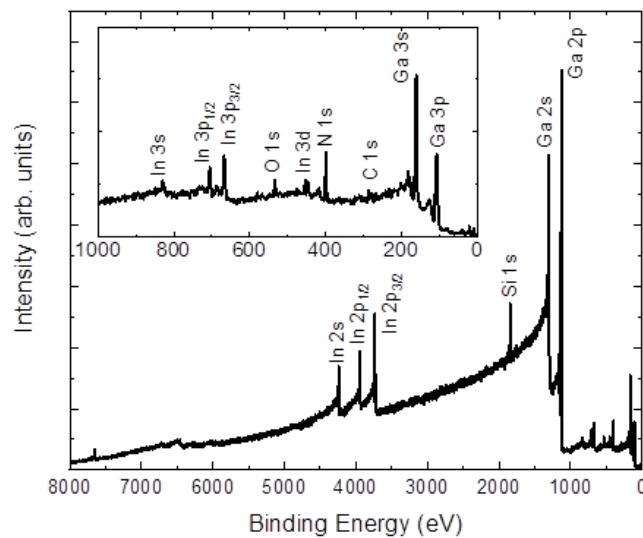


Fig 2. A HAX-PES spectrum of the same heterostructure as in Figure 1 using an x-ray energy of 9250 eV (Ga K), inset is the same spectrum zoomed in on the first keV. Many In core levels are observed, and the Auger peaks no longer overlap N 1s.

P5 The effects of thermal annealing on the optical properties of Mg-doped zinc-blende GaN

D Dyer¹, S A Church¹, M Jain², M J Kappers³, D J Wallis^{2,3,4}, R A Oliver³, and

D J Binks¹

¹Dept. of Physics and Astronomy & Photon Science Institute, University of Manchester, UK, ²Kubos Semiconductors Ltd., Future Business Centre, UK, ³Department of Materials Science and Metallurgy, University of Cambridge, UK, ⁴Centre for High Frequency Engineering, University of Cardiff, UK

LEDs based on InGaN/GaN quantum wells (QWs) grown in the wurtzite (wz) crystal phase can exhibit an external quantum efficiency (EQE) of >80% when emitting in the blue; in contrast, the EQE of similar green- or amber-emitting devices is significantly lower, typically 20-50%¹. This decrease in EQE has been attributed to the consequences of the higher indium content needed to achieve longer wavelength emission, such as the increased polarisation fields across the QWs reducing the wavefunction overlap between carriers and thus the radiative recombination rate, and a greater concentration of non-radiative defects due to the lower growth temperatures required². However, InGaN/GaN QWs can also be grown in the zincblende (zb) phase, which has several potential benefits. When grown along the (001) direction, there are no polarisation fields across zb-InGaN/GaN QWs due to the greater crystal phase symmetry³. Moreover, the band gap of zb-GaN is 0.2 eV lower than that of wz-GaN reducing the indium content required for green emission⁴, despite the absence of the quantum confined Stark effect seen in wz-InGaN/GaN QWs⁵.

In wz-GaN LEDs, p-type layers are produced by Mg doping, followed by thermal annealing to free Mg from electrically inactive Mg-H complexes that form during growth⁶. As a step toward realising zb-InGaN/GaN LEDs, the effect of thermal annealing on the optical properties of Mg-doped zb-GaN epilayers has been investigated. Samples were grown by MOCVD on 3C-SiC/Si substrates with a Mg concentration of $1.7 \times 10^{19} \text{ cm}^{-3}$, as measured by secondary ion mass spectrometry, and annealed at 740°C in N₂. The photoluminescence (PL) spectrum obtained at 10 K for continuous wave laser excitation at 325 nm, shown in figure 1 is dominated by a broad blue emission band, which is similar to the blue band (BB) observed in Mg-doped wz-GaN and attributed to donor-acceptor pair recombination⁷; a similar observation has been reported previously for MBE-grown Mg-doped zb-GaN⁸. After annealing, the BB intensity increased by a factor of about eight, consistent with a greater concentration of the participating acceptor species and/or a reduction in competing processes. Figure 2 shows a significant increase in saturation of the BB at excitation powers $>10 \text{ W cm}^{-2}$ after annealing, suggesting that it results in an increased recombination lifetime. This was verified with time resolved PL, as can be seen in figure 3 the decays for the BB emission consist of two components; an initial fast component followed by a slow component that persists to the sub-millisecond time scale. This was consistent with decays reported previously for BB emission in Mg doped wz-GaN⁹. The fast component of the unannealed sample decayed approximately five times faster than after the annealing process; suggesting annealing decreases the concentration of non-radiative defects, in agreement with previous studies on the effect of annealing on non-radiative recombination^{10,11}.

- [1] M. Auf Der Maur, A. Pecchia, G. Penazzi, W. Rodrigues, and A. Di Carlo, *Phys. Rev. Lett.* **116**, 027401 (2016).
- [2] S. Hammersley, M.J. Kappers, F.C.P. Massabuau, S.L. Sahonta, P. Dawson, R.A. Oliver, and C.J. Humphreys, *Phys. Status Solidi C.* **13**, 209 (2016).
- [3] S.-H. Park and S.-L. Chuang, *J. Appl. Phys.* **87**, 353 (2000).
- [4] L.Y. Lee, *Mater. Sci. Tech.* **33**, 1570 (2017).
- [5] D.R. Elsaesser, M.T. Durniak, A.S. Bross, and C. Wetzel, *J. Appl. Phys.* **122**, 115703 (2017).
- [6] S. Nakamura, N. Iwasa, M. Senoh, and T. Mukai, *Jpn. J. Appl. Phys.* **31**, 1258 (1992).

- [7] M.A. Reshchikov, P. Ghimire, and D.O. Demchenko, Phys. Rev. B **97**, 205204 (2018).
- [8] R.E.L. Powell, S. V. Novikov, C.T. Foxon, A. V. Akimov, and A.J. Kent, Phys. Status Solidi C. **11**, 385 (2014).
- [9] M. Godlewski, T. Suski, I. Grzegory, S. Porowski, J.. Bergman, W.. Chen, and B. Monemar, Phys. B Condens. Matter **273-274**, 39 (1999).
- [10] M. Sumiya, K. Fukuda, S. Takashima, S. Ueda, T. Onuma, T. Yamaguchi, T. Honda, and A. Uedono, J. Cryst. Growth **511**, 15 (2019).
- [11] M. Meneghini, D. Zhu, C.J. Humphreys, M. Berti, A. Gasparotto, T. Cesca, A. Vinattieri, F. Bogani, G. Meneghesso, and E. Zanoni, AIP Adv. **5**, 107121 (2015).

Supplementary information

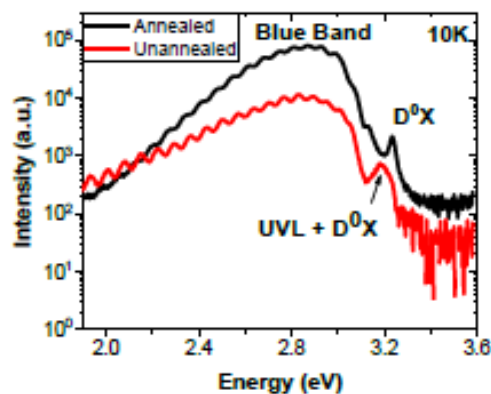


Fig. 1. 10 K PL comparison of Mg doped zb-GaN samples before and after annealing in nitrogen. Samples were excited with the 325 nm line of a HeCd laser with a power density of 5.6 W cm⁻².

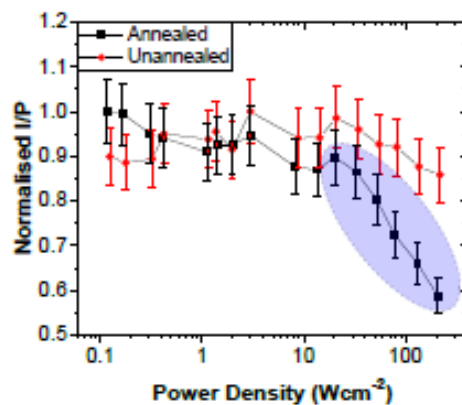


Fig. 2. 10 K integrated BB intensity normalized by excitation density as a function of excitation density for both nitrogen annealed and unannealed samples. Saturation regime of the annealed sample is indicated by the shaded area.

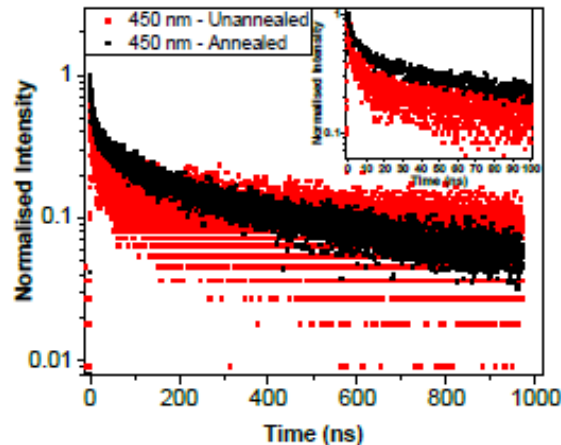


Fig. 3. Decay transients for the annealed and unannealed Mg doped zb-GaN samples taken at 450 nm corresponding roughly to the peak of the blue band emission in both samples. The inset shows the decays over the first 100 ns.

P6 Study of Ti contacts to corundum α -Ga₂O₃

F Massabuau¹, D Nicol¹, F Adams², J Jarman², J Roberts³, A Kovacs⁴, P Chalker³, and R. Oliver²

¹Department of Physics, University of Strathclyde, UK, ²Department of Material Science and Metallurgy, University of Cambridge, UK, ³School of Engineering, University of Liverpool, UK, ⁴Ernst Ruska-Centre for Microscopy and Spectroscopy with Electrons, Forschungszentrum Jülich, Germany

Gallium Oxide (Ga₂O₃) is an emerging wide bandgap semiconductor with applications in solar-blind ultraviolet (UV) sensing, and high-power electronics [1]. This material exists under several phases (α , β , γ , δ , ϵ), with the monoclinic β -phase attracting most attention owing to its thermodynamic stability. In comparison, the rhombohedral α -phase is metastable but displays several advantages compared to the other phases of Ga₂O₃: for example it (i) exhibits the largest bandgap (5.3 eV) amongst all phases, (ii) is isostructural with several other semiconducting group-III or transition metal sesquioxides (e.g. In₂O₃, Ti₂O₃) and (iii) is isostructural with the cheap and widely available sapphire (α -Al₂O₃) substrate.

Metallic contacts play a central role in the working principle and overall properties of semiconductor devices. In β -Ga₂O₃, Ti is routinely used as the metal of choice in order to produce ohmic contacts [1]. However, in this phase the metallic layer has been reported to react with the semiconductor to form a thin TiO_x interlayer [2]. In α -Ga₂O₃, the properties (ohmic/rectifying) and chemical stability of metallic contacts are, at the moment, unexplored. In this study, we investigate the properties of α -Ga₂O₃ films with Ti contacts.

Films of non-intentionally doped α -Ga₂O₃ (thickness 250 nm) were produced by atomic layer deposition, and Ti/Au (20/80 nm) were evaporated and subsequently annealed under N₂ ambient for 2 min at temperatures of 350-600°C. The films were characterised by atomic force microscopy (AFM), X-ray diffraction (XRD), UV light-assisted I-V measurements and high resolution scanning transmission electron microscopy (HR-STEM) with energy dispersive X-ray spectroscopy (EDX).

Topographical and structural analysis from AFM and XRD reveal no observable changes in film structure upon annealing. Figure 1(a) shows the AFM and XRD data of the sample after growth – which remained unchanged upon contact deposition and annealing treatment.

Electrical characterisation of the samples in the dark and under 240 nm and 350 nm light confirm that the structures can be used for solar-blind photodetection. Because the films are undoped and highly resistive, the ohmic or rectifying behaviour was assessed under 240 nm illumination [3]. We note that the films

display ohmic behaviour when the contact were either not annealed (as-deposited) or annealed up to *ca.* 400oC. The greatest (photo)conductivity was obtained for the structure annealed at 400oC. For higher annealing temperature, the device electrical properties degrade rapidly with annealing temperature.

To understand the impact of annealing on the contact structure, HR-STEM and EDX were conducted on the as-deposited device and the sample annealed at 600oC. In the as-deposited sample, the semiconductor and metallic layers can be clearly distinguished (Figure 1(b)). Voids at the Ga₂O₃/Ti interface can be observed in places, which may help explain why the electrical properties can be improved using gentle annealing.

On the other hand, the sample annealed at 600oC exhibits a distinguishably different structure (Figure 1(c)). The Ga₂O₃ film contains several voids, and the Ti film has transformed almost entirely into a TiO_x film. This is a clear evidence of reduction of Ga₂O₃ by Ti. It is interesting to note that the obtained structure is different from that observed in β -Ga₂O₃ [2], which underlines the necessity for a phase-specific study of contacts in Ga₂O₃ devices.

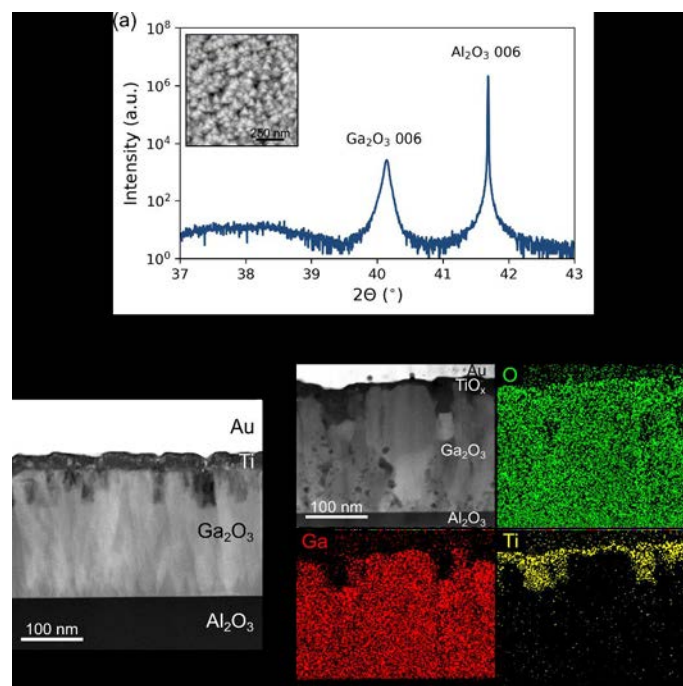


Fig. 1. (a) XRD and AFM (inset) scans of the as-deposited sample demonstrating α -phase Ga₂O₃ films were obtained. STEM and EDX maps of the (b) as-deposited sample, and (c) sample annealed at 600oC.

- [1] Pearton *et al.*, Appl. Phys. Rev. **5**, 011301 (2018)
- [2] Lee *et al.*, APL Mater. **7**, 022524 (2019)
- [3] Liu *et al.*, J. Phys. D: Appl. Phys. **53**, 085105 (2020)

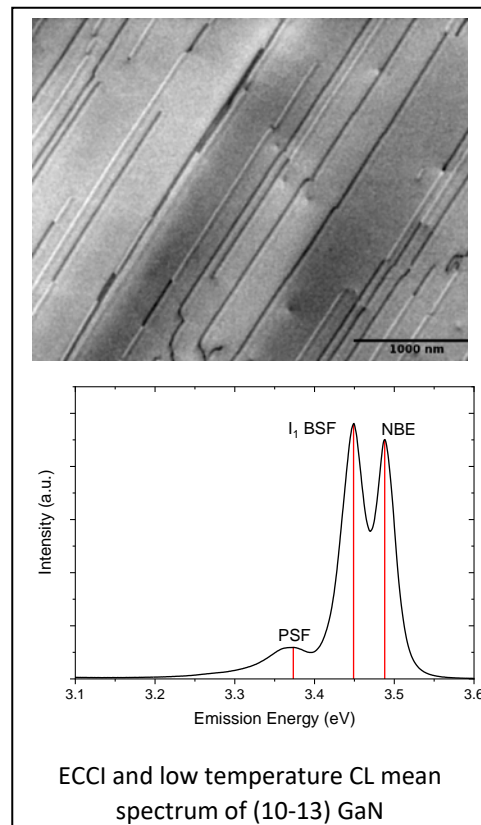
P7 Defects in 10-13 GaN: An electron microscopy study

Gunnar Kusch¹, Elena Pascal², Nan Hu³, Markus Pristovsek³, and Rachel A Oliver¹

¹Department of Materials Science and Metallurgy, University of Cambridge, UK, ²Department of Materials Science and Engineering, Carnegie Mellon University, USA, ³Center for Integrated Research of Future Electronics, Institute for Materials and Systems for Sustainability, Japan

(10-13) GaN is one of the lesser studied but, nevertheless, promising semipolar crystal orientations for the design of optoelectronic devices. While all semipolar structures reduce the piezo and spontaneous polarization fields, only (10-13) offers a negative electric field across an InGaN-GaN quantum well, similar to (0001), which greatly improves hole confinement. Furthermore, the low angle of 32.04° of the (10-13) to the (0001) plane increases the energy needed to form a basal plane stacking faults (BSF), the dominant defect in semipolar heteroepitaxy. While a functioning blue InGaN/GaN LED structure utilizing (10-13) GaN was demonstrated 15 years ago[1], little further research has been published. Both BSFs, and other defects such as dislocations, can have significant impacts on the optical properties of semipolar heterostructures. In this work, we have utilized electron channeling contrast imaging (ECCI) and cathodoluminescence hyperspectral imaging (CL) to analyze the spatial distribution, the type and the optical properties of defects in (10-13) GaN. The sample was grown on m-plane sapphire using directional AlN sputtering and further overgrowth was done by metal-organic vapor phase epitaxy [3]. ECCI is becoming one of the go-to techniques for the analysis of defects in nitride semiconductors, thanks to it being non-destructive, spatially resolved and able to achieve statistically significant results. CL is the ideal correlative technique for ECCI, providing complementary information about the optical properties of the material at or close to the defects.

The majority of defects were I₁ type basal plane stacking faults and bounded partial dislocations, with perfect threading dislocations and prismatic stacking faults also being present. Low temperature (10K) cathodoluminescence hyperspectral imaging revealed light emission associated with I₁ stacking faults and prismatic stacking faults. The stacking fault density in the (10-13) GaN layer was $(3.5 \pm 1.0) \times 10^4 \text{ cm}^{-1}$, and a low threading + partial dislocations density $(7 \pm 2) \times 10^8 \text{ cm}^{-2}$ was also observed. These defect densities are one order of magnitude below densities reported for hetero-epitaxial (11-22) or (11-20) GaN [4], which together with the negative polarization field make (10-13) a very attractive semipolar orientation for long wavelength LEDs.



- [1] Chakraborty A. et al. Jpn. J. Appl. Phys, **44** 30 L945-L947 (2005)
- [2] Naresh-Kumar G. et al. Microscopy and Microanalysis, 20(1), 55-60 (2014)
- [3] N. Hu et al. J. Crystal Growth 507, 205-208 (2019)
- [4] M. Pristovsek et al. Phys. Status Solidi (B) 253, 61-66 (2016).

P8 Multi-microscopy of a single dislocation cluster within a GaN-on-GaN p-i-n diodes

Simon M. Fairclough¹, Bogdan-Florin Spiridon¹, Florian Tendille², Fabien Massabuau¹, Gunnar Kusch¹, Thi Huong Ngo³, Rémi Comyn³, Eric Frayssinet³, Kaddour Lekhal², Sébastien Chenot³, Benjamin Damilano², Vincent Gelly², Yvon Cordier³, and Rachel A Oliver¹

¹Department of Material Science and Metallurgy, University of Cambridge, UK, ²Saint Gobain Lumilog, France, ³Université Côte d'Azur, France

Gallium nitride (GaN) has shown great application within the transistor field due to a high breakdown voltage, high mobility and high saturation velocity.¹ The performance of these devices can be reduced by the impact of strain arising from the lattice and thermal mismatch of GaN with the substrate (eg Sapphire, Silicon or Silicon Carbide) which leads to high defect densities (e.g. threading dislocations density from 10^8 to 10^{10}cm^{-2}) and cracking if strain management is not handled correctly.²

Recently, GaN devices have been developed on free-standing GaN substrates which have been made via hydride vapor phase epitaxy (HVPE).³ Free-standing GaN potentially offers an ideal substrate for high performance devices owing to the matching lattice parameter and thermal expansion coefficient. Indeed, the dislocation density within HVPE-grown free standing GaN often falls to levels of the order of 10^7cm^{-2} .³ However, clusters of dislocations are frequently observed and may impact device properties. The formation mechanisms of such clusters and their detailed influence on device performance is an under-researched area.

Multi-microscopy techniques have been used to great effect to understand a multitude of defects in GaN.⁴ As shown in Figure 1, here we investigate the properties of a single dislocation cluster in a p-i-n diode structure utilising atomic force microscopy (AFM), tunnelling AFM (TUNA) and cathodoluminescence scanning electron microscopy (CL). We then investigate the structure via cross-sectional transmission electron microscopy (TEM) in an effort to help determine the influence of the dislocation cluster on the diode properties.

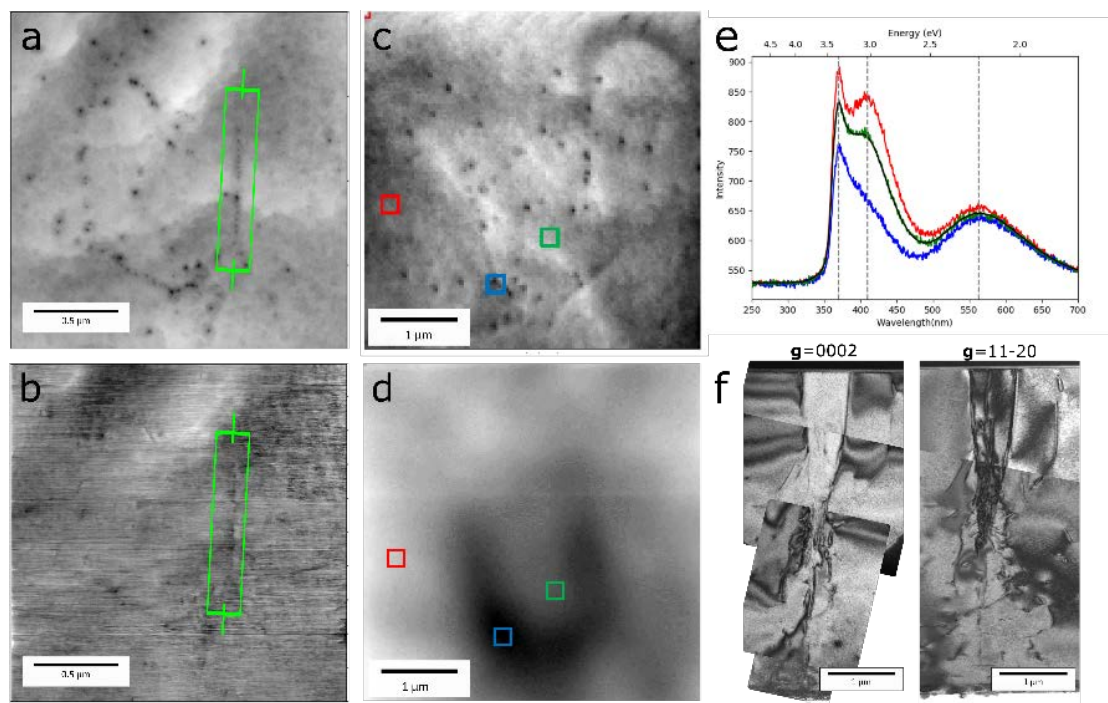


Fig. 3. Multi-microscopy of a single dislocation cluster with a GaN-on-GaN p-i-n diode as imaged by a) Peak Force Tapping® AFM, b) TUNA c) Secondary electron imaging, d) Panchromatic CL, e) the corresponding CL spectra for the red, green and blue regions in c & d, f) **g.B** TEM analysis of a cross section of the dislocation cluster.

- [1] Roccaforte, F., Fiorenza, P., Nigro, R. Lo, Giannazzo, F. & Greco, G. Physics and technology of gallium nitride materials for power electronics. *Rivista del Nuovo Cimento* vol. 41 625–681 (2018).
- [2] Bennett, S. E. Dislocations and their reduction in GaN. *Materials Science and Technology* vol. 26 1017–1028 (2010).
- [3] Ngo, T. H. *et al.* Cathodoluminescence and electrical study of vertical GaN-on-GaN Schottky diodes with dislocation clusters. *J. Cryst. Growth* **552**, 125911 (2020).
- [4] Mancini, L. *et al.* Multi-microscopy study of the influence of stacking faults and three-dimensional In distribution on the optical properties of m-plane InGaN quantum wells grown on microwire sidewalls. *Appl. Phys. Lett.* **108**, (2016).

P9 Combined Time of Flight and Photometric Stereo Imaging for Surface Reconstruction

Emma Le Francois¹, Johannes Herrnsdorf¹, Jonathan J. D. McKendry¹, Laurence Broadbent², Martin D. Dawson¹, and Michael J. Strain¹

¹Institute of Photonics, University of Strathclyde, UK, ²Aralia Systems, Bristol Robotics Laboratory, Bristol, UK

3D reconstruction of objects can be achieved using both time of flight and photometric stereo imaging using four modulated white LEDs, a SPAD camera and a mobile phone. The standard deviation for the reconstruction is 1.5 mm at a distance of 70 cm.

Keywords— Time of Flight, Photometric Stereo, 3D surface reconstruction, LEDs, SPAD camera, Mobile device

Introduction

Time-of-flight (ToF) and photometric stereo (PS) are three-dimensional (3D) imaging techniques with distinct, and complementary, areas of application. ToF imaging deals well with long range and discontinuous imaging but is limited by the resolution of current single photon camera systems or acquisition time of scanning systems. PS imaging uses conventional imagers and therefore has high spatial resolution but does not deal well with discontinuous surfaces. ToF is typically used for long-range light detection and ranging systems. A short-pulsed laser illuminates a scene in order to time correlate the reflected light intensity with the outgoing pulse to obtain a range map of the scene [1] and is commonly used in automotive and robotics applications. Alternatively, PS imaging is a passive method that relies on having one fixed camera perspective and different illumination directions to image an object in 3D [2]. This technique is more common in indoors scenarios for video surveillance, surface mapping and robot navigation [3]. Our previous work on “top-down” illumination PS imaging demonstrated 3D reconstruction with an error ranging from 3.5% to 10.4% for an object imaged at a distance of 42 cm [4]. However, this method used a black background to easily mask objects to reconstruct in order to speed up the computational reconstruction time. By employing a dual imaging system incorporating both ToF and PS the complementary properties of both systems can be used to image complex 3D fields with high resolution and complex discontinuities between objects.

Here we report the 3D reconstruction of three different objects (a sphere, a monkey head and a cube) using ToF - as a tool to mask the objects, and PS imaging for a high-resolution surface reconstruction. A time-correlated single photon-counting (TCSPC) single photon avalanche diode (SPAD) camera is used with blue commercial light-emitting diodes (LEDs) to obtain a range map of the scene. For PS imaging, four white modulated LEDs illuminate the object while a mobile phone capture frames at 960 frames per second (fps). The LEDs are modulated at the camera frame rate with an orthogonal multiple access carrier schemes such that visible flicker is minimal, and no electronic synchronization is needed between the LEDs and the phone [4,5]. Our early results of the surface reconstruction show a root mean square error (RMSE) of 3.1%.

Experiment

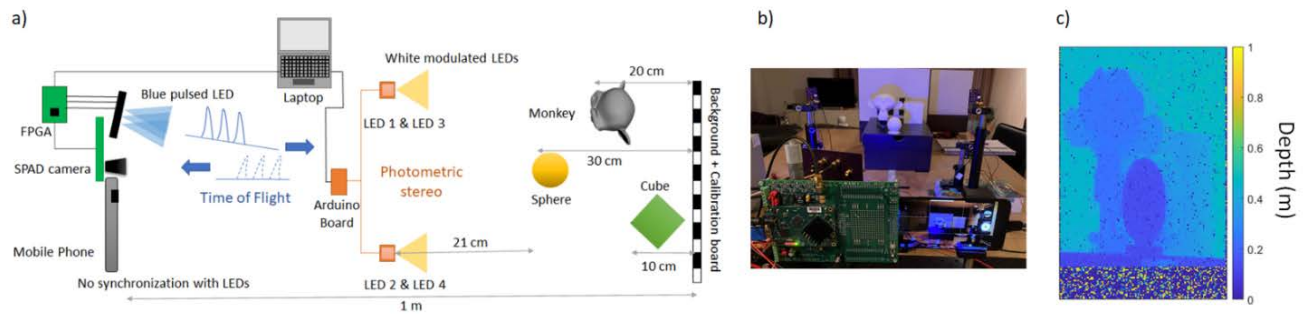


Fig. 1. a) Top-down schematic of the experimental setup, b) Picture of the experimental setup, c) Range Map of the scene using TCSPC mode with the SPAD camera

The experimental setup with both ToF and PS imaging is shown in Fig. 1.a) and b). For ToF imaging, a SPAD image sensor is used and consists of a 192x128 SPAD pixels [5]. Each pixel is 18.4 x 9.2 μm^2 in area and can be operated with TCSPC functionality, see [5,6] for more details. Both photon counting (PC) and TCSPC modes are needed for the calibration. PC mode is used to acquire the image intensity of a calibration board and the TCSPC mode for ToF, where time signal is provided by blue commercial LED array that is pulsed – 11.3 ns pulse wide at a repetition rate of 30 ns – with respect to a trigger signal from the SPAD camera. Both LED array and SPAD camera are controlled with field-programmable gate array (FPGA) modules. For PS imaging, four white commercial LEDs were placed 21 cm away from the object in a X shape. A mobile phone device (Samsung Galaxy 9) was mounted on a tripod as close as possible to the SPAD camera at a distance of 70 cm from the object with a field of view of 32 degrees. The phone captured frames with a resolution of 1280 x 720 at a rate of 960 frames per second (fps) for 0.2 s. For the illumination, we used an USB programmable controller board (Arduino Uno) to modulate the four LEDs at a frequency of 960 Hz. Each LED was modulated with an individual multiple access carrier signal at a frequency of 960 Hz, which is above visual flicker recognition and therefore suitable for digital lighting applications. The carriers were designed such that, analogous to orthogonal frequency division multiple access, no synchronization between the LEDs and the mobile phone was required [4,5].

The SPAD intensity image was scaled and spatially registered to match the smartphone image dimensions using a checkerboard calibration object in the image. Then, a range map (Fig. 1.c)) obtained with the TCSPC mode is used to isolate each object by selecting its distance range. The subsequent PS imaging process carried out on the selected area follows the method from [4].

Results

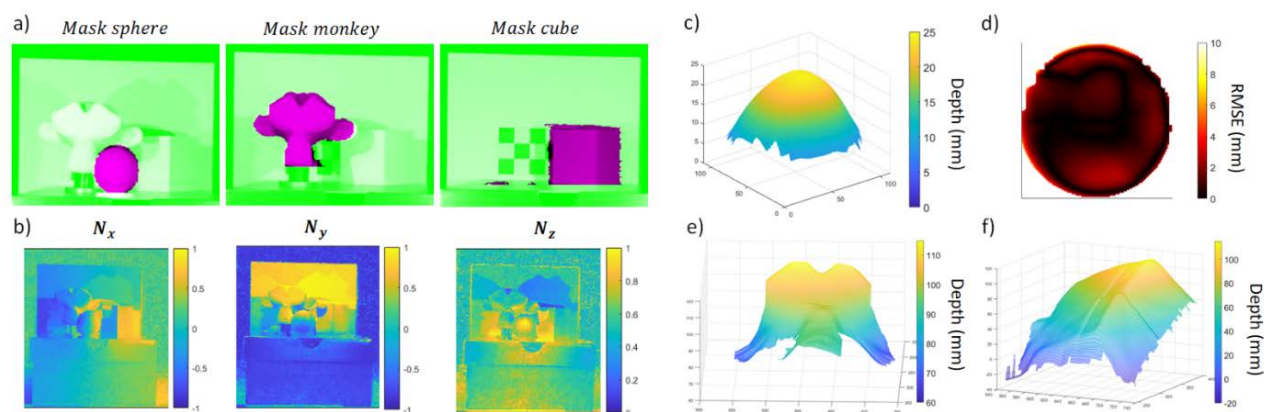


Fig. 2. a) ToF masks from SPAD camera superimpose on scene image, b) Surface normal components of the scene, c) 3D reconstruction of sphere, d) RMSE map of the sphere, e) 3D reconstruction of the monkey

head, f) 3D reconstruction of the cube corner. Fig. 2. a) shows the three ToF masks which are individually superimposed on the mobile phone image. We can see both cameras are correctly calibrated and aligned as the ToF masks coincide with the smartphone image for the three objects. Fig. 2.b) plots the surface normal components N_x , N_y and N_z of the scene. N_x and N_y correctly distinguishes left, right and up, down facing surfaces, respectively. As we cannot see the back of the scene, N_z is always positive with some variations due to the scene's depth. N_x , N_y and N_z are used to calculate the surface topology of the three objects. Fig.2.c) plots the reconstruction of the sphere and we can see that a high-resolution is achieved. Its corresponded root-mean squared error map [4] (Fig.2.d)) indicates a reconstruction error varying from 0 mm to 4 mm, which produces a global RMSE of 1.5 mm and represents a normalized error of 3.1%. This error is below our previous results [4,7] though the mobile phone is located at almost twice the distance in this setup. Fig.2.e) and f) respectively plot the 3D reconstruction of the monkey head and the cube. Both reconstructions display lower-resolution reconstruction than for the sphere, however these are early results and are encouraging as the shape of both objects has been successfully reconstructed.

Conclusion

Accurate calibration of a SPAD camera with a mobile phone has been demonstrated which gives the possibility to use ToF to improve our previous PS imaging technique. By using both ToF and PS imaging, we could simultaneously obtain depth information of a public area for example with a high-resolution 3D reconstruction of selected elements within the imaged scene.

Acknowledgements

We acknowledge support from the EPSRC (EP/M01326X/1, EP/T00097X/1). Emma Le Francois's studentship was part supported by Fraunhofer UK. We would also like to thank David Li for lending us the SPAD camera.

References

- [1] M. Edgar, S. Johnson, D. Phillips, and M. Padgett, "Real-time computational photon-counting LiDAR," *Optical Engineering*, vol. 57, no. 03, p. 1, 2017.
- [2] R. J. Woodham, "Photometric Method For Determining Surface Orientation From Multiple Images," *Optical Engineering*, vol. 19, no. 1, pp. 139-144, 1980.
- [3] A. Lipnickas and A. Kny, "A stereovision system for 3-d perception," *Elektronika ir Elektrotechnika*, no. 3, pp. 99-102, 2009.
- [4] E. L. Francois, J. Herrnsdorf, L. Broadbent, M. D. Dawson, and M. J. Strain, "Top-down illumination photometric stereo imaging using lightemitting diodes and a mobile device," in *Frontiers in Optics + Laser Science APS/DLS*, p. JTU3A.106, Optical Society of America, 2019.
- [5] R. K. Henderson *et al.*, "A 192×128 Time Correlated SPAD Image Sensor in 40-nm CMOS Technology," *IEEE J. Solid-State Circuits*, vol. PP, pp. 1-10, 2019, doi: 10.1109/JSSC.2019.2905163.
- [6] A. D. Griffiths *et al.*, "Multispectral time-of-flight imaging using light-emitting diodes," vol. 27, no. 24, pp. 35485-35498, 2019.
- [7] E. Le Francois, J. Herrnsdorf, J. J. D. McKendry, L. Broadbent, M. D. Dawson and M. J. Strain, "Combined Time of Flight and Photometric Stereo Imaging for Surface Reconstruction," 2020 IEEE Photonics Conference (IPC), Vancouver, BC, Canada, 2020, pp. 1-2 , doi: 10.1109/IPC47351.2020.9252553.

P10 Structural impact of step-graded AlGaIn buffer variants on MOCVD grown GaN-on-Si

Saptarsi Ghosh¹, Alexander Hinz¹, Menno J Kappers¹, Martin Frentrup¹, Saiful Alam², Bogdan F Spiridon¹, Rachel A Oliver¹, David J Wallis^{1,2}

¹Department of Materials Science and Metallurgy, University of Cambridge, UK, ²Centre for High Frequency Engineering, University of Cardiff, UK, ⁵The Parade, UK

GaN heterostructures grown on Si(111) offer all the advantages of III-nitride semiconductors on a cost-effective, mature, and scalable platform^{1,2}. However, in addition to the large lattice mismatch, an even larger thermal expansion co-efficient mismatch between the substrate and the epilayer often results in formation of cracks or large tensile bow, ruining device processing and functionality. The last two decades has seen the III-nitride community engineer several methods that produce compressive strain in the GaN epilayers during growth to compensate for the tensile strain upon cooldown, namely low-temperature AlN interlayers, Al_xGa_{1-x}N-Al_yGa_{1-y}N superlattices, and graded AlGaIn buffers³. Among these, the step-graded variant of the latter where the buffer layer consists of several AlGaIn layers with distinct compositions (Fig. 1a) is widely used and often the ‘recommended’ approach⁴. However, in this multi-dimensional parameter space (such as number of layers, individual layer thickness, and individual layer compositions) different groups often come to their own “optimised” solution.

In this presentation, we scrutinize a series of such step-graded structures on 6-inch Si with different designs of the stack and inspect the effect on a 1-micron GaN layer grown on top through a framework of non-destructive characterisation. We demonstrate that even though all the heterostructures are compressively bowed with less than 50 µm bow across the entire wafer, the evolution of strain during growth, the surface morphology, and the defect-structures of the GaN layer are systematically dependent on the grading parameters. During the MOCVD growth itself, we monitor the change of curvature in real-time to estimate the strain evolution during growth of each layer (Fig. 1b). Post-growth, Nomarski optical microscopy, atomic force microscopy (AFM), and high-resolution XRD (HRXRD) are implemented to estimate the long-range roughness, topography, and microstructure, respectively (Fig 1c-d). The results should not only aid design of such step-graded buffers but may also assist in guiding the compositional grading of ‘linearly-graded’ structures⁵.

- [1] Amano, H. *et al.* The 2018 GaN power electronics roadmap. *J. Phys. D: Appl. Phys.* **51**, 163001 (2018).
- [2] Zhu, D., Wallis, D. J. & Humphreys, C. J. Prospects of III-nitride optoelectronics grown on Si. *Reports Prog. Phys.* **76**, 106501 (2013).
- [3] Dadgar, A. Sixteen years GaN on Si. *Phys. status solidi* **252**, 1063–1068 (2015).
- [4] Mohan, N., Manikant, Soman, R. & Raghavan, S. Integrating AlGaIn/GaN high electron mobility transistor with Si: A comparative study of integration schemes. *J. Appl. Phys.* **118**, 135302 (2015).
- [5] Yang, Y. *et al.* Effect of compositionally graded AlGaIn buffer layer grown by different functions of trimethylaluminum flow rates on the properties of GaN on Si (111) substrates. *J. Cryst. Growth* **376**, 23–27 (2013).

Convex

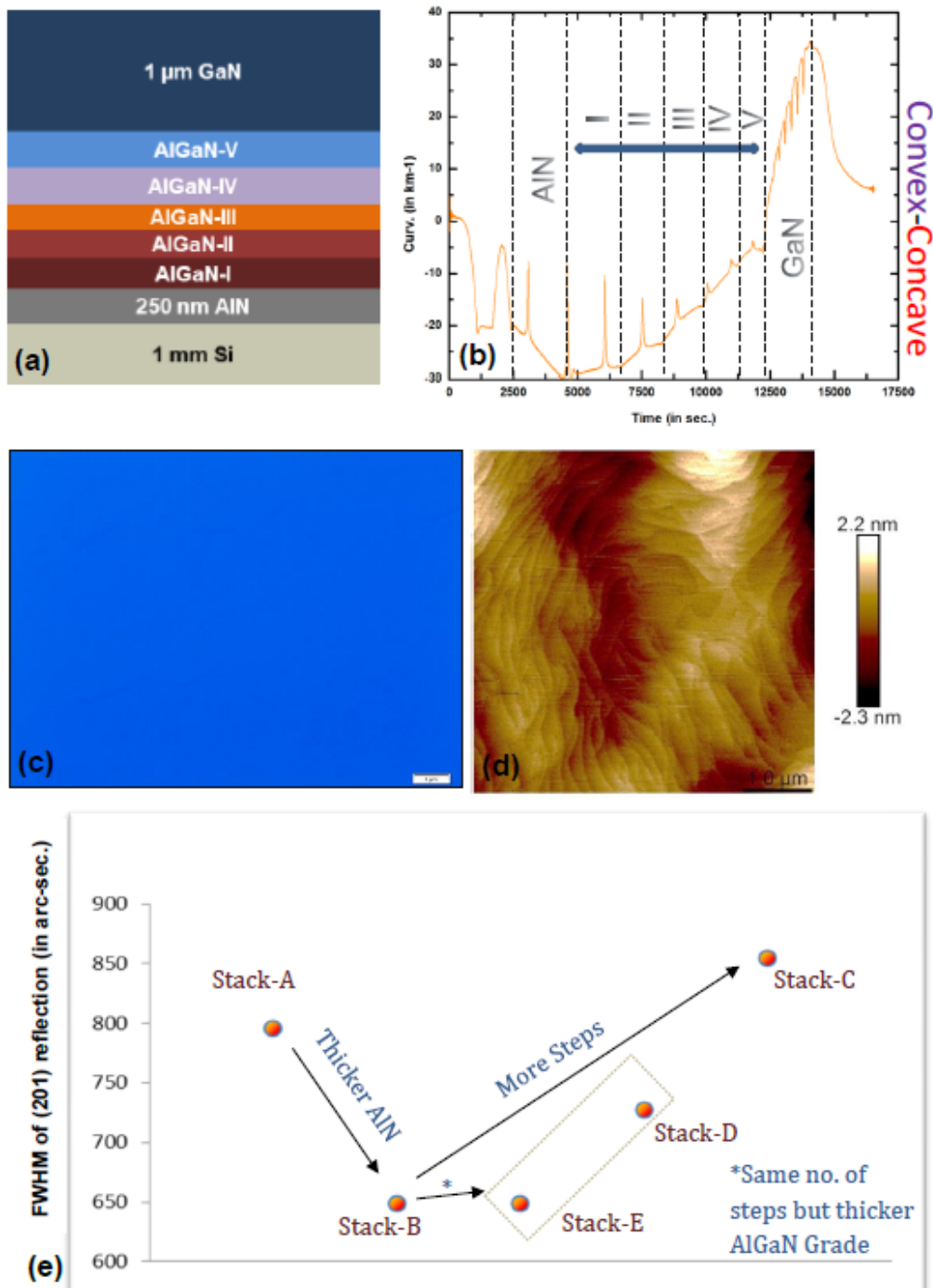


Fig. 1. (a) An exemplary schematic of the step-graded structure where the buffer is composed of five different compositions of AlGaN. (b) The evolution of in-situ curvature shows the real-time stress changes during the growth of the nucleation layer, the graded-buffer, and the top GaN layer. Note that the sudden peaks are data artefacts. (c) Optical Nomarski micrograph (scale-bar 5 μm) acquired near the edge of the wafer shows a crack-free smooth morphology of the GaN surface and (d) AFM scan of the surface evaluates a rms roughness of 0.6 nm of the same. (e) HRXRD analysis make it evident that structural attributes such as the mosaic twist and/or the dislocations with edge-components in the GaN layer is intricately dependent upon the individual layer thicknesses and different design of the grade.

P11 The role of the nucleation step in self-assembled GaN nanowire growth

Nian Jiang¹, Saptarsi Ghosh², Rachel A Oliver², and Hannah J Joyce¹

¹Department of Engineering, University of Cambridge, UK, ²Cambridge Centre of Gallium Nitride, University of Cambridge, UK

Nucleation of self-assembled GaN nanowires grown by metal organic chemical vapour deposition was investigated. It is shown that a growth interruption between nucleation and nanowire growth affects the nanowire density and growth rate.

Introduction

Self-assembled nitride nanowire growth via metal organic chemical vapour deposition (MOCVD) is considered to be an optimal method to obtain nitride nanowires because it is catalyst-free and easy to scale-up. Nitride nanowires have attracted tremendous academic and industrial interest as they offer a promising solution to the problems facing heteroepitaxial III-nitrides associated with lattice mismatch and thermal mismatch.

The self-assembly method has been adopted by multiple groups since its first demonstration.¹⁻³ This method requires neither foreign catalysts (which introduce the risk of contamination to the material and reactors), nor dielectric masks which are expensive and challenging to scale-up. However, a lack of understanding of self-assembled growth mechanisms has prevented this method from reaching its full potential.

Self-assembled growth typically involves a nitridation treatment for the sapphire substrates and a short nucleation step before nanowire growth. SiH₄ is often introduced during the growth to increase the growth rate along c-direction.⁴ While the nitridation treatment has been widely discussed as a result of its wide application in planar structure growth,⁵⁻⁷ little has been reported for the nucleation step despite its significant impact on the dimension and crystal quality of the subsequent nanowires grown.¹ In this study, we investigated the impact of nucleation conditions on self-assembled GaN nanowire growth.

Experiment

Self-assembled GaN nanowires were grown on c-sapphire substrates in a Veeco Propel Power GaN MOCVD, using ammonia (NH₃), trimethylgallium (TMGa) and silane (SiH₄) as precursors. The substrates were kept in H₂ flow at 1060 °C for 5 min to decontaminate the surface, followed by a 10 min nitridation at 1080 °C. The temperature was then dropped to 1035 °C for GaN nanowire growth. Growth was initiated with a nucleation step with [NH₃]/[TMGa] = 12, followed by a 15s growth interruption before 10 min nanowire growth with [NH₃]/[TMGa] = 6 and [SiH₄] = 800 nmol/min. To study the nucleation impact, a set of samples was grown with 0s, 2s and 5s nucleation times. A comparison sample was prepared without the 15s growth interruption between the 5s nucleation and nanowire growth. Optical reflectivity of the substrate was monitored during the growth.

Results and discussion

The typical morphologies of samples grown with 0s, 2s and 5s nucleation time are compared in Figure 1 (a-c). The differences between samples without (a) and with (b-c) the nucleation step are significant. Sparse GaN micro-rods (with aspect ratio ~ 1) are observed for the growth without the nucleation step. Nanowire growth was significantly enhanced by the nucleation step. GaN nanowires with 2s and 5s nucleation have an average of length of (4.5 ± 1.0) μm and (5.7 ± 0.8) μm and diameter of (1.0 ± 0.1) μm and (1.0 ± 0.1) μm, respectively. The samples exhibit similar nanowire densities and overall morphology, regardless of the duration of the nucleation step. Figure 1(d) shows the nanowires grown without the 15s interruption between nucleation and growth. The resulting GaN nanowires have an average of length of (4.6 ± 1.2) μm with an average diameter of (1.5 ± 0.2) μm. In addition to the diameter difference, the density of the GaN

nanowires without the growth interruption between nucleation and growth is much lower than that with the 15s interruption.

In conclusion, we have demonstrated that the initial nucleation step plays an important role in achieving GaN nanowires with large aspect ratio. The diameter of GaN nanowires is found to be independent of the duration of the nucleation step, but is affected by the duration of the interruption between the nucleation step and the rest of the growth. We suggest this interruption is associated with evaporation/surface reconstruction, which is supported by in-situ reflectivity measured during the growth. This process reduces the size of GaN nuclei and may further reduce the defects caused by the lattice mismatch between the sapphire substrate and GaN grown on it.

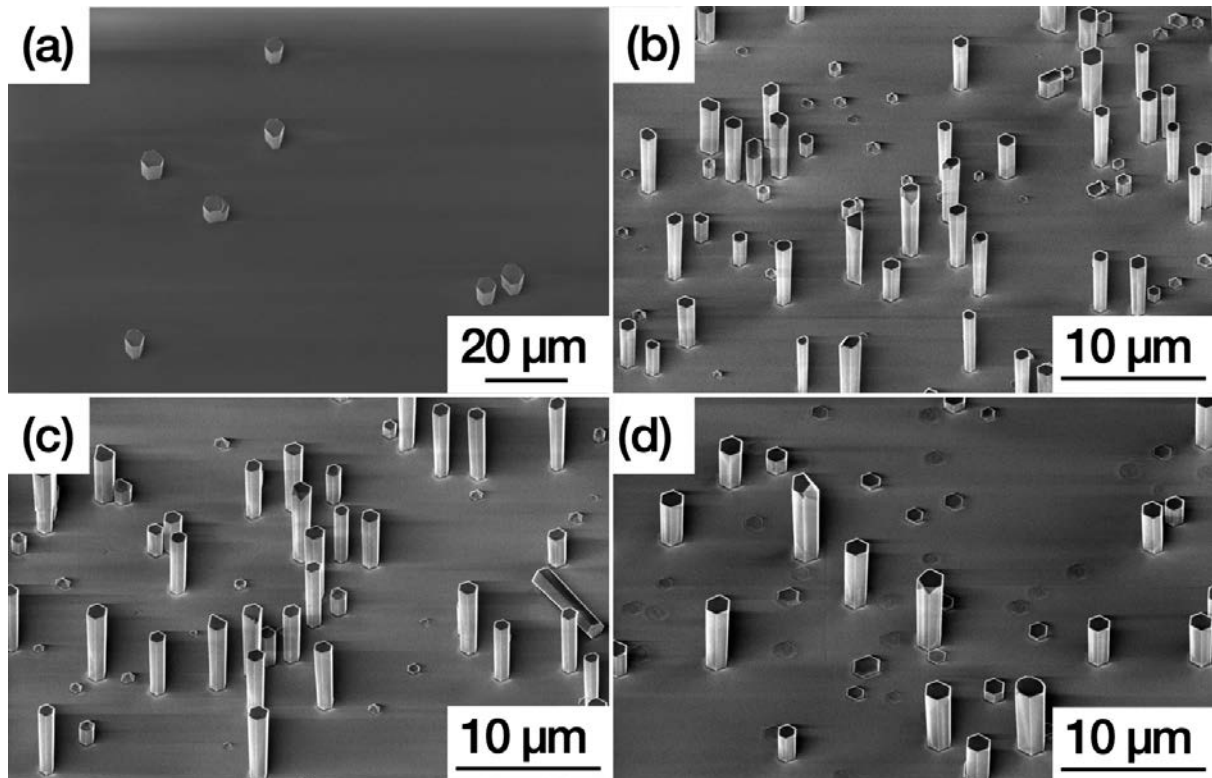


Fig. 1. SEM images of GaN grown with (a) 0s, (b) 2s and (c) 5s nucleation step followed by a 15s break before nanowire growth. (d) GaN Nanowire grown with 5s nucleation step without the 15s break before nanowire growth.

- [1] R. Koester, J.S. Hwang, C. Durand, D. Le Si Dang, and J. Eymery, *Nanotechnology* **21**, (2010).
- [2] B. Zhao, M.N. Lockrey, P. Caroff, N. Wang, L. Li, J. Wong-Leung, H.H. Tan, and C. Jagadish, *Nanoscale* **10**, 11205 (2018).
- [3] C. Tessarek and S. Christiansen, *Phys. Status Solidi Curr. Top. Solid State Phys.* **9**, 596 (2012).
- [4] C. Tessarek, M. Heilmann, E. Butzen, A. Haab, H. Hardtdegen, C. Dieker, E. Spiecker, and S. Christiansen, *Cryst. Growth Des.* **14**, 1486 (2014).
- [5] S. Mohn, N. Stolyarchuk, T. Markurt, R. Kirste, M.P. Hoffmann, R. Collazo, A. Courville, R. Di Felice, Z. Sitar, P. Vennéguès, and M. Albrecht, *Phys. Rev. Appl.* **5**, 1 (2016).
- [6] F. Liu, R. Collazo, S. Mita, Z. Sitar, G. Duscher, and S.J. Pennycook, *Appl. Phys. Lett.* **91**, 3 (2007).
- [7] F. Dwikusuma and T.F. Kuech, *J. Appl. Phys.* **94**, 5656 (2003).

P12 Tomography of Porous Gallium Nitride Nanostructures

Maruf Sarkar¹, Peter Griffin¹, Richard Langford², and Rachel A Oliver¹

¹Department of Materials Science and Metallurgy, University of Cambridge, UK, ²Department of Physics, University of Cambridge, UK

The Cambridge Centre for Gallium Nitride is developing a range of III-Nitride devices that exhibit a complex 3D structure. To this end, the overall aim of this research project is to develop and apply tomographic microscopy techniques that allow for the three-dimensional characterization of nanostructured semiconductor samples. Structural insights will be incorporated into models to understand what structural factors enhance or limit the performance of devices and to drive the future development of improved fabrication techniques or novel device designs.

Porosification of semiconductors provides an alternative method for the engineering of materials[1]. In III-nitrides such as GaN, this can be achieved using doping selective electrochemical etching which creates porosity in doped layers while leaving undoped layers largely unchanged. This material decomposition allows for the fabrication of surface and subsurface pores. Electrochemically etched porous GaN semiconductors offer a vast multitude of properties that can be exploited for novel and enhanced device characteristics which could facilitate the next generation of optoelectronics. However, determining their internal structure such as pore morphology – which is essential for the non-compositional engineering and optimisation of devices – is non-trivial and requires three-dimensional tomographic imaging.

A key example of a porous GaN device application are Distributed Bragg Reflectors (DBR)[2]. A porous DBR structure can be made by growing GaN consisting of alternating layers of undoped GaN and n-doped GaN, the latter of which is porosified when using the doping selective electrochemical etching. Porous DBRs are of interest as they a route towards highly reflective and lattice-matched DBRs which could be used in microcavity-based GaN lasers and LEDs. The porous DBRs investigated were produced using two etching methods[3]. A one-step vertical etching method making use of dislocations as an etching pathway to allow the etchant to access n-doped GaN. This produces pores that form radially branching networks emanating out of the dislocations. A two-step lateral etching method makes use of patterning to define deep trenches that expose the sidewalls of the n-doped GaN. This produces pores that are highly aligned with the etching direction.

In this study, electron tomography via Focused Ion Beam – Scanning Electron Microscopy (FIB-SEM) slice and view imaging was investigated. This technique allows one to map the 3D inner structure of an object through the acquisition of a series of 2D sections. Through FIB serial sectioning, 2D SEM imaging, and 3D image reconstruction, this technique was able to produce high fidelity 3D models of porous GaN DBRs that were able to reproduce the expected pore morphology produced by the two etching methods. Less successful 3D reconstructions were plagued by numerous artefacts such as curtaining, sample charging, poor image registration, and low signal-to-noise; each is a point for future optimization. These artefacts contributed to a compromised machine learning-based segmentation of the porous regions from the host matrix. In the segmentation process, one seeks to both preserve and isolate the porous morphology observed prior to segmentation. However, regions much larger than the pores themselves were incorrectly classified as porous. This is thought to be attributed to charging effects which took the form of bright, high contrast regions around individual and groups of pores, that are unrelated to the material topology.

- [1] P. H. Griffin et al., “Porous nitride semiconductors reviewed,” *Journal of Physics D: Applied Physics*, 2020.
- [2] P. H. Griffin et al., “The relationship between the three-dimensional structure of porous GaN distributed Bragg reflectors and their birefringence,” *Journal of Applied Physics*, 2020.

- [3] T. Zhu et al., "Wafer-scale fabrication of non-polar mesoporous GaN distributed Bragg reflectors via electrochemical porosification," Scientific Reports, 2017.

P13 Thick GaN capped AlGa_{0.25}/Ga_{0.75}N HEMTs for reduced surface effects

Maira Elksne, Abdullah Al-Khalidi, and Edward Wasige

University of Glasgow, UK

In this paper an unpassivated AlGa_{0.25}/Ga_{0.75}N HEMT with 70nm thick undoped GaN cap layer for reduced surface effects is presented. Devices with sizes of 2x200 μm show gate leakage currents of 3 μA at -20 V with threshold voltage of -5.3 V. These devices exhibit off-state breakdown voltage over 200 V.

AlGa_{0.25}/Ga_{0.75}N high electron mobility transistors (HEMTs) have a great potential for high-power and high-frequency applications due to the combination of high breakdown field, high sheet charge density and high electron velocity. However one of the limitations of the today's technology is the DC-to-RF dispersion or current collapse, especially at millimetre-waves where the use of field plates is not possible. The common approach to reduce dc-to-RF dispersion is by using SiN_x passivation, but the reproducibility of gate leakage, breakdown voltages and effectiveness of dispersion removal is unreliable [1]. In this paper a new approach of using 70nm thick undoped GaN cap is investigated.

AlGa_{0.25}/Ga_{0.75}N HEMTs with deeply recessed contacts were fabricated on a high thermal conductivity 4H-SiC substrate grown by molecular beam epitaxy (MBE). The epitaxial structure used here are illustrated in Figure 1(left). Fabricated unpassivated devices show improved dispersion which is attributed to reduced impact of surface states. Pulsed IV measurements we performed at 5 different bias points and compared to DC-IV characteristics and showed in Figure 1(right). Bias voltage of [0,0] or cold point show self-heating effects within the device. Gate lag and drain lag measurements at bias voltages of [-7V,0], [-7V,10V],[-7V,20V],[-7,25V] were performed, where current collapse is observed however it is not a complete collapse under stress comparing it to a standard unpassivated GaN HEMT structure. This demonstrates that this method with some optimisation could be an alternative way to conventional passivation. Here post gate etch annealing is a crucial fabrication step that improved the gate leakage currents from 2.18×10^{-4} down to 3.74×10^{-6} (A/mm) and also shifted the threshold voltage V_{TH} from -4.6 V to -5.3 V. Here breakdown voltages over 200 V and reduced impact of surface states are achieved using an unpassivated AlGa_{0.25}/Ga_{0.75}N HEMTs with an undoped 70nm thick GaN cap layer for a 2μm gate length devices.

Acknowledgments :The authors would like to thank the staff of James Watt Nanofabrication Centre (JWNC) and Dr. Farid Medjdoub and Mr. Riad Kabouche for performing the pulsed IV measurements.

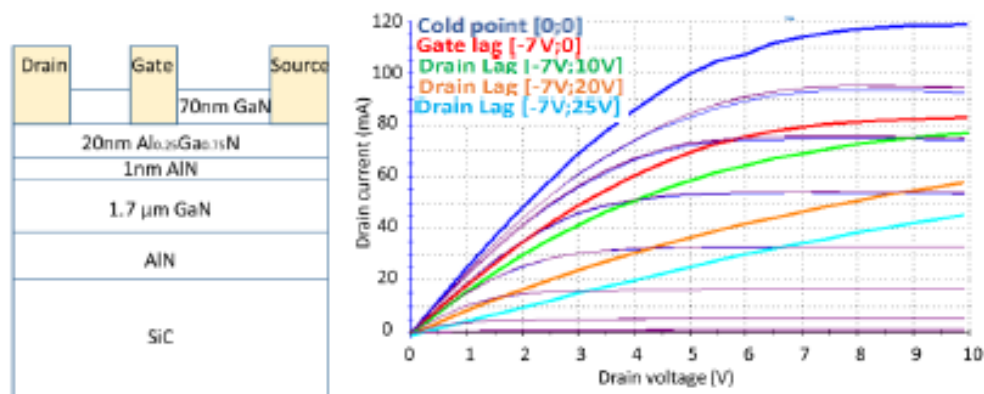


Fig. 1. Epitaxial layer structure of the wafer(left) and measured DC-IV and pulsed IV characteristics(right).

References

- [1] T. Huang, J. Bergsten, M. Thorsell, and N. Rorsman, "Small- and Large-Signal Analyses of Different Low-Pressure-Chemical-Vapor-Deposition SiN_x Passivations for Microwave GaN HEMTs," vol. 65, no. 3, pp. 908–914, 2018.

P14 Investigation of electrically active defects in In_{0.15}Ga_{0.35}N/GaN multi quantum wells grown on different substrates by using deep level transient spectroscopy

Abdulaziz Almalki^{1,2}, Saud Alotaibi¹, Maryam Al huwayz¹, Amjad Almuniyif¹, Sultan Alhassan¹, Shan Lin³, Lixia Zhao^{3,4}, Mohamed Henini¹

¹School of Physics and Astronomy, University of Nottingham, UK, ²Physics department, Taibah University, Saudi Arabia, ³State Key Laboratory of Integrated Optoelectronics, Institute of Semiconductors, Chinese Academy of Sciences, China, ⁴Center of Materials Science and Optoelectronic Engineering, University of Chinese Academy of Sciences, China

InGaN/GaN semiconductor structures are promising for many applications, such as light emitting diode (LEDs), multijunction solar cells, and more recently, tunnel field effect transistors (TFETs). However, to realize their full potential, it is important to understand the impact of defects on device performance. Deep-level transient spectroscopy (DLTS) is employed in this study to investigate the electrically defects in In_{0.15}Ga_{0.35}N (2.5 nm) /GaN (10.7nm) multi quantum wells grown on both GaN and sapphire substrates. Capacitance-voltage (C-V), current-voltage (I-V), and DLTS measurements were performed at different temperatures. Both samples showed good I-V characteristics. Furthermore, the C-V measurements for sample grown on GaN substrate showed two different regions from $V_r = -4$ V to $V_r = 0$ V at room temperature, resulting in two different free electron concentration values. However, for the sample grown on sapphire substrate only one free electron concentration was obtained, meaning that the doping concentration is more uniform in the structure grown on sapphire than the one grown on GaN. For DLTS measurements under $V_r = -0.5$ V, only one trap level in both samples with same activation energy of 0.01 eV was detected. This shallow electron trap has similar signature to that reported in InGaN/GaN by Venturi et al [1]. It is suggested that the trap observed by Wen et al [2] is related to lower Indium content. The trap concentrations were also determined to be $\approx 3.9 \times 10^{15}$ cm⁻³ and 2.6×10^{16} cm⁻³ in GaN and sapphire substrate, respectively. These findings are important as they allow us to better understand the defects in InGaN/GaN quantum wells grown on different substrates and to further improve the performance of InGaN/GaN based devices.

- [1] G. Venturi, A. Castaldini, A. Cavallini, M. Meneghini, E. Zanoni, D. Zhu, C. Humphreys, Dislocation-related trap levels in nitride-based light emitting diodes, Appl. Phys. Lett. (2014). <https://doi.org/10.1063/1.4879644>.
- [2] P. Wen, S. Zhang, J. Liu, D. Li, L. Zhang, Q. Sun, A. Tian, K. Zhou, T. Zhou, H. Yang, Investigation of InGaN/GaN laser degradation based on luminescence properties, J. Appl. Phys. 119 (2016) 213107. <https://doi.org/10.1063/1.4953236>.

P15 A study of the effect of a Si-doped underlayer on photoluminescence in InGaN/GaN QWs

S A Church¹, G M Christian¹, S Hammersley², M J Kappers³, M Frentrup³, R A Oliver³ and D J Binks¹

¹Department of Physics and Astronomy & Photon Science Institute, University of Manchester, UK,

²Department of Electrical and Electronic Engineering, University of Manchester, UK, ³Department of Materials Science & Metallurgy, University of Cambridge, UK

Commercial high-efficiency white light LEDs contain InGaN/GaN quantum wells (QWs) with an internal efficiency of up to 95% [1] at blue wavelengths. In recent years, it has been discovered that the inclusion of a Si doped InGaN underlayer (UL) in the heterostructure can improve the efficiency of recombination [2]. This has been attributed separately to a reduction in threading dislocation density [3], a reduction in strain [4], the UL acting as a carrier source [5], screening of the quantum confined stark effect [6] and a reduction in the point defect density [7]. However, further work is needed to understand the impact of the UL on carrier dynamics.

In this work, we study the effects of carrier transfer between the UL and the QW using photoluminescence experiments. A series of single InGaN/GaN QWs, grown using MOCVD, with a Si-doped underlayer, are investigated, which have been designed to have a significantly reduced internal electric field [8]. In low temperature PL measurements, exciting with photon energy above the barrier bandgap, emission is seen from both the QW and the UL. As the temperature increases, the emission from the UL quenches rapidly and so only emission from the QWs is visible at room temperature. When a smaller excitation photon energy is used to selectively excite the QW, no emission is observed from the UL and the QW intensity quenches much faster with temperature. As shown in Figure 1, this has the effect of increasing the apparent recombination efficiency at room temperature.

Low temperature PL-excitation spectra show a strong absorption at the UL bandgap energy when detecting emission from the QW, as shown in Figure 2. This suggests that carrier transfer from the UL to the QW occurs at low temperature, and in fact, the majority of carriers that recombine in the QW originate from the UL. This transfer may become more prominent at higher temperatures, and thus account for the results in Figure 1. These results highlight the potential importance of the UL acting as a source of carriers. We will also present the UL's impact on time-resolved measurements.

- [1] N. Bardsley et al. Solid-State Lighting RD Plan (US Department of Energy, 2015).
- [2] M. J. Davies, *Journal of Applied Physics*, 2016, 119, 5, 055708.
- [3] H. Takahashi et al. *Japanese Journal of Applied Physics*, 2000, 39, 6B, L569.
- [4] H. Shan et al. *Japanese Journal of Applied Physics*, 2017, 56, 11, 110305.
- [5] N. Otsuji et al. *Journal of Applied Physics*, 2006, 100, 11, 113105.
- [6] G. M. Christian, *Phys. Status Solidi C*, 2016, 13, 5-6, 248-251.
- [7] C. Haller, *Applied Physics Express*, 2019, 12, 3, 034002.
- [8] G. M. Christian, *Japanese Journal of Applied Physics*, 2019, 58, SCCB09.

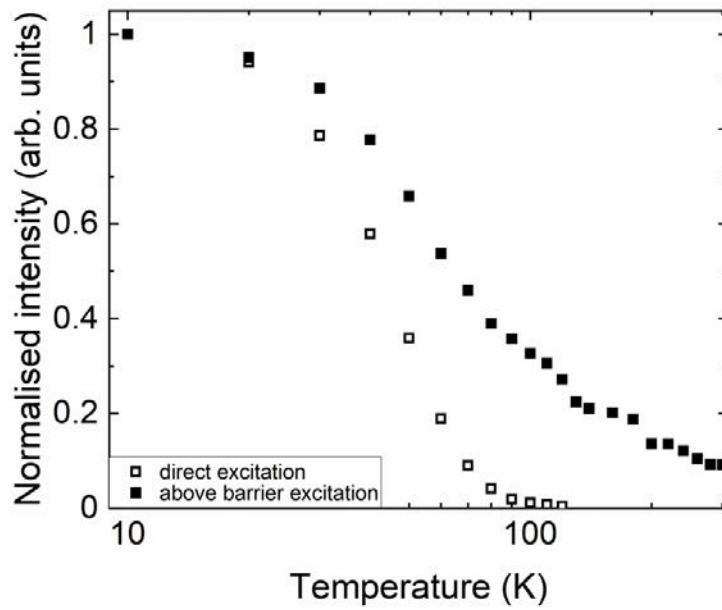


Fig 1. The temperature dependence of the emission intensity from the QW when directly exciting the QW, and when exciting above the barrier energy, and thus exciting both the QW and the UL.

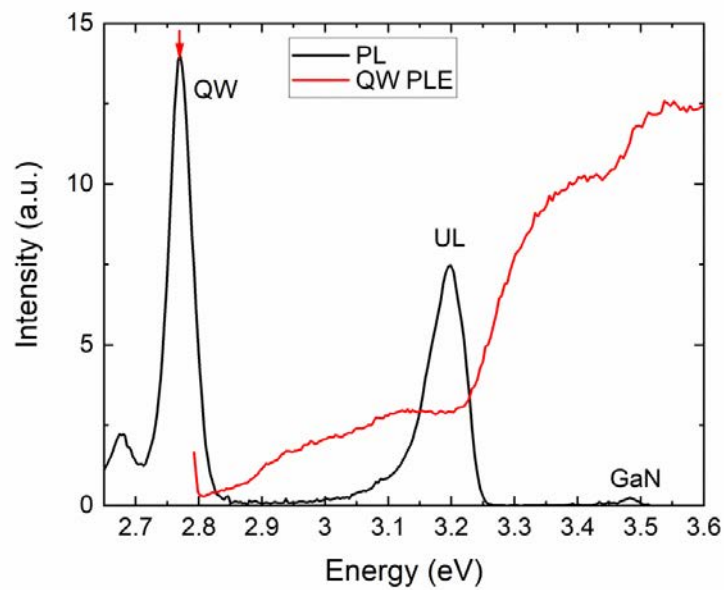


Fig. 2. 10K PL and PL-excitation spectra showing how the QW emission has an absorption edge at the bandgap of GaN, the UL and the QW.

Session 6: Quantum wells and LEDs

Application of GaN-based series-biased micro-LED arrays to long-distance visible light communications

Enyuan Xie¹, Xiangyu He¹, Rui Bian², Mohamed Sufyan Islam³, Cheng Chen³, Jonathan J D McKendry¹, Erdan Gu¹, Harald Haas³, and Martin D Dawson¹

¹Institute of Photonics, University of Strathclyde, UK, ²pureLiFi, UK, ³LiFi Research and Development Centre, University of Strathclyde, UK

In order to satisfy the increased demands of communication services such as high data rates, high connection density, low latency communication and security, visible light communication (VLC) is considered as a favourable solution for 5G and beyond [1]. Compared with the traditional radio-frequency communication, VLC offers attractive advantages including the large available frequency spectrum, high speed, and robustness against interference.

GaN-based micro-light emitting diodes (\square LEDs) are promising candidates as light sources for VLC systems [2]. This is mainly attributed to their high modulation bandwidth, up to hundreds of MHz compared with tens MHz from conventional large-scale LEDs. However, due to the smaller emitting area, the optical power of the single \square LED is relatively low. This strongly limits the data transmission distance of VLC systems using \square LED transmitters. Thus, it is important to develop the high-optical-power \square LED transmitters without sacrificing modulation bandwidth.

Here, we present a novel series-biased \square LED array developed for high-speed VLC systems targeting long distance (> 3 m) applications. The employed series-connection configuration in this array not only enables a multi- \square LED-element operation to produce high optical power but also retains high current density and reduces the array capacitance to increase the modulation bandwidth [3]. An example array, which consists of 3×3 20 μm -in-diameter \square LED elements, has been fabricated from a commercial blue LED wafer, as shown in Fig. 1. As shown in Fig.2(a) and (b), over 10 mW optical power and 980 MHz -6dB electrical modulation bandwidth have been achieved based on this array. Compared with the performance of the single \square LED with the similar size [4], this array presents at least 3 times higher optical power and similar modulation bandwidths at the same operating current density, which confirms the combined high optical power and high modulation bandwidth characteristics of series-biased \square LED arrays. Furthermore, by reducing the element-to-element pitch, the light collection efficiency and, in turn, channel gain of free-space link for the VLC system are also improved. Thanks to these enhancements, by utilising orthogonal frequency division multiplexing modulation, record data transmission rates have been achieved at different transmission distances. As shown in Fig.3, at the forward error correction (FEC) floor of 3.8×10^{-3} , up to 11.74, 11.72, 10.11, 6.58, 2.84 and 1.61 Gbps data transmission rates are achieved at the free-space distances of 0.3, 2, 5, 10, 15, and 20 m, respectively. The results presented in this work not only demonstrate the state-of-art VLC data transmission rates at different distances using \square LED-based transmitters, but also demonstrate the great potential of series-biased \square LED arrays for VLC applications.

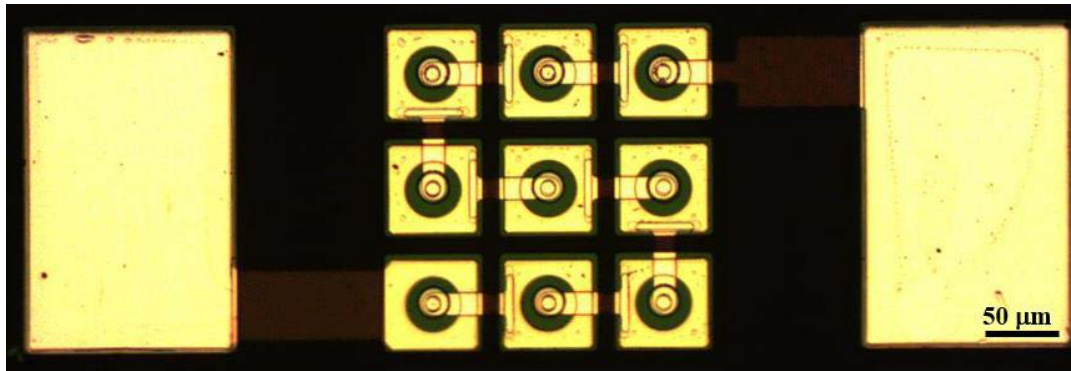


Fig.1. Top-view optical image of the fabricated series-biased \square LED array.

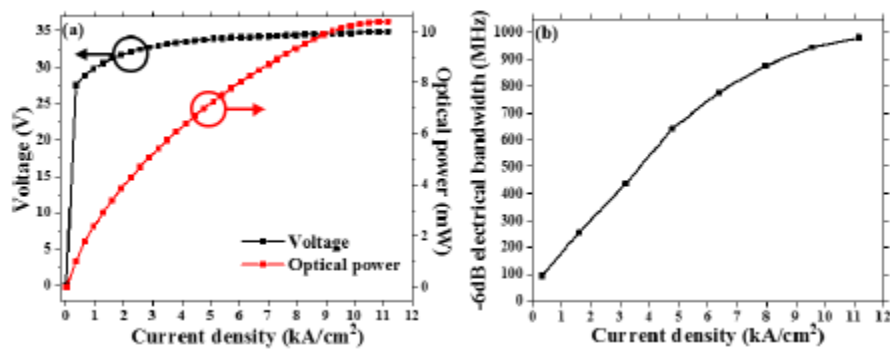


Fig. 2. (a) J-V, L-J, and (b) -6dB electrical bandwidth characteristics of the blue series-biased \square LED array.

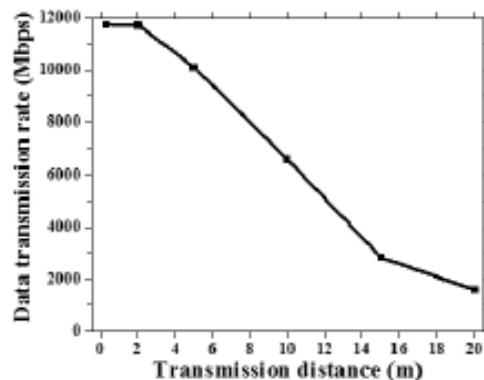


Fig.3. Data transmission rates at the FEC floor at different transmission distances for the free-space VLC system.

- [1] Forecast, G. M. D. T. "Cisco visual networking index: global mobile data traffic forecast update, 2017- 2022." *Update 2017* (2019): 2022.
- [2] James Singh, Konthoujam, Yu-Ming Huang, Tanveer Ahmed, An-Chen Liu, Sung-Wen Huang Chen, Fang-Jyun Liou, Tingzhu Wu et al. "Micro-LED as a Promising Candidate for High-Speed Visible Light Communication." *Applied Sciences* 10, no. 20 (2020): 7384.
- [3] Xie, Enyuan, Xiangyu He, Mohamed Sufyan Islim, Ardimas Andi Purwita, Jonathan JD McKendry, Erdan Gu, Harald Haas, and Martin D. Dawson. "High-speed visible light communication based on a III-nitride series-biased micro-LED array." *Journal of Lightwave Technology* 37, no. 4 (2019): 1180-1186.

- [4] Ferreira, Ricardo XG, Enyuan Xie, Jonathan JD McKendry, Sujan Rajbhandari, Hyunhae Chun, Grahame Faulkner, Scott Watson et al. "High bandwidth GaN-based micro-LEDs for multi-Gb/s visible light communications." *IEEE Photonics Technology Letters* 28, no. 19 (2016): 2023-2026.

Size and wavelength-dependent characterisation of ultraviolet micro-light-emitting diodes

Jonathan J D McKendry¹, Daniel M Maclure¹, Xiaobin Sun², Johannes Herrnsdorf¹, Xiangyu He¹, Enyuan Xie¹, Erdan Gu¹, and Martin D Dawson¹

¹Institute of Photonics, University of Strathclyde, UK , ²Fraunhofer Centre for Applied Photonics, Technology and Innovation Centre (TIC), UK

Ultraviolet light of wavelength 100-400 nm has many possible applications, including photolithography, water purification, disinfection of surfaces, sensing and optical communications [1]. However, the wider deployment of UV light in these applications has been hampered by bulky, fragile and inefficient UV sources such as mercury-vapour lamps. In recent years AlGaIn-based UV-emitting light-emitting diodes (LEDs) have rapidly matured in terms of their efficiency and output power and are beginning to make an impact on these fields.

One application of emerging importance is optical wireless communications (OWC) using UV light. A unique benefit of using UV for OWC is that the ozone layer strongly absorbs most solar emission in the UVB-UVC region of the electromagnetic spectrum; as a result, terrestrial UV communications can operate in a virtually noiseless environment. Furthermore, strong scattering of light at these wavelengths means non-line of sight communications are made possible by scattering transmitted signals off the atmosphere [2].

In this work we present a study of the characteristics of micro-pixelated LEDs ('micro-LEDs', i.e. LEDs with dimensions < 100 μm) with peak emission in the UVC (280 nm), UVB (300 nm) and UVA (375 nm) spectral regions. We previously demonstrated a 1 Gb/s line-of-sight OWC using a similar UVC micro-LED [3]. The optical output power versus current (L-I) and -3dB modulation bandwidth, two key metrics for OWC, are presented for the three wavelengths. Figure 1 shows the L-I plots for pixels approximately 435 μm^2 in area, showing 0.24, 0.15 and 0.75 mW maximum CW output power for the 280, 300 and 375 nm micro-LEDs, respectively. Figure 2 shows the frequency response from micro-LEDs at these three wavelengths, at an injected current of 10 mA. Features in the response curves, attributed to impedance mismatch, at frequencies < 10 MHz make unambiguously defining the -3dB bandwidth of each micro-LED challenging, but taking the point in the curves with the highest response as the reference point the electrical-to-electrical -3dB bandwidths are approximately 404, 438 and 104 MHz for the 275, 300 and 375 nm micro-LEDs, respectively. The corresponding electrical-to-optical bandwidths are 645, 716 and 182 MHz. These are amongst the highest values reported for UV-emitting LEDs.

These bandwidths also suggest that sub-nanosecond optical pulses from these UV-emitting micro-LEDs should be possible, which would be applicable to time-of-flight applications, optical sensing and some OWC configurations. Figure 3 shows an optical pulse measured from a 275 nm micro-LED in response to an ~ 150 ps electrical pulse from a commercial pulse generator. The full width half maximum (FWHM) of the pulse is 800 ps, however, this represents the temporal resolution limit of the photoreceiver and oscilloscope combination used to record the pulsewidth, so the actual optical pulse width may be significantly shorter, which will be explored in future work.

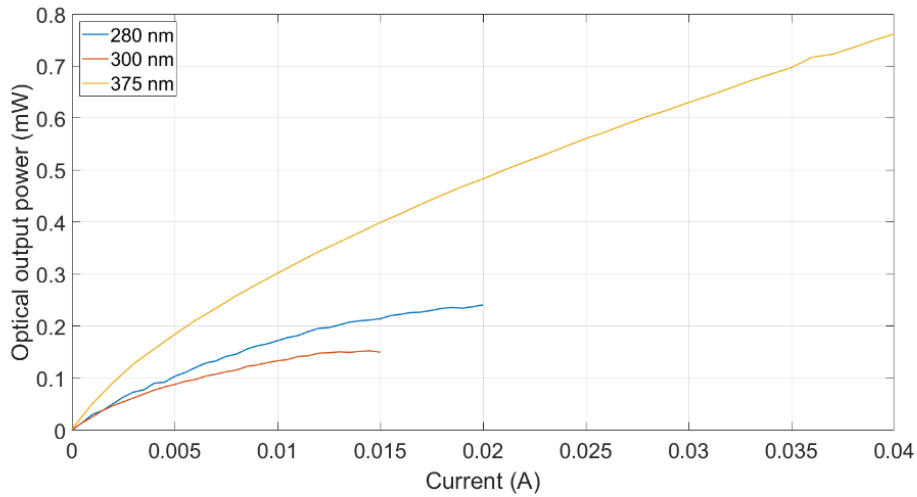


Fig. 1. CW output power versus current for micro-LEDs of different wavelength.

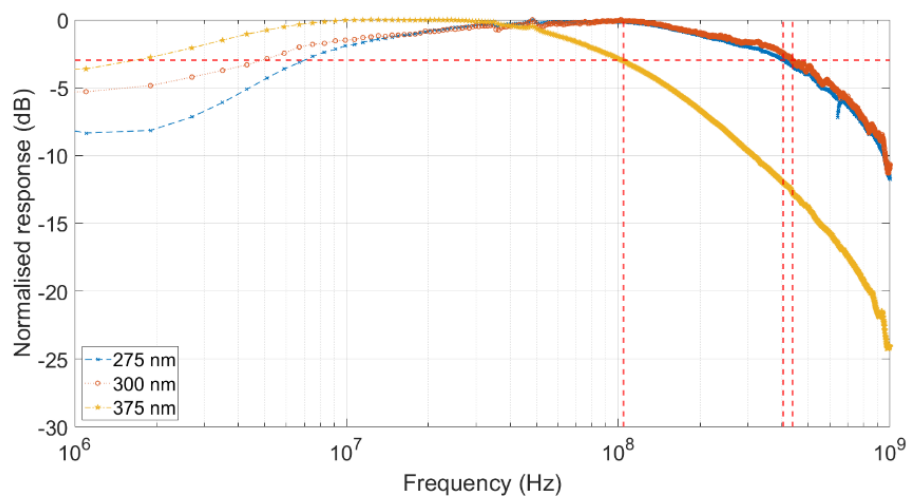


Fig. 2. frequency response of three UV-emitting micro-LEDs with peak emission of 275, 300 and 375 nm. Injected current is 10 mA for all. Dashed lines indicate -3dB bandwidths.

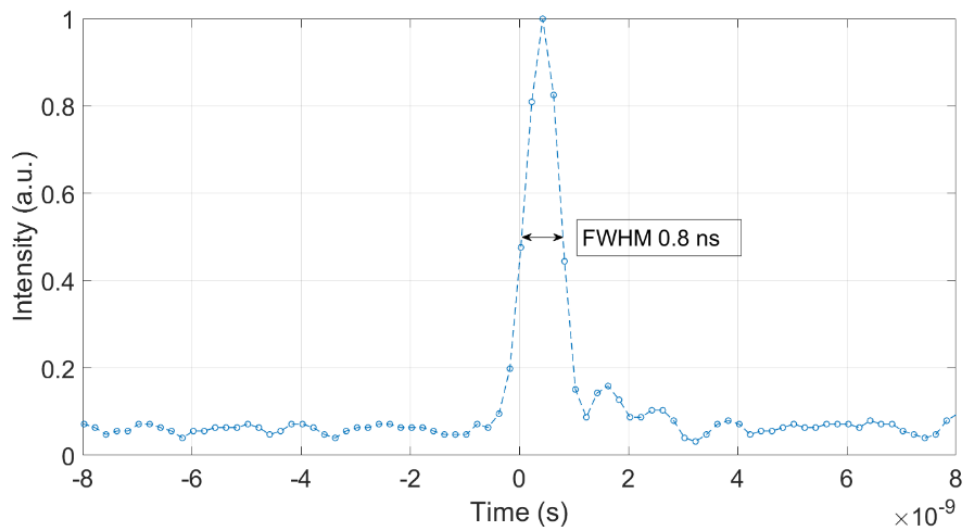


Fig. 3. 800 ps FWHM optical pulse recorded from a 275 nm peak emission micro-LED.

- [1] M. Kneissl, T.-Y. Seong, J. Han, and H. Amano, "The emergence and prospects of deep-ultraviolet light-emitting diode technologies," *Nat. Photonics*, vol. 13, no. 4, pp. 233–244, 2019, doi: 10.1038/s41566-019-0359-9.
- [2] A. Vavoulas, H. G. Sandalidis, N. D. Chatzidiamantis, Z. Xu, and G. K. Karagiannidis, "A Survey on Ultraviolet C-Band (UV-C) Communications," *IEEE Commun. Surv. Tutorials*, vol. 21, no. 3, pp. 2111–2133, 2019, doi: 10.1109/COMST.2019.2898946.
- [3] X. He *et al.*, "1 Gbps free-space deep-ultraviolet communications based on III-nitride micro-LEDs emitting at 262 nm," *Photonics Res.*, vol. 7, no. 7, p. B41, Jul. 2019, doi: 10.1364/PRJ.7.000B41.

Effect of localised state filling and defect density on the efficiency of InGaN/GaN QWs

R Barrett¹, R Ahumada Lazo¹, M J Kappers², R A Oliver² and D J Binks¹

¹Dept. of Physics and Astronomy & Photon Science Institute, University of Manchester, UK, ²Department of Materials Science and Metallurgy, University of Cambridge, Cambridge, UK

Above an onset value, the internal quantum efficiency of InGaN/GaN quantum wells (QWs) begins to decrease with increasing carrier density. Several explanations for this phenomenon, known as 'droop', have been proposed, including: Auger recombination [1], defect-assisted Auger recombination [2], carrier escape from the QWs [3], and the saturation of localisation sites [4]. In the latter explanation, as localisation sites are filled, additional carriers have increased mobility and are therefore more likely to encounter defects and recombine non-radiatively [5].

The characteristic 's-shaped' temperature dependence of the peak energy of photoluminescence (PL) from InGaN/GaN QWs (see Figure 1a,b) is caused by the redistribution of carriers between localised states as the temperature rises [6]. However, as the carrier density increases these localised states become progressively filled, limiting redistribution and suppressing the s-shape dependence (Fig. 1c).

In this work, the temperature dependence of the peak emission energy is compared to that of the PL intensity at different excitation levels for a series of blue- and a series green-emitting InGaN/GaN QW samples grown at different temperatures, with consequently different point defect densities [7]. At low and medium excitation, corresponding to pumping by cw laser at a wavelength of 325 nm with intensities of 0.78 W.cm⁻² and 8.5 W.cm⁻² respectively, the s-shaped dependence of peak energy is observed and the PL intensity decreases continuously as the temperature rises (Fig. 1a,b). In contrast, at a high excitation intensity of 450 W.cm⁻² both the peak energy and PL intensity are approximately constant until a temperature of about 120 K is reached and then both reduce simultaneously as the temperature is increased (Figure 1c). This suggests that that the redistribution of carriers between localised states plays an important role in the temperature dependence of PL intensity for low and medium excitation levels but is much less important at higher excitation levels. The implications of these findings for our understanding of droop will be discussed.

- [1] J. Iveland, L. Martinelli, J. Peretti et al, *Phys. Rev. Lett.* **110** 177406 (2013)
- [2] A. David, N. G. Young, C. A. Hurni et al, *Phys. Rev. Applied* **11** 031001 (2019)
- [3] Q. Dai, M. F. Schubert, M. H. Kim et al, *Appl. Phys. Lett.* **94** 111109 (2009)
- [4] G. Verzellesi, D. Saguatti, M. Meneghini, et al, *J. Appl. Phys.* **114** 071101 (2013)
- [5] J. Hader, J. V Moloney, and S. W. Koch, *Appl. Phys. Lett.* **96** 221106 (2010)
- [6] T. J. Badcock, S. Hammersley, D. Watson-Parris et al, *Jpn. J. Appl. Phys.* **52** 08JK10 (2013)
- [7] S. Hammersley, M. J. Kappers, Fabien C. P. Massabuau et al, *Phys. Status Solidi C* **13** 209– 213 (2016)

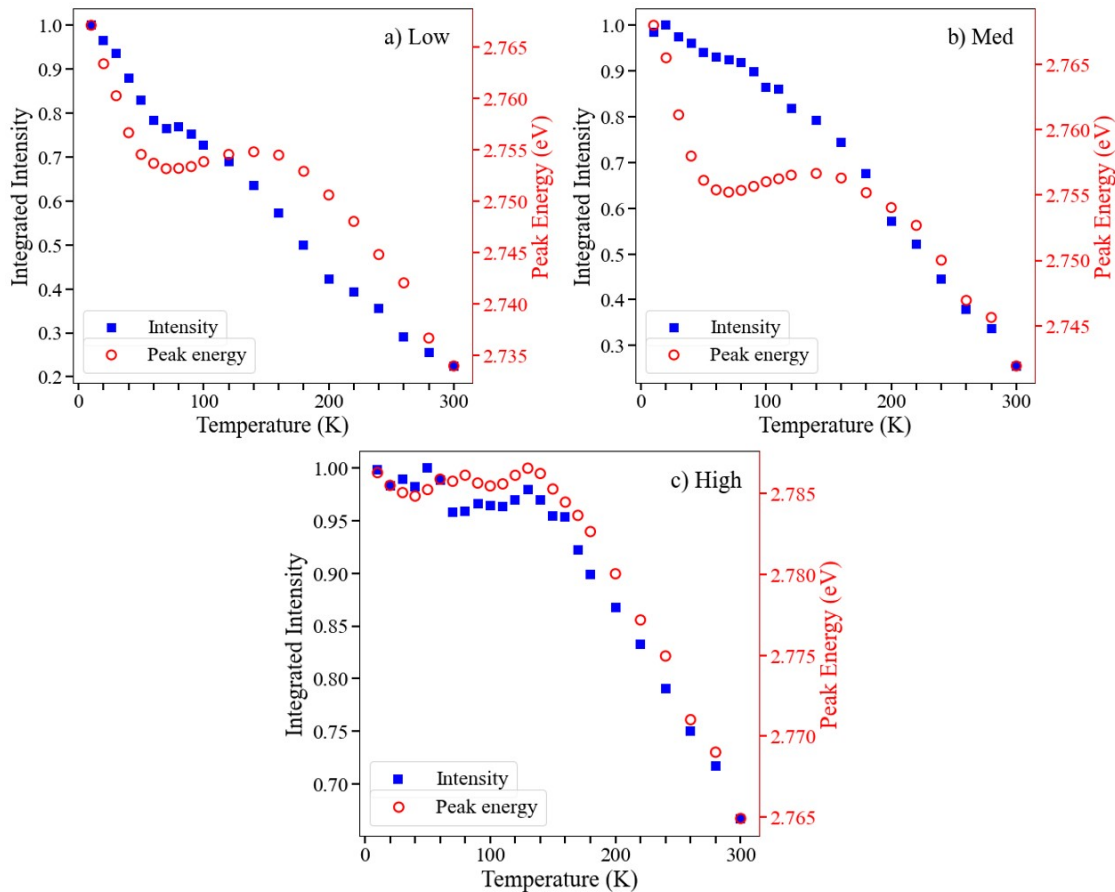


Fig. 4. Temperature dependence of integrated PL intensity (left axes & filled squares) and peak emission energy (right axes & empty circles) for the blue-emitting sample with QW growth temperature 730°C at low (a), medium (b) and high (c) excitation levels, produced by pumping with a cw laser at wavelength of 325 nm and intensities of 0.78 W.cm⁻², 8.5 W.cm⁻² and 450 W.cm⁻², respectively.

A comparison of efficiency droop in wurtzite and zincblende InGaN/GaN quantum wells

S A Church¹, R Ahumada-Lazo¹, M J Kappers², M Frentrup², D J Wallis^{2,3}, R A Oliver² and D J Binks¹

¹Department of Physics and Astronomy & Photon Science Institute, University of Manchester, UK,

²Department of Materials Science & Metallurgy, University of Cambridge, UK, ³Centre for High Frequency Engineering, University of Cardiff, UK

The peak internal efficiency of radiative recombination in wurtzite (wz) c-plane InGaN/GaN quantum wells (QWs) can be as high as 95% at blue wavelengths [1]. However, increasing the injected current density to achieve higher intensities leads to a reduction in the recombination efficiency: this is known as efficiency droop [2]. Droop is an area of much study in the literature, and has been separately attributed to carrier leakage [3], poor hole injection [4], the saturation of localised states [5] and Auger recombination [6].

In recent years, InGaN/GaN QWs grown in the zincblende (zb) phase have arisen as a promising candidate to replace the wurtzite structure. The zb-QWs are free of the built-in electric fields present in c-plane wz-QWs, and this results in a faster radiative recombination rate, which may lead to higher recombination efficiencies than the established technologies. However, to fully assess the merit of zb-QWs, their performance in the high carrier density regime must be studied to determine if efficiency droop also occurs in these structures.

In this paper, we study the low temperature photoluminescence spectra of a zb-QW, grown using MOCVD on 3C-SiC/Si (001) substrates, under pulsed excitation. These results are directly compared with a c-plane wz-QW where droop has already been observed [7]. The integrated intensity divided by excitation power for each sample is shown in Figure 1. The polar wz-QWs experience a reduction in efficiency for carrier densities above $1 \times 10^{11} \text{ cm}^{-2} \text{ pulse}^{-1} \text{ QW}^{-1}$. This droop coincides with a blueshift in the peak energy. In contrast, the zb-QW experiences the onset of droop at the significantly higher carrier density of $5 \times 10^{12} \text{ cm}^{-2} \text{ pulse}^{-1} \text{ QW}^{-1}$, which is promising for applications in high luminosity LEDs, although there may be still some work to do to increase the peak efficiency of the zb-QWs. We will discuss possible explanations for this behaviour.

- [1] N. Bardsley et al. Solid-State Lighting RD Plan (US Department of Energy, 2015).
- [2] J. Cho, Laser & Photonics Reviews, 2013, 7, 3, 408-421.
- [3] M. F. Schubert, Applied Physics Letters, 2009, 94, 8, 23-26.
- [4] I. A. Pope, Applied Physics Letters, 2003, 82, 17, 2755-2757.
- [5] J. Hader, Applied Physics Letters, 2010, 96, 22, 221106.
- [6] Y. C. Shen, Applied Physics Letters, 2004, 91, 14, 141101.
- [7] M. J. Davies, Applied Physics Letters, 2016, 108, 25, 252101.

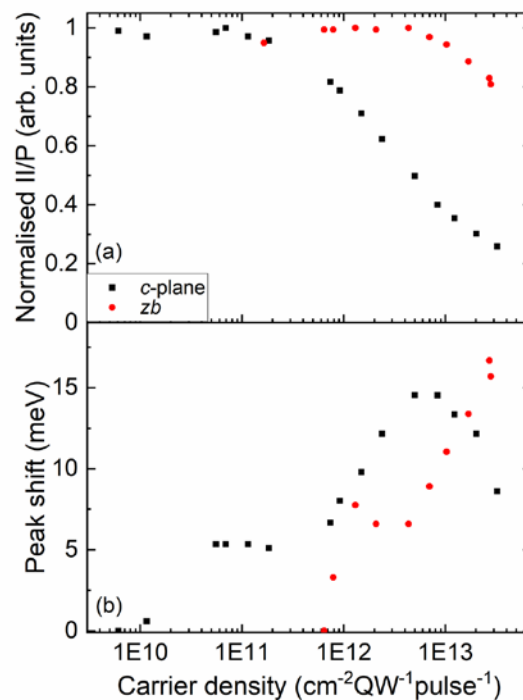


Fig 1. 10K high power PL measurements of c-plane and zb InGaN/GaN SQWs. (a) Is the normalised integrated intensity/power which is proportional to the recombination efficiency. (b) is the peak shift of the PL, relative to the lowest power measurement.

Session 7: Electronic devices

Evaluation of doping profiles by UV-induced increase in channel conductivity in AlGaIn/GaN High Electron Mobility Transistors

Markus Wohlfahrt¹, Michael Uren¹, Hassan Hirshy², and Martin Kuball¹

¹Centre for Device Thermography and Reliability (CDTR), University of Bristol, UK, ²IQE Europe, Cardiff, UK

We demonstrate a new measurement to probe the channel doping in AlGaIn/GaN High Electron Mobility Transistors (HEMTs) based on an UV-induced increase in channel conductivity (persistent photoconductivity – PPC). We demonstrate that this is a generic effect occurring for a wide range of HEMT configurations, however, its magnitude is largest for buffers where background Carbon has made it p-type. We have developed a quantitative model and show this effect can be attributed to a UV-induced shift in bulk Fermi level which persists for days to weeks. The PPC effect allows the net deep-level doping density (i.e. $|N_A - N_D|$) below the 2DEG to be measured, a quantity which is extremely difficult to evaluate by any other means.

It has been reported before that illuminating AlGaIn/GaN HEMTs with UV light increases the channel conductivity [1], however, there is no clear conclusion to how this effect occurs and what defines the magnitude and recovery time constants. Some reports assign the effect to surface traps and their charge state [2-5], others attribute the effect to absorption in the buffer and potentially in the barrier as well [6, 7].

The effect can be explained by considering the effect of UV-induced charge accumulation in the buffer (Fig. 1). Initially, before the UV illumination, the electron and hole Fermi level is pinned at the Carbon acceptor level (Fig. 1a) which defines the hole concentration in the buffer (Fig. 1c). Increasing the illumination power causes an accumulation of electrons in the buffer. At a certain point, the charge generation in the buffer exceeds the leakage capabilities of the buffer and both electron and hole concentrations become comparable (Fig. 1d) causing the bands to bend down (Fig. 1b). The magnitude can be explained by considering a channel-buffer capacitor defined by the depletion region. The depletion width is determined by the difference in Carbon acceptor (CN) and donor (background donors and CGa) concentrations in both channel and buffer. The higher CN-CGa, the narrower is the depletion region. That causes a higher change in capacitive charge caused by the potential change due to band bending. This leads to a higher increase in electron concentration in the 2DEG and ultimately a higher increase in channel conductivity.

Here as examples we use two Fe-doped GaN-on-SiC structures with different doping profiles (Fig. 2). Wafer A exhibits a higher conductivity increase of 7.5% compared to Wafer B with 5.9% (Tab. I). Comparing the measured PPC values with different simulated cases for varying NA-ND (Fig. 3) shows a good agreement and an inconsistency of Wafer B being n-type. The determined values of NA-ND also nicely correspond to the SIMS measurements (Fig. 2).

The PPC effect is particularly sensitive to the channel doping and the difference NA-ND as this dominantly defines the depletion width. Measuring SIMS generally only yields the magnitude of the Carbon doping but no information about the ratio of donors and acceptors. The UV-induced increase in channel conductivity can consequently be used to investigate the channel donor concentration.

- [1] Z.H. Zaidi *et al.*, IEEE Transactions on Electron Devices. **60**, 2776-2781 (2013).
- [2] Y.-C. Chang *et al.*, Journal of Applied Physics. **107**, 033706 (2010).
- [3] G. Koley *et al.*, Journal of Applied Physics. **96**, 4253-4262 (2004).
- [4] R. Vetry *et al.*, IEEE Electron Device Letters. **48**, 560-566 (2001).
- [5] Y.-C. Chang *et al.*, Japanese Journal of Applied Physics. **46**, 3382-3384 (2007).
- [6] Y. Huang *et al.*, Applied Physics Letters. **96**, 243503 (2010).
- [7] A. Caddemi *et al.*, Microelectronics Reliability. **65**, 310-317 (2016).
- [8] M. Singh *et al.*, IEEE Transactions on Electron Devices. **65**, 3746-3753 (2018).

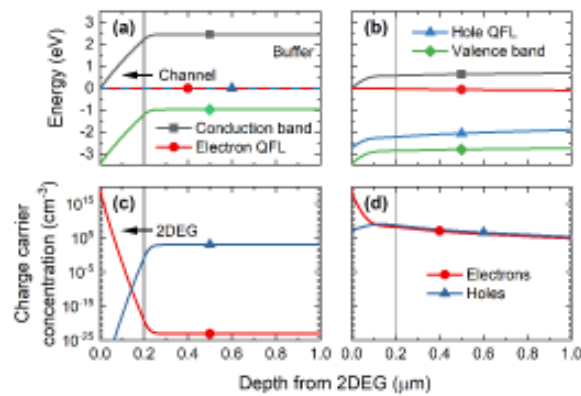


Figure 2. Doping densities for the three simulated cases for Wafer A (case 1) and Wafer B (case 2 with simulated p-type buffer and case 3 with simulated ntype buffer) overlaid with the measured SIMS profiles. CN corresponds to Carbon acceptors, CGa corresponds to Carbon donors. From Ref. [8].

Table I. Measured and simulated increase in channel conductivity induced by UV light.

	Wafer A	Wafer B (p-type) ^a	Wafer B (n-type) ^a
Measured	7.5 ± 1.8 %	5.9 ± 1.5 %	
Simulated	8.0 %	6.5 %	1.7 %

^a Buffer Carbon doping for simulation

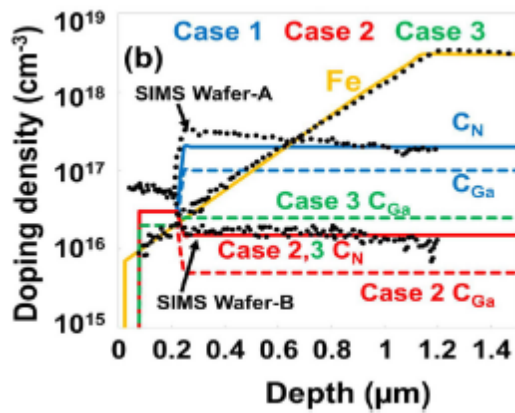


Figure 1. Wafer A band diagram cross-section (top) and corresponding charge carrier concentration (bottom) for the initial solution in darkness (left) and 10⁻⁴ W/cm² of the static UV illumination (right). UV-induced electrons in the bulk are trapped and take days to re-equilibrate. They shift the Fermi level and reduce surface depletion charge and increase the 2DEG density.

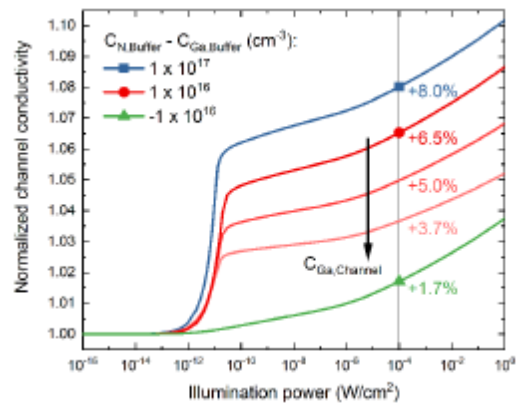


Figure 3. Simulated static normalized channel conductivity for increasing UV illumination power for different buffer NA-ND, i.e. C_{N,Buffer} - C_{Ga,Buffer}. The arrow symbolizes increasing channel donor density from the nominal 2 × 10¹⁶ cm⁻³ to 3 × 10¹⁶ cm⁻³ and 4 × 10¹⁶ cm⁻³ for the case with the circle symbol. The vertical line represents the experimentally used power of 10⁻⁴ W/cm².

Crystalline AlGa_N & SiC Interlayers for Integration of Diamond with GaN

Daniel E Field^{1,2}, Jerome A Cuenca³, Matthew Smith⁴, Simon M Fairclough⁵, Fabien C-P Massabuau^{5,6}, James W Pomeroy¹, Oliver A Williams³, Rachel A Oliver⁵, Iain Thayne⁴, and Martin Kuball¹

¹Centre for Device Thermography and Reliability, University of Bristol, UK, ²Centre for Diamond Science and Technology, University of Warwick, UK; ³Diamond Foundry, University of Cardiff, UK, ⁴James Watt School of Engineering, University of Glasgow, UK, ⁵Cambridge Centre for Gallium Nitride, University of Cambridge, UK, ⁶Department of Physics, University of Strathclyde, UK

Improvement of thermal management in GaN high electron mobility transistors (HEMT) is vital for improved device reliability. In this work, we explore the use of crystalline interlayers for the integration of diamond heat sinks with GaN. This reduces the effective thermal boundary resistance (TB_{Reff}) between GaN and diamond compared to commonly used amorphous interlayer materials such as SiN. Crystalline Al_{0.32}Ga_{0.68}N interlayers have been incorporated within a GaN HEMT structure. Diamond was grown directly on this layer as well as on an additional, 10 nm thick, crystalline SiC layers. TB_{Reff} was characterised using transient thermoreflectance and found to be 107±44 m² K GW⁻¹ without SiC and 30±5 m² K GW⁻¹ with SiC, with potential to improve TB_{Reff} in the future with further materials optimization.

I. INTRODUCTION

Gallium nitride high electron mobility transistors (HEMTs) are promising devices for high-power high-frequency amplifiers and have been demonstrated at operating at 20 W mm⁻¹ in the X-band. Such devices would enable the next generation of communication technologies [1]. Despite this, commercial devices are derated from high-power densities to prevent over-heating and increase reliability. Improved thermal management would decrease the peak temperatures occurring within the device making high power density devices more viable.

Diamond with its large bulk thermal conductivity (~2000 W m⁻¹ K⁻¹ [2]), is an excellent candidate to act as a heterogenous heat sink for GaN RF devices. Typical diamond integration involves removal of the GaN growth substrate, deposition of a thin SiN_x layer on the GaN followed by polycrystalline diamond growth. It is important to minimise the thermal resistance between the GaN and diamond to see the true benefit of the diamond. Currently, the amorphous SiN_x which has a low thermal conductivity (~2 W m⁻¹ K⁻¹) introduces a significant TB_{Reff}. This can be reduced by thinning the SiN_x, and interlayers < 10 nm thick have resulted in very low TB_{Reff}. [3]. However, such thin layers may not offer the necessary protection to the GaN from the harsh diamond growth conditions [4]. Alternatively, crystalline material could be used for the interlayer to increase its thermal conductivity.

In this work, a ~20 nm thick Al_{0.32}Ga_{0.68}N interlayer has been integrated within an AlGa_N/GaN HEMT device epitaxy. Diamond has been grown on this layer with and without an additional SiC layer. The TB_{Reff} of both samples has been extracted using transient thermoreflectance (TTR).

2. EXPERIMENTAL METHODS

AlGa_N/GaN-on-Si standard HEMT structures were grown by metal organic chemical vapour deposition, with a ~20 nm Al_{0.32}Ga_{0.68}N layer 750 nm below the channel. Two samples were prepared using different fabrication techniques (Fig. 1). For sample 1, the wafer was flipped and bonded to a Si handle wafer [5]. The Si growth substrate was removed using chemical-mechanical lapping and a reactive ion etch. Sample 2 utilised a membrane process [6]. In brief, a Bosch process was used to selectively etch ∅ 0.5 mm holes in the Si growth substrate. Following removal of the Si substrate for both samples, AlGa_N etch stop was revealed using a two stage inductively coupled plasma etch [9], [10].

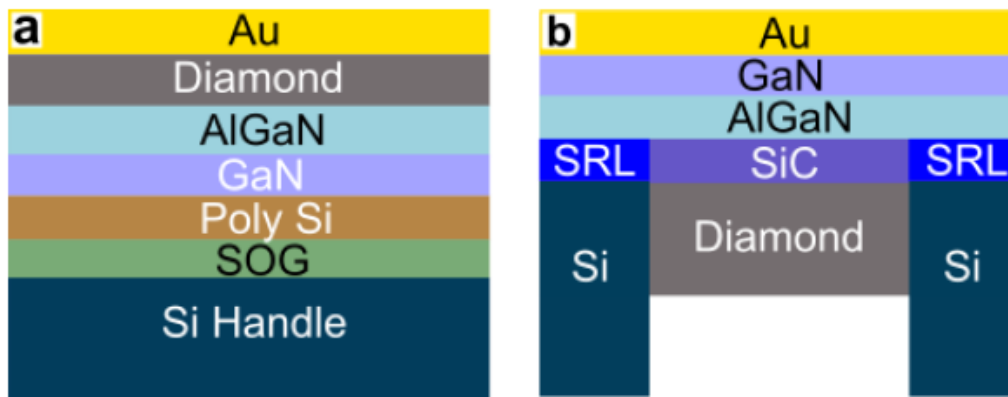


Fig. 1. Structures of sample 1 (a) and sample 2(b) after diamond growth and transducer deposition.

Diamond was then grown using a similar process to that used for growth on crystalline AlN [9]. This involves a N₂/H₂ plasma flash pre-treatment prior to diamond growth at ~ 800°C. A 35 µm film was grown on sample 2 and ~ 1 µm film grown on sample 1. During the plasma pre-treatment for sample 2, unetched Si was sputtered and redeposited onto the AlGaN before reacting with carbonaceous species in the diamond growth plasma to form SiC.

Scanning transmission electron microscopy (STEM) and energy dispersive x-ray spectroscopy (EDS) were used to characterise the interfaces. The samples were coated in 10 nm Cr and 145 nm Au by thermal evaporation to give a transducer for TTR. This technique uses a 355 nm nanosecond pulsed pump laser to periodically heat the sample surface. Simultaneously, a low power, continuous wave 532 nm laser tracks the reflectivity of the surface. This is linearly proportional to the temperature change of the surface and can be used to extract thermal properties of the material by solving the heat diffusion equations in a multilayer stack and using least squares fitting between the model and experimental data [10].

3. RESULTS & DISCUSSION

Fig. 2 shows the cross section TEM and EDS of sample 1 and 2. These show that the selective etch process successfully stopped on the AlGaN etch stop. Fig. 2d shows the presence of a 10 nm thick SiC layer at the diamond/AlGaN interface. We believe this layer forms after diamond seeding as TEM images show a nanodiamond seed flush with the AlGaN layer (Fig. 2c).

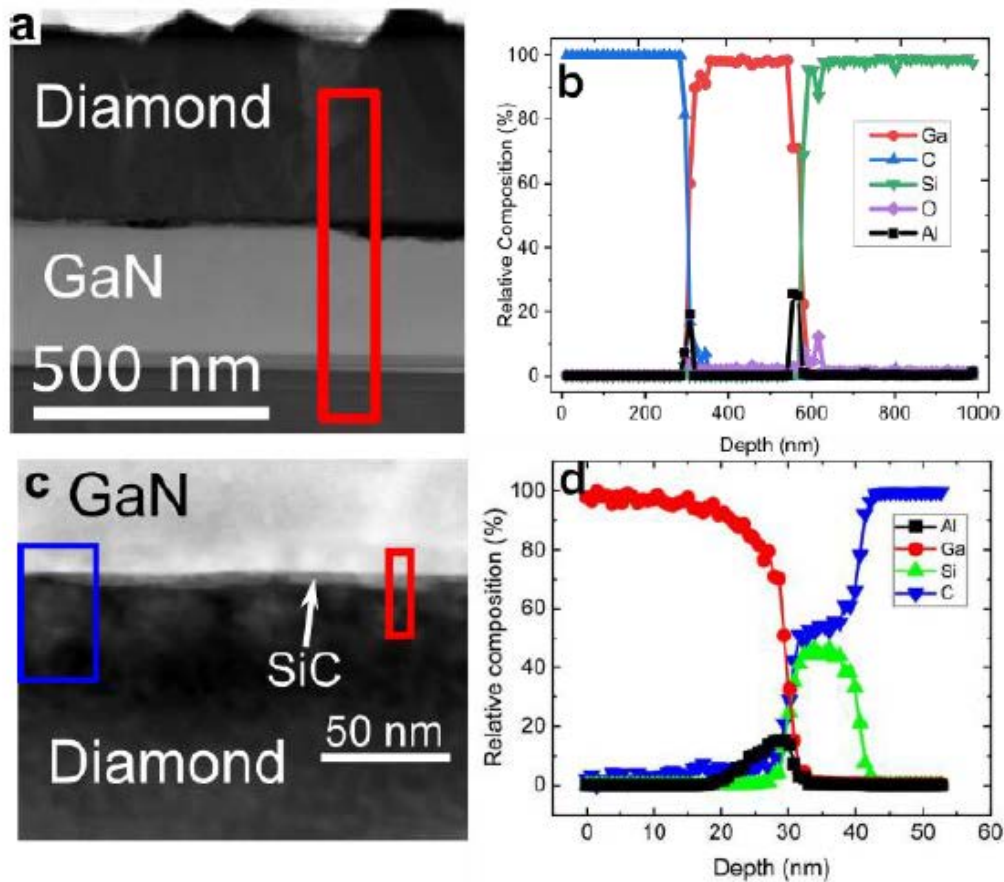


Fig. 2. TEM & EDS of the diamond GaN interface of sample 1 (a & b) and 2 (c & d). Red boxes show where EDS were taken. Blue box in (c) contains a nanodiamond seed.

Representative TTR traces are shown in Fig. 3. It was necessary to fit the thermal resistance between the Au transducer and the sample, and the diamond thickness of sample 1 in addition to TB_{eff} . Whilst sample 1 had a larger TB_{eff} ($104 \pm 44 \text{ m}^2 \text{ K GW}^{-1}$), sample 2 had a TB_{eff} of $30 \pm 5 \text{ m}^2 \text{ K GW}^{-1}$ comparable to the state of the art for SiN_x layers of similar thickness [11]. We believe this occurs as the SiC aids adhesion of the diamond to the AlGaN. Whilst diamond has been shown to be adherent to single crystal AlN with a low TB_{eff} [9], $\text{Al}_{0.32}\text{Ga}_{0.68}\text{N}$ has a low Al % and is more GaN like. There is yet to be any success of direct diamond growth on GaN which is assumed to be due to the lack of covalent bonding between the two. Lower TB_{eff} can be achieved by optimisation of SiC formation and using high Al composition interlayers.

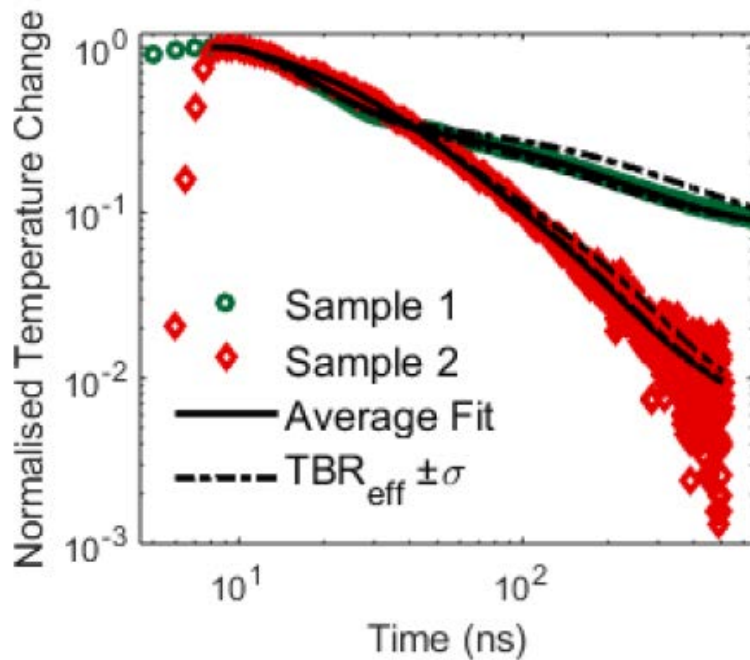


Fig. 3. TTR traces and fits of sample 1 and 2. The dashed lines show the effect of \pm one standard deviation of TBR_{eff} .

4. CONCLUSIONS

We have demonstrated the use of an integrated crystalline $Al_{0.32}Ga_{0.68}N$ interlayer for the growth of diamond on a GaN HEMT structure. Direct growth on this layer resulted in a high TBR_{eff} ($107 \pm 44 \text{ m}^2 \text{ K GW}^{-1}$), but the addition of a SiC layer between the AlGa_N and diamond reduced this to $30 \pm 4 \text{ m}^2 \text{ K GW}^{-1}$ similar to equivalent SiN_x layers. Whilst low Al% AlGa_N may not be viable as an interlayer, we believe AlN, SiC, and high Al% AlGa_N all offer promising routes forward in the pursuit of minimising TBR_{eff} .

Acknowledgements - The authors acknowledge financial support from the Engineering and Physical Sciences Research Council (EPSRC) under the program Grant GaN-Dame (Grant No. EP/P00945X/1). DF's studentship is cofounded by the EPSRC (EP/L015315/1) and Element-Six Technologies. We thank D. Francis (Akash Systems) for wafer bonding.

REFERENCES

- [1] A. Bar-Cohen *et al.*, vol. 141, no. 4, pp. 1-14, 2019.
- [2] D. G. Onn *et al.*, *Phys. Rev. Lett.*, vol. 68, no. 18, pp. 2806-2809, 1992.
- [3] L. Yates *et al.*, *ACS Appl. Mater. Interfaces*, vol. 10, no. 28, pp. 24302-24309, 2018.
- [4] D. Liu *et al.*, *Scr. Mater.*, vol. 128, pp. 57-60, 2017.
- [5] K. D. Chabak *et al.*, *IEEE Electron Device Lett.* Vol. 31, No. 2, Febr. 2010, vol. 31, no. 2, pp. 99-101, 2010.
- [6] M. D. Smith *et al.*, *AIP Adv.*, vol. 10, no. 3, pp. 1-6, 2020.
- [7] M. D. Smith *et al.*, *Appl. Surf. Sci.*, vol. 521, no. December 2019, 2020.
- [8] Y. Han *et al.*, *Japanese J. Appl. Physics, Part 2 Lett.*, vol. 42, no. 10 A, pp. 8-11, 2003.
- [9] S. Mandal *et al.*, *ACS Appl. Mater. Interfaces*, 2019.
- [10] Y. Zhou *et al.*, *ACS Appl. Mater. Interfaces*, vol. 9, no. 39, pp. 34416-34422, 2017.
- [11] H. Sun *et al.*, *Appl. Phys. Lett.*, vol. 106, no. 11, 2015.

Dual metal gate AlGaIn/GaN HEMTs with improved transconductance and reduced short channel effects

Joseph Pinchbeck, Sheng Jiang, Peter Houston, and Kean Boon Lee

Department of Electronic and Electrical Engineering, The University of Sheffield, UK

AlGaIn/GaN high electron mobility transistors (HEMTs) have been an area of increasing research particularly in high frequency and high power applications. Performance in high frequency applications requires device layouts with a small gate length and high transconductance. Reducing the gate length to achieve this higher transconductance, however, will lead to drain induced barrier lowering (DIBL) effect in which the threshold voltage varies with drain bias. One approach to achieve a high transconductance and reduce DIBL in HEMTs is by introducing a dual metal gate (DMG) topology.^{1,2} This study uses both simulation results and experimental results to demonstrate the advantages brought about by employing a DMG in comparison with the conventional single metal gate (SMG) configuration on AlGaIn/GaN HEMTs.

Figure 1(a) shows the SEM image of the AlGaIn/GaN HEMT with Pd/Ti DMG. An improvement in peak transconductance (212 mS/mm) of the Pd/Ti DMG HEMTs is measured compared to that of the Pd SMG HEMTs (200 mS/mm) with a total gate length of 400 nm as shown in Figure 1(b). Figure 2(a) shows the TCAD simulated electric field profile of the DMG and SMG configurations at $V_{ds} = 10$ V and $V_{gs} = 0$ V. An additional peak in the electric field is present between the two gates in the device with Pd/Ti DMG due to the work function difference between the two metals. This additional peak in the electric field leads to a higher average electron velocity in the channel over the gate region and hence a higher transconductance in the DMG HEMTs.

Figure 3 shows experimental gate transfer characteristics of the DMG and SMG devices with different drain biases. SMG HEMTs exhibit a DIBL of 37 mV/V with a drain bias voltage between 0.1 V and 10 V. In comparison, the threshold voltage of the Pd/Ti DMG devices was less sensitive to the drain bias changes with a DIBL of 19 mV/V when subjected to the same drain bias range. An increase in the off-state leakage current is also seen in SMG HEMTs which is attributable to the inability to fully pinch off the device channel region, as a result of the DIBL. A two-step profile in the simulated electrostatic potential along the channel is observed in the Pd/Ti DMG HEMTs as shown in Figure 2(b). This acts to spread out the depletion region in the channel and the screening effect reduces the sensitivity of DIBL with the drain bias variation when compared to the SMG HEMTs. These results demonstrate the potential of DMG structure in the AlGaIn/GaN HEMTs for high frequency applications with sub- μ m gate length.

- [1] W. Long, J-M. Kuo and K. K. Chin, IEEE Transactions on Electron Devices 46, 865 (1999).
- [2] K. B. Lee, H. Sun, L. Yuan, W. Wang, S. L. Selvaraj and G. Q. Lo, 2012 IEEE International Symposium on Radio-Frequency Integration Technology (RFIT), 7-9 (2012).

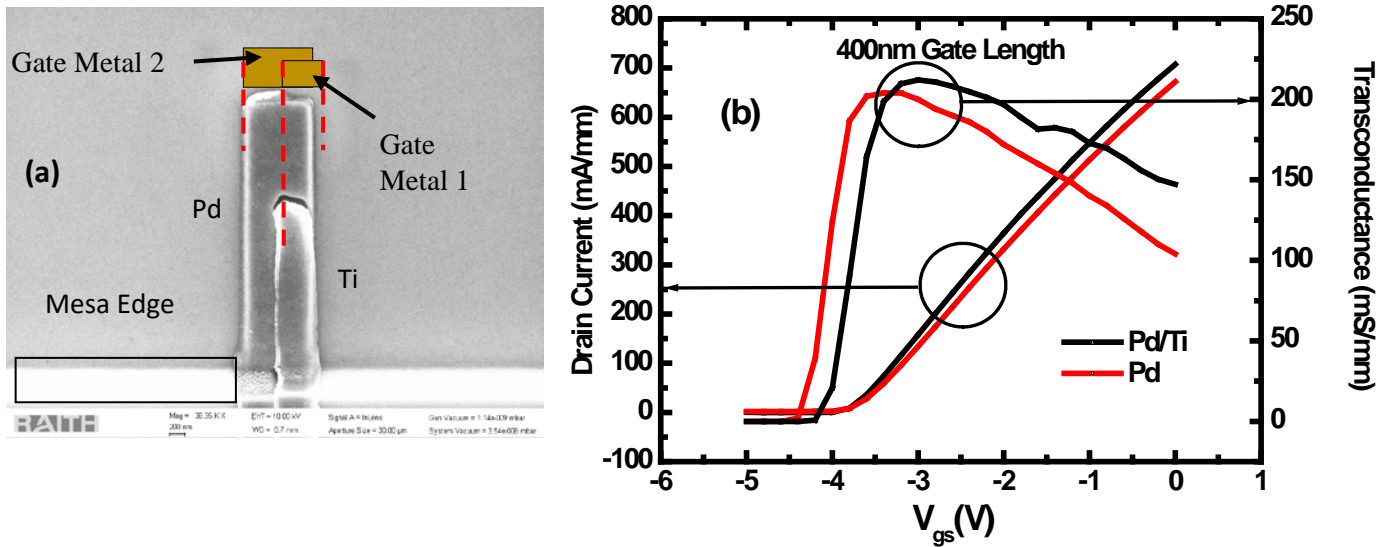


Fig. 1. (a) SEM image of the AlGaIn/GaN HEMT with Pd/Ti DMG structure. (b) Gate transfer characteristics of SMG and DMG AlGaIn/GaN HEMTs at $V_{ds} = 10$ V.

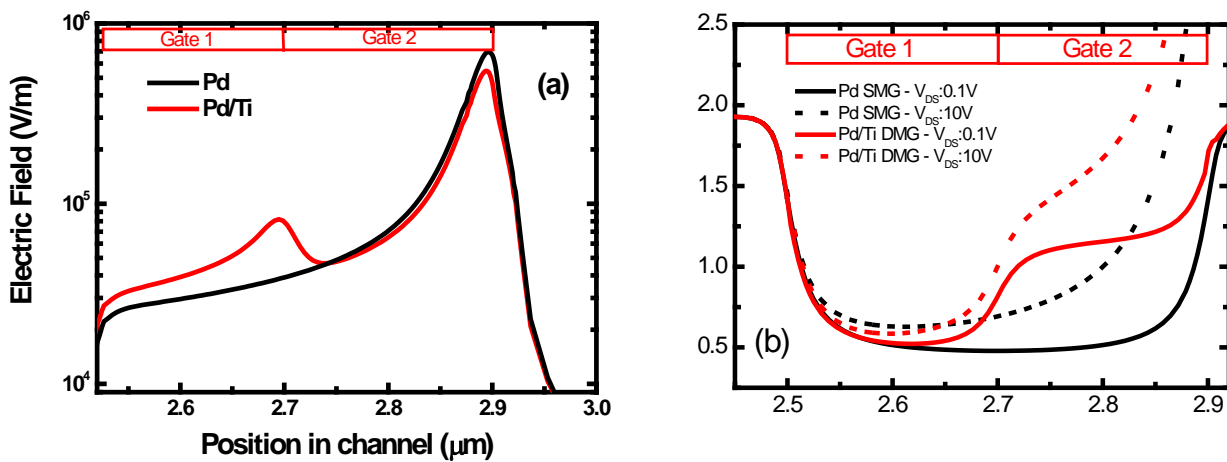


Fig 2. (a) Simulated electron velocity under the gate region along the channel for SMG and DMG at $V_{ds} = 10$ V and $V_{gs} = 0$ V. (b) Simulated electrostatic potential along the channel under the 400 nm gate region between SMG and DMG at $V_{gs} = -3.5$ V with varying drain bias.

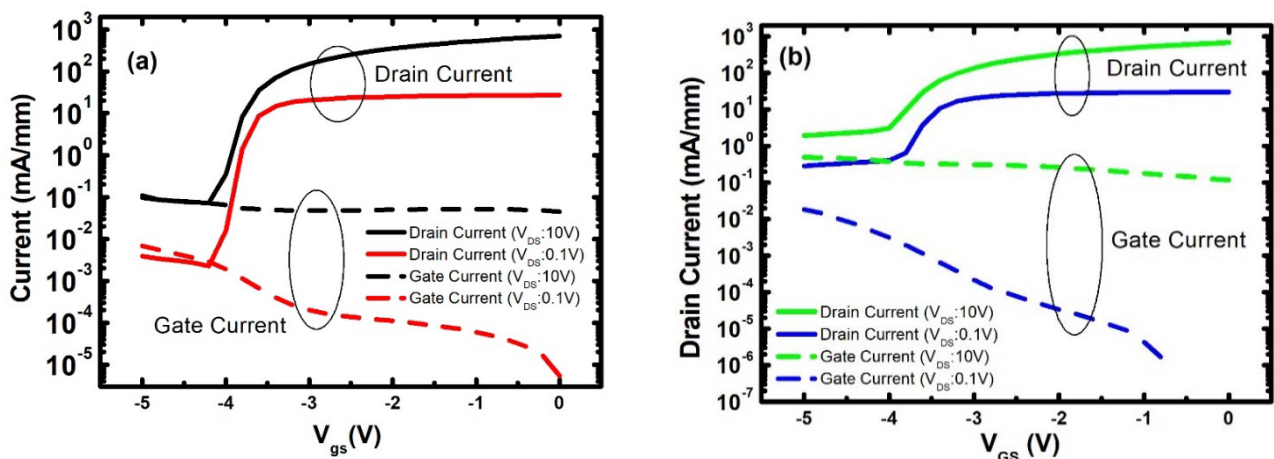


Fig. 3. Gate transfer characteristics of (a) DMG and (b) SMG HEMTs with drain bias of 0.1 V and 10 V.

Optimum design choices for AlGaIn/GaN HEMTs on diamond substrates

Thomas Gerrer¹, James Pomeroy¹, Feiyuan Yang¹, Daniel Francis², Jim Carroll², Brian Loran², Larry Witkowski², Marty Yarborough², Michael J Uren¹, and Martin Kuball¹

¹Centre for Device Thermography and Reliability (CDTR), University of Bristol, UK , ²Akash Systems, USA

We propose optimum thermal designs of GaN-on-diamond high electron mobility transistors (HEMT) fabricated on polycrystalline diamond substrates. For high-power GaN HEMT microwave amplifiers thermal degradation and the performance is critically decided by the substrate's thermal conductivity, which is five times larger for diamond as compared to SiC (the present industry standard). Until now, GaN-on-diamond technology demonstrated the fabrication on 4 inch wafer sizes [2], continuous operation at 250 °C for >3,000 h [3] and power densities of 56 W/mm [4] (DC operation). However, despite significant technological progress, the best thermal designs maximizing the performance per chip area and constraints related to conventional packaging materials like the die attach are still unclear. Here, high-resolution thermal measurements close to the hotspot region by optical technologies like micro-Raman thermography in conjunction with detailed thermal finite element (FE) simulations provide the best route to explore the thermal limits of this technology.

Based on the electrical and thermal characterization of large 10-finger 13 and 40 μm gate pitch GaN-on-diamond HEMTs with a gate periphery of 1.25 mm by pulsed I - V measurements (see Fig. 1) and Raman thermography (see Fig. 2) simulation were calibrated, and we investigated design opportunities and constraints for such technology operated at a high power dissipation of 8 W/mm. We employed a detailed thermal FE model (see Fig. 3) to study design variations of the 13 μm gate pitch GaN-on-diamond technology (PCD = polycrystalline diamond, SCD = single crystalline diamond) evaluated against a conventional 40 μm gate pitch GaN-on-SiC technology (see Tab. 1). In contrast to previous studies, the FE model accounts for the thickness dependent thermal conductivity of the GaN layer and the polycrystalline grain structure of the PCD substrate from the GaN/diamond interface to the bulk material.

We find that the 13 μm gate pitch GaN-on-diamond technology provides good thermal performance and enables a 3x larger areal power density over the commonly employed 40 μm gate pitch GaN-on-SiC designs. At 8 W/mm power density the 13 μm gate pitch GaN-on-diamond design results in ~35 °C and ~15 °C cooler peak channel temperature than for 40 μm gate pitch GaN-on-SiC, i.e. 190 °C for single and 210 °C for polycrystalline diamond substrates despite the 3× larger areal power density (see Fig. 4). As a result of our thickness dependent GaN thermal conductivity model, in the present GaN-on-diamond technologies with an effective GaN/diamond thermal boundary resistance (TBR_{eff}) of 20 m² °C/GW, a GaN thickness of 1.5 μm (see Fig. 5) is most optimal and combined technological optimizations of the TBR_{eff} to 10 m² °C/GW promise further sizable reductions by 25 °C from 210 °C to 185 °C. Furthermore, a 150 μm thick diamond substrate for 13 μm gate pitch design enables good thermal spreading, whereas less than ~100 μm thickness significantly increases the peak temperature. Finally, we found that the conventional Au-Sn die attach produces a sizable thermal resistance for the investigated GaN-on-diamond die sizes should be exchanged for Ag sintering in this new technology. In combination, the temperature could be reduced from 210 °C to 170 °C for the investigated 13 μm gate pitch GaN-on-diamond design.

- [1] M. Tyhach *et al.*, "S2-T3: Next generation gallium nitride HEMTs enabled by diamond substrates," in *2014 Lester Eastman Conference on High Performance Devices (LEC)*, 2014, pp. 1-4.
- [2] D. Francis, F. Faili, D. Babić, F. E. Ejeckam, A. Nurmikko, and H. Maris, "Formation and characterization of 4-inch GaN-on-diamond substrates," (in en), *Diamond and Related Materials*, vol. 19, no. 2-3, pp. 229-233, Feb-Mar 2010, doi: 10.1016/j.diamond.2009.08.017.

- [3] F. E. Ejeckam *et al.*, "3,000+ Hours continuous operation of GaN-on-Diamond HEMTs at 350°C channel temperature," in *2014 30th Semiconductor Thermal Measurement & Management Symposium (SEMI-THERM)*, 2014, pp. 242-246.
- [4] M. J. Tadjer *et al.*, "GaN-On-Diamond HEMT Technology With $T_{AVG} = 176^\circ\text{C}$ at $P_{DC,max} = 56\text{ W/mm}$ Measured by Transient Thermoreflectance Imaging," *IEEE Electron Device Letters*, vol. 40, no. 6, pp. 881-884, 2019, doi: 10.1109/led.2019.2909289.

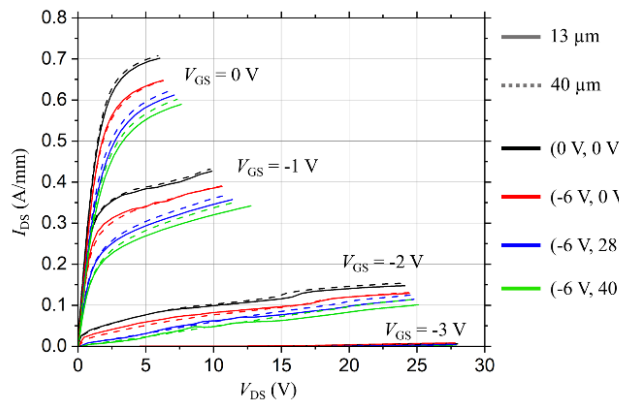


Table 1
Reference design parameters of the GaN Transistor on SiC and poly (PCD) and singlecrystalline diamond (SCD).

Parameters	SiC	PCD	SCD
Power density (W/mm)		8	
# device fingers		10	
Gate width (μm)		125	
Gate pitch (μm)		40	13
GaN thickness (μm)	1.8		0.7
TBR_{eff} ($\text{m}^2\text{ }^\circ\text{C/GW}$)	8		20
Die thickness (μm)	100		150
Die edge length (μm)		400	
Die-attach & thickness	35 W/m $^\circ\text{C}$, 25 μm		
T_{max} ($^\circ\text{C}$)	224	210	190

Fig. 1. Pulsed I-V output characteristics of the 13 μm and 40 μm gate pitch GaN-on-diamond transistor driven from a quiescent bias at ($V_{GS}=0\text{ V}/V_{DS}=0\text{ V}$), ($-6\text{ V}/0\text{ V}$), ($-6\text{ V}/28\text{ V}$) and ($-6\text{ V}/40\text{ V}$).

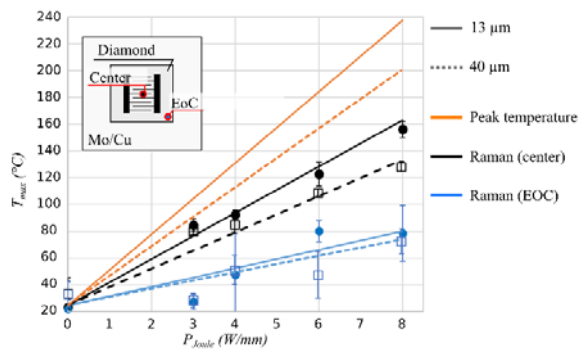


Fig. 2 Temperature for the 10-finger GaN-on-Diamond transistors (13 μm gate pitch and 40 μm gate pitch) as a function of the dissipated power density at different positions on the chip (cp. legend and inset). Raman thermography of the 13 μm gate pitch (dots) and 40 μm gate pitch (squares) transistor was used to fit the simulation. The fitted lines show the simulated temperatures for a TBR_{eff} of 20 $\text{m}^2\text{ }^\circ\text{C/GW}$.

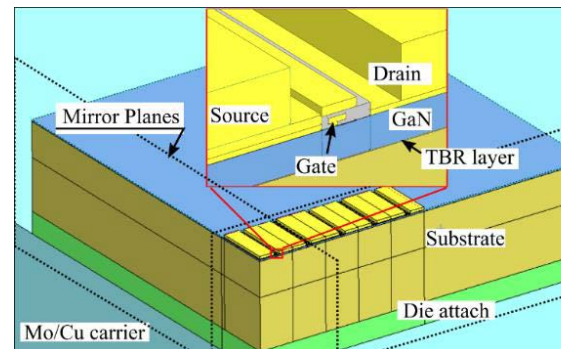


Fig. 3 Finite element model showing the GaN transistor on its substrate attached to the Mo/Cu carrier. The inset shows the detailed model of the drain, gate and source contacts. Symmetry reduces the model to one quarter of the device with respective isothermal boundary conditions.

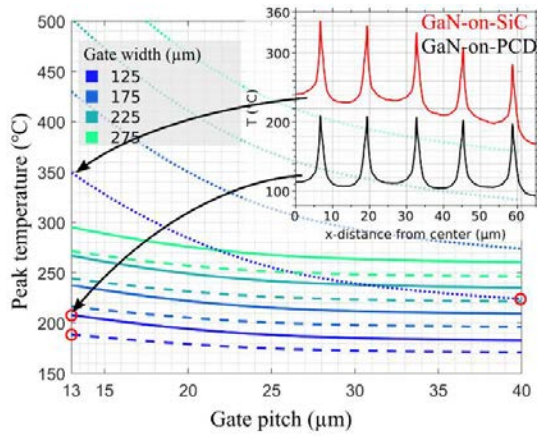


Fig. 4 Peak channel temperature as a function of gate pitch for GaN transistors on different substrates (SiC – dotted, PCD – solid, SCD – dashed) and gate widths ranging from 125 μm to 275 μm. The inset shows the temperature along the gate located hotspots from the device center to the outermost finger for a 13 μm gate pitch GaN-on-SiC and GaN-on-PCD transistor. Red circles mark the reference designs from Table 1.

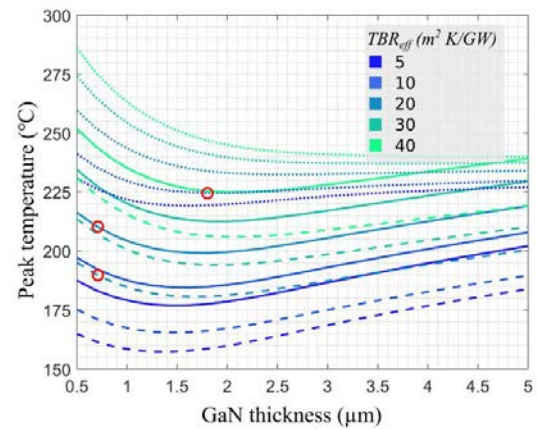


Fig. 5 Peak channel temperature as a function of the GaN film thickness for different substrates (SiC – dotted, PCD – solid, SCD – dashed) and TBR_{eff} ranging from 5 m² °C/GW to 40 m² °C/GW. Red circles mark the reference designs from Table 1.

Institute of Physics
37 Caledonian Road, London N1 9BU
Telephone: +44 (0)20 7470 4800
iop.org/conferences

Registered charity number 293851 (England & Wales) and SC040092 (Scotland)